A Modelling Study of HF Radar Coherent Detection of Irregularities in the High-latitude Ionosphere

Thesis submitted for the degree of
Doctor of Philosophy
at the University of Leicester

Li Zou B.Sc., M.Sc.
Department of Physics and Astronomy
University of Leicester
United Kingdom

September 1997

This thesis is dedicated to

my wife Fei Chen, my daughter Jaqi Zou

and

my father, mother, and brother Liang Zou

A Modelling Study of HF Radar Coherent Detection of Irregularities in the High-latitude Ionosphere

Li Zou

Abstract

Ground-based coherent backscatter radar systems are extensively used to investigate small-scale dynamics in the earth's ionosphere and related geophysical process(es) in the magnetosphere. At high-latitudes, HF radars are used due to the requisite orthogonal condition with the earth's magnetic field lines. Because of the effect of ionospheric refraction on the ray paths, the exact path of the radar signal through the ionosphere is then unknown. In practice, it is important to locate the radar echo sources given the echo parameters, such as group path, elevation angle, and azimuth angle. Furthermore, radar observations consist of direct backscatter from the ground. An uncertainty arises due to the difficulty in separating true ground backscatter from ionospheric scatter which fulfils the radar criteria based on the measured Doppler velocity and spectral width. These problems are investigated in this research using a three-dimensional ray tracing computer programme, Jones3D (Jones and Stephenson, 1975). Some problems in the Jones3D code have been identified and corrected whilst modifications to the code have been made to suit the purpose of this research work. All modelling work presented in this thesis are based on two HF radars, the Halley HF radar in Antarctica and the CUTLASS HF radar in Finland. For the best comparison with radar observations, realistic ionospheric conditions are used. In the case study for the Halley HF radar in Antarctica, it is found that the radar's main propagation mode is one-hop propagation, and that the radar scatter is mostly organised in ranges in the order of E- region scatter, F- region scatter, and ground scatter. The range-bin statistical analysis suggests that the radar criteria based on the measured Doppler velocity and spectral width are not sufficient, and that the measured range (group path) parameter is important and should be used in separating radar ionospheric echoes from ground backscatter. In the case study for the CUTLASS HF radar in Finland, it is found that the radar's first hop and second hop propagation are both important, although most of the main features of the radar summary plot of beam 5 are from the first hop radar propagation. Ray tracing results also suggest that the radar criteria are generally good for E- region scatter, but not good for F- region scatter. Besides, for the Finland radar, ray tracing results suggest that the radar beam-width in elevation should be based on 10 dB attenuation in power, rather than 3 dB. Thus, the scatter from behind the radar can sometimes be significant. This point has been confirmed (Milan *et al.*, 1997a, b).

Acknowledgements

For making this thesis possible and for sustaining me throughout its construction thanks are given to:

Professor Tudor Jones for his stewardship as head of the Radio and Space Plasma Physics Group (Department of Physics and Astronomy, University of Leicester) and his helpful discussions of HF radar modelling using the ray tracing technique.

Dr. Mark Lester for his supervision, encouragement and constant support. He introduced me into the research of HF radar study of small-scale irregularities in the high-latitude ionosphere and provided constant guidance, leading me through the maze of the research project. Not only did he support me in scientific aspects, but also he gave me his generous help in other areas which is considered essential for the completion of the thesis and the success of my future career.

Dr. Tim Yeoman for his encouragement, valuable discussions of HF radar modelling and various practical support.

Professor Terry Robinson for his encouragement, invaluable teaching on the theory of plasma waves, and helpful discussions about irregularities and gravity waves.

Dr. Mike Pinnock for PACE data and helpful discussions of irregularities and radar systems.

Dr. H. Yamagishi for his appreciation of my research work, useful suggestions for ray tracing and HF radar modelling.

Dr. Chris Thomas for CUTLASS data, Nigel Wade for help with computing of all types, Dr. Alan Stocker for the Jones3D programme, Dr. Neil Anold for atmospheric

waves, Peter Chapman, Mick Parsons, Warren Smith, Stuart Crooks, Lynda Forsyth, and Martin Hollingshead for various assistance.

Everyone else who I had the fortune to work with in the Radio and Space Plasma Physics Group, including Dr. Farideh Honary, Dr. Eric Bradshaw, Dr. Paul Eglitis, Dr. Awni Abdulahad, Dr. John Taylor, Paul Rylah, Dr. Jackie Davies, Dr. Steve Milan, Dr. Darren Wright, Dr. Brian Shand, Mark Ransom, Dr. Richard Beard, Jon Angell, Gabrielle Provan, Julian Thornhill, and Kathleen Bowers, ...

At the Upper Atmosphere Group, Department of Physics and Astronomy, University of Southampton, special thanks are given to:

Professor Henry Rishbeth (group leader) for his constant encouragement and support. The thesis would not have been finalised in time without his generous support.

Dr. Betty Lanchester for her very kind support, helpful discussions, suggestions, and proof reading.

Professor Manfred H. Rees for his encouragement, Dr. Paul Field (various help), Dr. Francis Sedgemore (Dynasonde), Mike Hill (various computer operating systems), and Dave Smith (computing support).

This work has been jointly sponsored by the State Education Commission of the People's Republic of China and the British Council through the Sino-British Friendship Scholarship Scheme (SBFSS).

Finally, my deepest appreciation goes to my wife Fei Chen and my daughter Jaqi Zou for their love, care, understanding and encouragement during my graduate studies.

Contents

CHAPTER 1 INTRODUCTION

1.1 INTRODUCTION

Our near earth environment is constantly under the influence of the sun's radiation. One of the most important consequences of this radiation is that the earth's upper atmosphere is partially ionised. This ionisation, between 60-600 km, has profound effects on the propagation of radio waves. This region, termed the ionosphere, serves as a giant natural laboratory of magnetised plasma which is full of dynamical processes of different spatial and temporal scales and, thus, provides us with a unique opportunity for studying a wide range of problems of basic plasma physics.

The ionosphere can be investigated by a wide range of in situ and remote sensing techniques. The research work presented in this thesis is concerned with the computer simulation of HF radar coherent detection of small-scale ionospheric irregularities. The modelling results are compared with HF radar observations made in both northern and southern hemispheres by the Halley HF radar in Antarctica and the CUTLASS HF radar in Finland. Before the subject is expanded upon, it is useful to introduce briefly some relevant background material, which includes the sun's influence on our near earth's environment, the neutral atmosphere, the nature and distribution of the ionospheric plasma, and the structures in the high-latitude ionosphere.

1.2 THE SOLAR-TERRESTRIAL ENVIRONMENT

The sun constantly emits both electromagnetic (EM) and corpuscular radiation into interplanetary space. Electromagnetic radiation, such as radio, infrared, visible, ultraviolet (UV), extreme ultraviolet (EUV), and X-rays, travels at the free space speed of light radially outwards from the sun. The transit time of the solar EM radiation from

the sun to the earth is about 8.3 minutes. As a result of this solar EM radiation, especially EUV and X-rays, the upper part of the earth's atmosphere is partially ionised. The ionisation is of sufficient magnitude that the plasma density can have profound effects on the propagation of radio waves in this region.

The solar corpuscular radiation (solar wind), which comes mainly from the expansion of the solar coronal plasma into interplanetary space, consists of solar energetic particles and the 'frozen-in' interplanetary magnetic field (IMF). A typical speed of the solar wind at a distance of 1 AU from the sun is around 400 km/s, which can increase to about 1,000 km/s during disturbed periods (Davies, 1990). When the solar wind travelling at supersonic speed reaches the earth, it impacts on and compresses the earth's dayside outer geomagnetic field. At the nightside, it pulls the geomagnetic field out to more than 100 earth radii to form the so-called geomagnetotail, see figure 1.1. The resultant cavity containing the deformed geomagnetic field is called the magnetosphere. Magnetospheric physics is a very large complex subject and is not discussed here in more detail. The interested reader is referred to Ratcliffe (1970), Dungey (1961), Axford and Hines (1961), and, more recently, Hargreaves (1992), Kamide and Baumjohann (1993).

Solar activity resulting from solar flares and coronal mass ejections can cause severe disturbances in the earth's magnetosphere and ionosphere. Such activity may start with dayside sudden ionospheric disturbance (SID) due to enhanced EM radiation which tends to be relatively short lived (~10 - 60 mins). This is often followed by severe geomagnetic field disturbances called a magnetic storm which may include a series of nightside magnetic substorms. Polar cap absorption (PCA) events and ionospheric storms may also follow with time scales for recovery of order several days.

1.3 THE NEUTRAL ATMOSPHERE

The neutral atmosphere not only serves as a reservoir of neutral particles to be ionised by the solar radiation, but also through collisions with charged particles interacts with the ionosphere. Although the ionisation in the earth's upper atmosphere is very

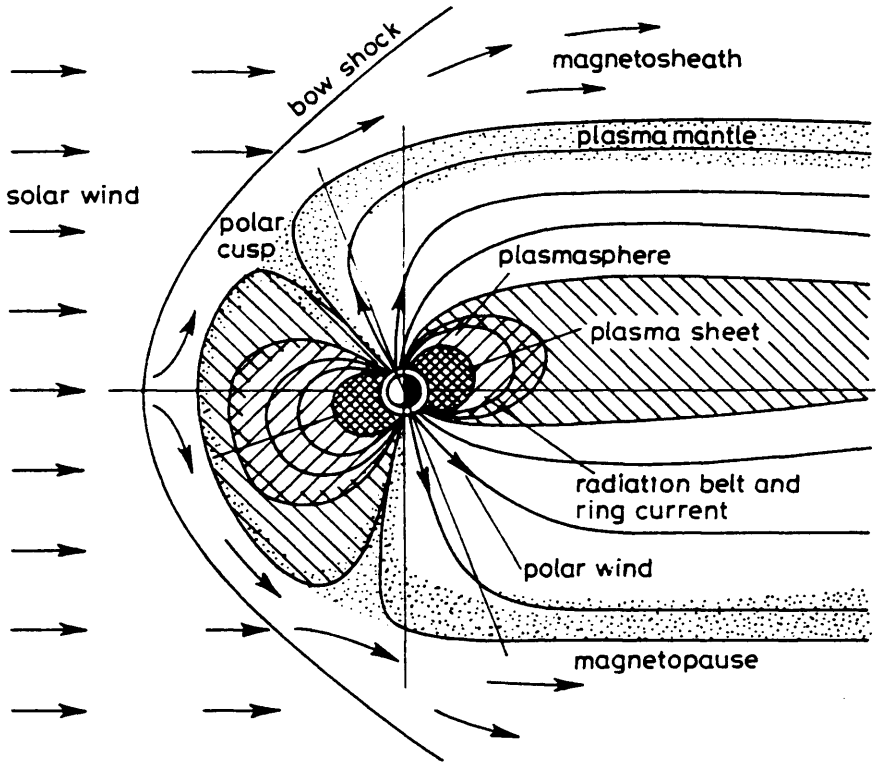

Figure 1.1 Magnetosphere formed by the interaction of the solar wind with the earth's magnetic field

important in terms of ionospheric radio wave propagation, the ionisation is only one of the minor constituents of the earth's upper atmosphere. Even in the main layers of the ionosphere, less than 1% of the air is ionised (Rishbeth, 1988). The neutral atmosphere can be subdivided either by its vertical average temperature structure or dynamical processes. A brief summary is given below.

1.3.1 Vertical average temperature structure

By its vertical temperature structure, the atmosphere may be subdivided into four main regions, which are the troposphere, stratosphere, mesosphere and thermosphere. Figure 1.2 shows a typical vertical temperature profile, which is a model profile at equinox for mid-latitudes taken from the U.S. standard atmosphere (1976).

The troposphere (0 - 12 km) is the lowest region of the earth's neutral atmosphere, where the temperature decreases from its ground level value with increasing height. The main heat source for this region is the solar radiation absorbed by the surface of the earth. The temperature in this region ceases to decrease at the tropopause. The height of the tropopause has a clear latitudinal variation, being highest in the equatorial region and decreasing with increasing latitude.

The region above the tropopause is termed the stratosphere (12 - 50 km), in which the temperature increases with height. The stratosphere temperature reaches its maximum of about 270 K at the stratopause. The main heat source for this region is the absorption of solar ultraviolet radiation by ozone.

Above the stratopause, the temperature decreases again reaching a minimum of 180 - 190 K at the mesopause (around 80 km altitude), the coldest part of the whole terrestrial atmosphere. The heat source in this region is determined by the radiative heating of molecular oxygen and infrared radiative cooling of carbon dioxide.

The thermosphere (above 80-90 km) is the top region of the terrestrial atmosphere, in which the temperature increases monotonically with height, as shown in figures 1.2 and

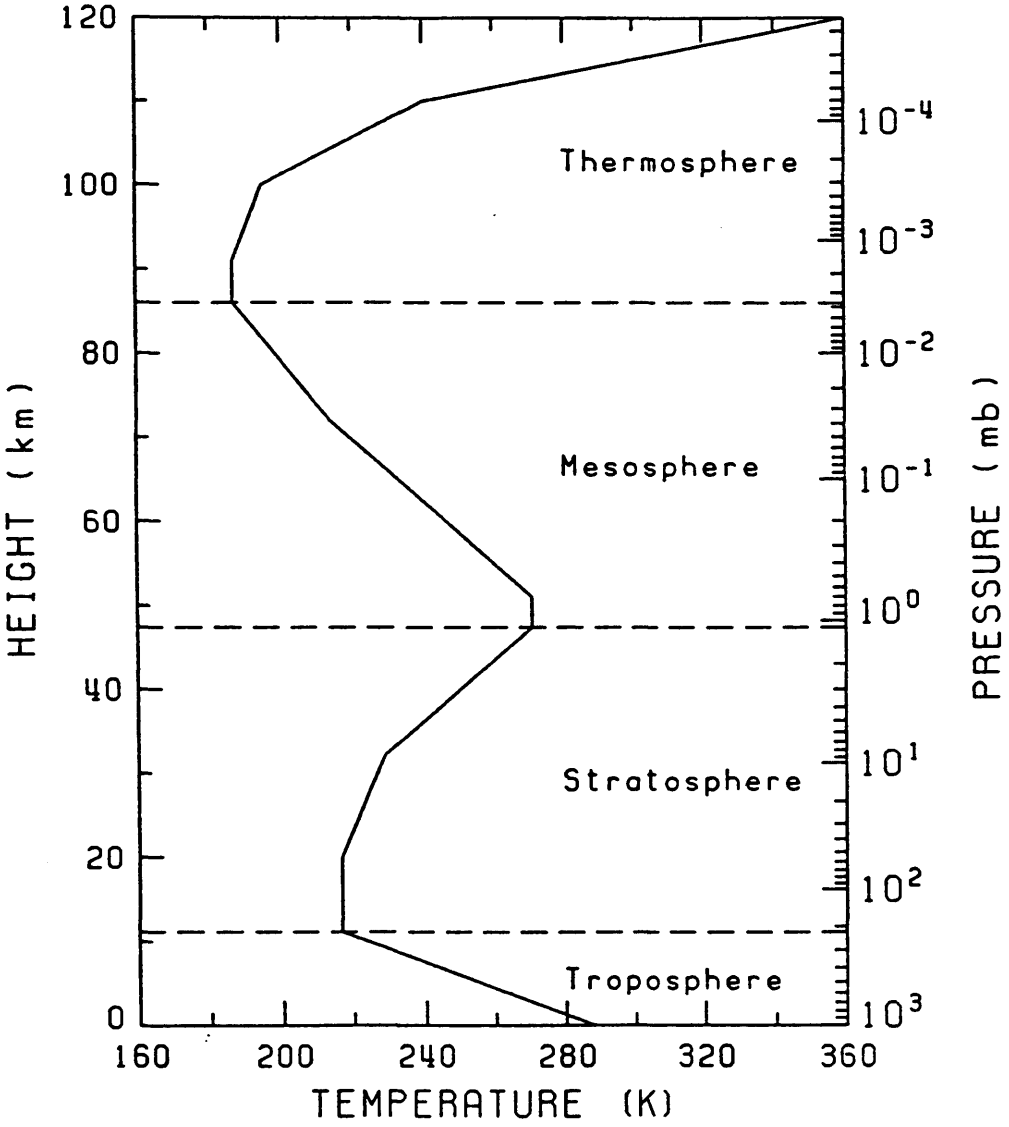

Figure 1.2 A model temperature profile for mid-latitude equinox (taken from the U.S. standard atmosphere, 1976)

1.3. The highest temperature of this region could reach 1,000 to 2,000 K due to radiative heating of atomic oxygen.

1.3.2 Arranged by dynamical processes

Dynamically, the neutral atmosphere can be subdivided into three main regions, termed the turbosphere, diffusosphere and exosphere, as shown in the right panel of figure 1.3. The turbosphere is a region below 100 km altitude, where the major gas constituents, nitrogen (N_2) and oxygen (O_2), are well mixed by turbulence, and where the air can be treated as a gas with constant molecular weight. The top of this region is referred to as the turbopause. Above the turbopause is the diffusosphere, 100 - 700 km, where all gas constituents are diffusively separated by the action of gravity because of lack of turbulence. The region above 700 km altitude is termed the exosphere, where the air is too rare to be considered as a gas. Individual atoms can move freely in satellite-like orbits controlled by the earth's gravity. At higher altitude, the gravity is so small that some atoms could be moving upwards and finally escaping from the gravity of the earth.

1.4 THE IONOSPHERE

The ionosphere, 60-600 km, is defined as that part of the earth's upper atmosphere in which free electrons are sufficiently numerous to influence the propagation of radio waves (Rishbeth, 1988). The ionisation is produced by a wide spectrum of solar EUV and X-ray radiations. Early ionosonde studies (Breit and Tuve, 1926) revealed that the ionosphere could be subdivided into several main layers. They are D, E and F layers as designated in the left panel of figure 1.3.

1.4.1 Basic ionospheric processes

In the real situation, the formation of the ionospheric D-, E- and F- regions are quite complicated. However, the main features of the ionisation production and loss

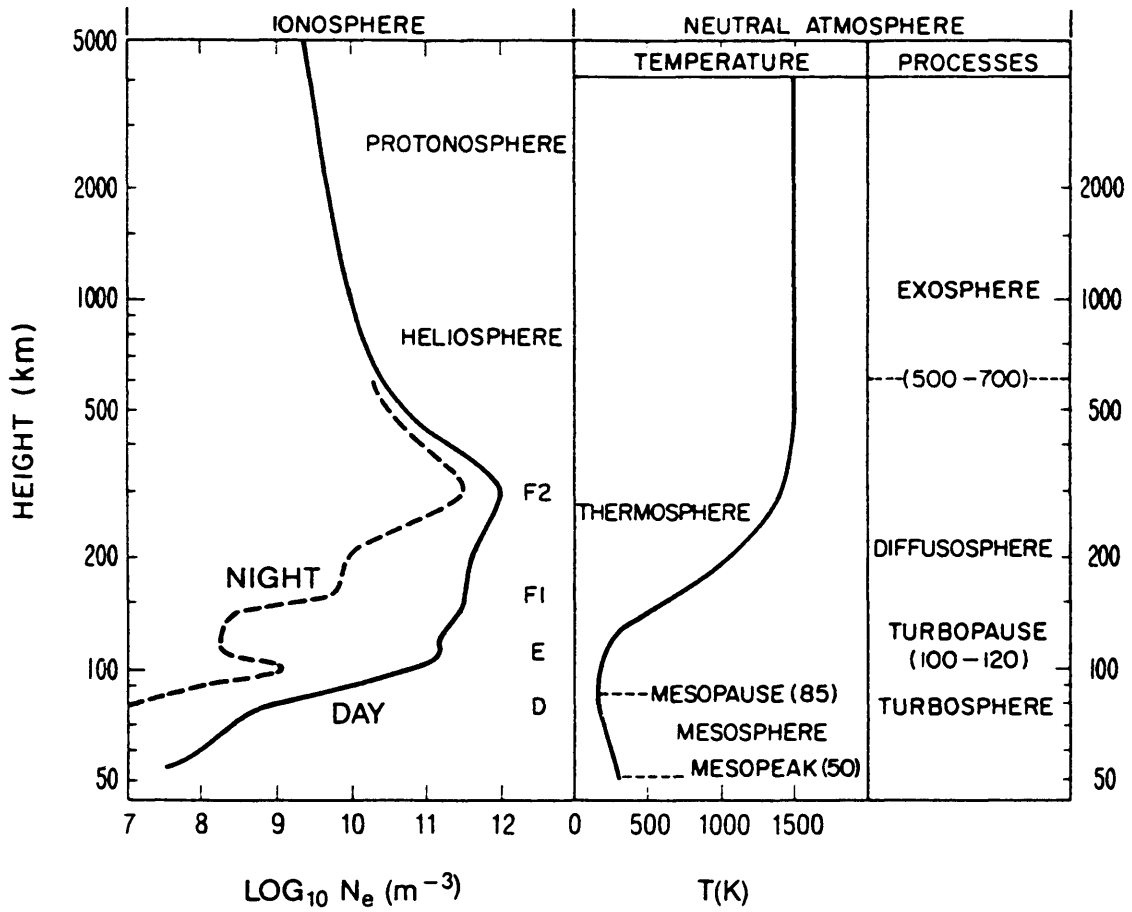

Figure 1.3 Atmosphere division by temperature and dynamics

processes can be summarised fairly simply as follows. For either electrons or ions, the continuity equation is given by

$$\partial N/\partial t = q - L(N) - \nabla\cdot(N\mathbf{V}) \qquad (1.1)$$

where N is number density, q the production rate, L(N) the loss rate, **V** the drift velocity. The transport term $\nabla\cdot(N\mathbf{V})$, except for the F2 layer, is usually less important and neglected. If quasi-equilibrium is assumed, equation (1.1) becomes

$$L(N) = q \qquad (1.2)$$

in which the loss term may be generalised as

$$L(N) = \alpha N^2 \qquad \text{Chapman } \alpha \text{ layer} \qquad (1.3)$$

$$L(N) = \beta N \qquad \text{Chapman } \beta \text{ layer} \qquad (1.4)$$

The above two equations represent the two main electron loss processes in the ionosphere. Equation (1.3) is the recombination reaction in which the rate of loss of electrons is proportional to the square of the electron density, and (1.4) is the attachment reaction in which the rate of loss of electrons is proportional to the first power of the electron density (and not the second power, as for recombination). For an ideal Chapman layer, assuming the scale height ($H = \frac{kT}{mg}$) independent of height (where k is Boltzmann constant, T is the temperature of the gas, m is the atomic (molecular) mass and g is the gravitational acceleration), the peak production rate of the layer is given by (Rishbeth and Garriott, 1969)

$$q_m = q_o \cos\chi \qquad (1.5)$$

where q_o is the peak production rate for an overhead sun and χ is solar zenith angle. Combining equations (1.2), (1.3), and (1.5) as well as (1.2), (1.4), and (1.5) gives

$$N_m \propto \sqrt{\cos\chi} \qquad \text{Chapman } \alpha \text{ layer} \qquad (1.6)$$

$$N_m \propto \cos\chi \qquad \text{Chapman } \beta \text{ layer} \qquad (1.7)$$

where N_m is the peak electron density of the layer. The critical frequency of the ordinary mode of the layer is given by

$$f_o^2 = 80.6\, N_m \qquad (1.8)$$

Substituting (1.6) and (1.7) into (1.8) gives

$$f_o \propto \sqrt[4]{\cos\chi} \qquad \text{Chapman } \alpha \text{ layer} \qquad (1.9)$$

$$f_o \propto \sqrt{\cos\chi} \qquad \text{Chapman } \beta \text{ layer} \qquad (1.10)$$

1.4.2 Main ionospheric regions

The D-region (60 - 90 km), the lowest part of the earth's ionosphere, is mainly ionised by solar X-rays, cosmic rays and solar Lyman α. The electron loss process in the D-region is predominated by the attachment of electrons to neutral atoms and molecules to form negative ions, which can then recombine with positive ions. At night, negative ions are more abundant than electrons at all heights below 90 km. By day, the negative ions are very quickly destroyed by the visible and ultraviolet sunlight and they are only abundant below 70 km. Since the predominant loss process of electrons is by the attachment reaction, the rate of loss of electrons is expected to be proportional to the electron density, i.e. $L(N) = \beta N$, equation (1.4). Observations show that the D-region electron density does vary quite regularly with equation (1.7), which can then be used to test whether the main loss mechanism in the layer is by attachment or recombination.

Above the D-region is the E-region (90 - 150 km), which is mainly produced by solar EUV and X-ray radiation, where almost all positive ions (NO^+ and O_2^+) are molecular and the dominant electron loss process is by dissociative recombination reaction. In this case, the rate of recombination of electrons equals the rate of recombination of the

molecular ions, $L(N) = \alpha N^2$. In fact, the critical frequency of the E-region, f_oE, varies quite regularly with equation (1.9), which means the E-layer is a Chapman α layer.

The region above E is termed the F-region (150 - 600 km), sometimes being a single layer and sometimes split so that the F1 layer/ledge appears well developed on its lower side. At night, it is always single with no F1 layer at all. By day the F1 layer is more prominent in summer and towards the minimum of the solar cycle. When the F1 layer is observed, its penetration frequency, f_oF1, behaves as expected for a Chapman recombination layer, as described by equation (1.9). This is because the dominant positive ions in the F1-layer are molecular (NO^+ and O_2^+) and because the principal electron loss process is by dissociative recombination reaction.

Above the F1 layer is the F2 layer, where the positive molecular ions (NO^+ and O_2^+) give way to positive atomic oxygen ions (O^+) and the recombination reactions are changed. The most important chemical reactions in the F2 layer are

$$O^+ + N_2 \rightarrow NO^+ + N \qquad (1.11)$$

$$NO^+ + e^- \rightarrow N + O \qquad (1.12)$$

$$O^+ + O_2 \rightarrow O_2^+ + O \qquad (1.13)$$

Equations (1.11) and (1.13) are called charge exchange reactions and equation (1.12) is a dissociative recombination reaction. Equation (1.13) is less important, since, compared to N_2, the smaller scale height of O_2 results in a faster rate of decrease in density with increasing height. Above the F1 peak, the rate of production of electrons (and ions) is determined by the atomic oxygen density, which decreases upwards depending on its scale height. On the other hand, the rate of loss of O^+ is mainly controlled by equation (1.11), and is then dependent on the number of nitrogen molecules (N_2) available at that height, which decreases upwards faster than atomic oxygen (O) because of its smaller scale height. The consequence is that, although the rate of production decreases upwards above the F1 peak, the electron density in an equilibrium layer increases upwards and it is these electrons which form the F2 layer (Ratcliffe, 1970). Furthermore, because the ion loss process is mainly controlled by

(1.11), the rate of loss of ions is assumed to be linearly proportional to its own density, equation (1.4). The F2 layer is, therefore, a Chapman β layer.

1.5 STRUCTURES IN THE HIGH-LATITUDE IONOSPHERE

The high-latitude ionosphere is the most dynamic part of the earth's ionosphere due to the electrical coupling between the high-latitude ionosphere, the magnetosphere and the solar wind. A number of processes are involved in this coupling and these are discussed below.

1.5.1 Coupling between the ionosphere, magnetosphere and solar wind with field-aligned currents

Above the E-region, because the collisions between charged particles and neutrals are very rare, the conductivity parallel to the earth's magnetic field σ_0 (specific conductivity) can be very large, much greater than σ_P (Pedersen conductivity) and σ_H (Hall conductivity). Therefore, above the E-region the geomagnetic field lines can be taken as very good conductors being able to transmit electric fields for long distances along **B**.

Due to the open geomagnetic field lines at high-latitudes, both of the high-latitude ionospheres are electrically linked through field-aligned currents to the magnetosphere and sometimes even to the interplanetary medium (when the IMF B_z southward), which makes this part of the ionosphere exposed to and very likely influenced by large-scale disturbances generated in either the magnetosphere or solar wind.

1.5.2 High-latitude ionospheric convection

The electrical coupling through field-aligned currents to the magnetosphere and even to the interplanetary medium means that large-scale electric fields generated in the outer magnetosphere or solar wind can map down to the high-latitude ionosphere. The resultant effect is the production of large-scale convection of high-latitude ionospheric plasma, figure 1.4.

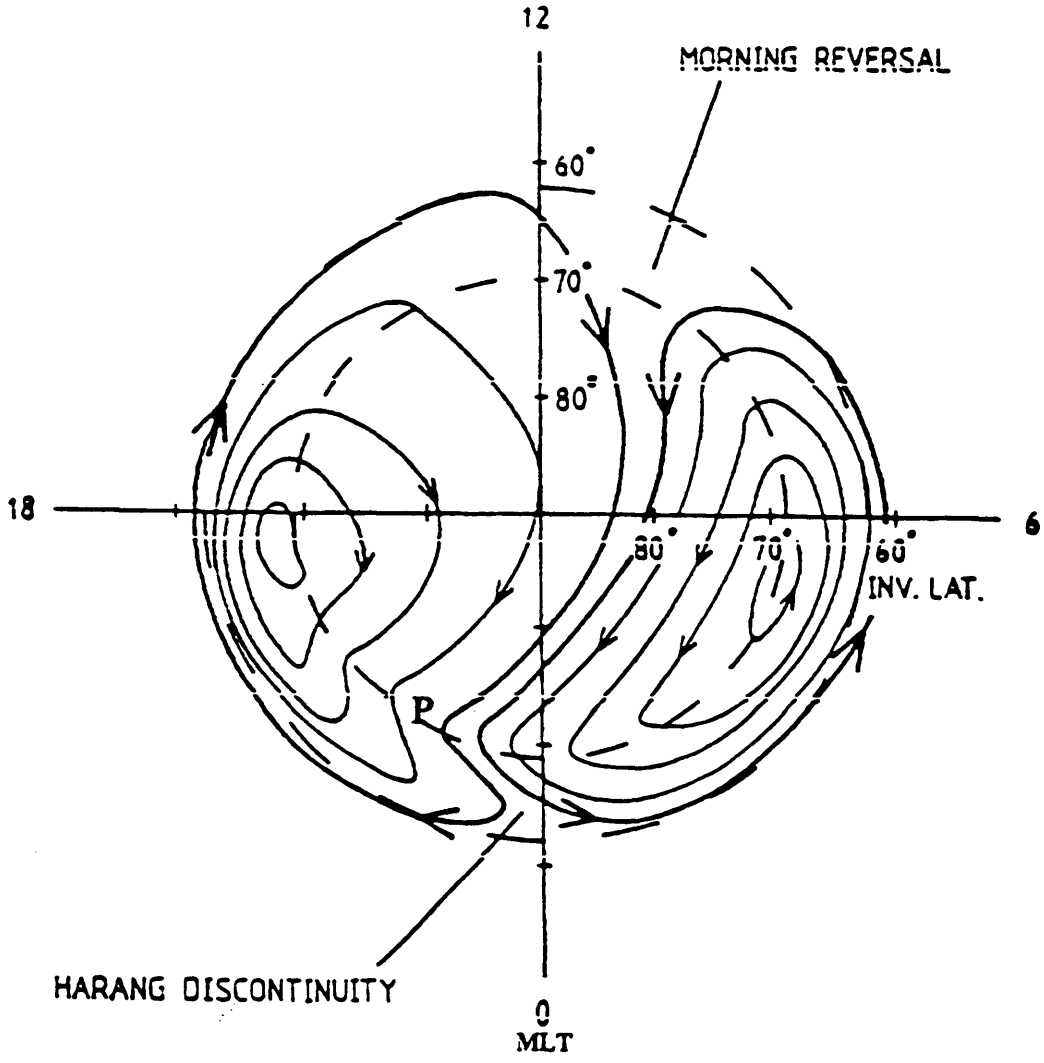

Figure 1.4 High-latitude plasma convection

1.5.3 Particle precipitation and aurora

In the auroral region, energetic particles from the solar wind can, from the dayside cusp, precipitate into the ionospheric E-region, strike the neutrals there to produce the dayside optical aurora. On the nightside, charged particles from the magnetotail can also be accelerated back into the nightside auroral region, forming the nightside aurora. Large-scale patches of enhanced ionisation are produced by these precipitating particles and, at the same time, small-scale structures may be produced by gradient drift instability.

1.6 THE AIM OF THIS RESEARCH

In the past ten years much effort has been directed towards studying the high-latitude ionospheric irregularities both theoretically and experimentally (e.g. Greenwald *et al.*, 1985, 1995; Villain *et al.*, 1985; Glassmeier *et al.*, 1987, 1989; Robinson, 1986; St-Maurice, 1987). Many ground-based coherent radars, such as PACE (HF), CUTLASS (HF), SABRE (VHF), and incoherent scatter radars, such as EISCAT, Sondrestrom, and Millstone Hill, have been developed and are in operation. Many ground-based high-latitude magnetometer networks have also been built and put in operation as well. With the help of these radars and magnetometer arrays, the knowledge of high-latitude irregularities has greatly been advanced, but much still remains to be known.

The aim of this research is to simulate HF radar coherent detection of small-scale irregularities in plasma density in the high-latitude ionosphere. The modelling results are compared with radar observations made in both northern and southern hemispheres by the Halley HF radar in Antarctica and the CUTLASS HF radar in Finland. This research work involves three-dimensional ray tracing modelling of HF coherent detection of ionospheric small-scale irregularities under realistic ionospheric

conditions. Emphasis is given to the separation of radar ionospheric echoes from ground backscatter.

CHAPTER 2

SMALL-SCALE IRREGULARITIES IN THE HIGH-LATITUDE IONOSPHERE

2.1 INTRODUCTION

It is believed that small-scale structures of electron density in the high-latitude ionosphere are produced by a variety of plasma instability mechanisms over a range of altitudes. Our modern understanding of these mechanisms started with the independent work of Farley (1963) and Buneman (1963) on the high-latitude auroral electrojet instability. Since then, especially in the past ten years, small-scale structures of electron density in the ionosphere have been studied extensively by ground-based HF, VHF, and UHF radars. In the mean time, theoretical efforts have been made to understand the physics behind these radar backscatter phenomena. Some elegant theories, linear and nonlinear, have been developed on the generation and growth of these density irregularities. Comprehensive reviews on the subject of ionospheric irregularities have been given by Fejer (1979), Fejer and Kelley (1980), Farley (1985), and Haldoupis (1989).

Detailed discussion of the theory of small-scale irregularities in the ionosphere is out of the scope of this thesis. However, because the work presented in this thesis involves ray tracing modelling of HF radar coherent detection of field-aligned small-scale irregularities in the high-latitude ionosphere, it is useful to review in this chapter briefly both the theory and radar studies of the plasma irregularities in the high-latitude ionosphere.

2.2 CHARGED PARTICLE MOTION

In the upper atmosphere, the motion of charged particles is constantly affected by a number of factors, such as the external magnetic field, ambient electric field, gravity, collisions with other gas components. In general, the linearised momentum equation of the motion of charged particles in a magnetised plasma may be written as

$$m_j n_j \frac{\partial \mathbf{v}_j}{\partial t} = n_j q_j (\mathbf{E} + \mathbf{v}_j \times \mathbf{B}) + m_j n_j \mathbf{g} - k_B T_j \nabla n_j - m_j n_j \nu_{jn} (\mathbf{v}_j - \mathbf{U}) \quad (2.1)$$

where

subscript j is for the jth species of charged particles

m_j mass

n_j number density

q_j charge of particle

$\mathbf{v}_j$ perturbation velocity

k_B Boltzmann constant

T_j temperature

ν_{jn} collision frequency between the charged particles and neutrals

$\mathbf{E}$ ambient electric field

$\mathbf{B}$ a uniform external magnetic field

$\mathbf{g}$ gravitational acceleration

$\mathbf{U}$ neutral velocity

On the right-hand side of (2.1), from left to right, the first term is Lorentz force, second term the gravity effect, third term the pressure effect, and the last term neutral drag. If quasi-equilibrium is assumed, equation (2.1) becomes

$$n_j q_j (\mathbf{E} + \mathbf{v}_j \times \mathbf{B}) + m_j n_j \mathbf{g} - k_B T_j \nabla n_j - m_j n_j \nu_{jn} (\mathbf{v}_j - \mathbf{U}) = 0 \quad (2.2)$$

Set $\omega_{Bj} = \dfrac{q_j |\mathbf{B}|}{m_j}$, equation (2.2) may be rewritten as

$$\nu_{jn}\mathbf{v}_j - \omega_{Bj}(\mathbf{v}_j \times \hat{\mathbf{B}}) = \frac{q_j}{m_j}\mathbf{E} + \mathbf{g} - \frac{k_B T_j}{m_j}\frac{\nabla n_j}{n_j} + \nu_{jn}\mathbf{U} \tag{2.3}$$

where $\hat{\mathbf{B}}$ is the unit vector of **B**. The dot product of (2.3) with $\hat{\mathbf{B}}$ gives the motion of charged particles moving along the magnetic field lines,

$$\nu_{jn}\mathbf{v}_j \cdot \hat{\mathbf{B}} = \frac{q_j}{m_j}\mathbf{E}\cdot\hat{\mathbf{B}} + \mathbf{g}\cdot\hat{\mathbf{B}} - \frac{k_B T_j}{m_j}\frac{\nabla n_j}{n_j}\cdot\hat{\mathbf{B}} + \nu_{jn}\mathbf{U}\cdot\hat{\mathbf{B}} \tag{2.4}$$

in which the gravity and pressure effects are usually less important and negligible. Assuming **E** perpendicular to **B**, equation (2.4) becomes

$$\mathbf{v}_j \cdot \hat{\mathbf{B}} = \mathbf{U}\cdot\hat{\mathbf{B}} \tag{2.5}$$

which means that in the magnetic field direction charged particles move with the neutrals.

In perpendicular directions, if $\nu_{jn} >> \omega_{Bj}$ (which is the case for ions in the E-region), the first term on the left-hand side of (2.3) is usually more important than the second term. Neglecting the less important second term, (2.3) may be written as

$$\mathbf{v}_j = \frac{q_j}{m_j\nu_{jn}}\mathbf{E} + \frac{\mathbf{g}}{\nu_{jn}} - \frac{k_B T_j}{m_j\nu_{jn}}\frac{\nabla n_j}{n_j} + \mathbf{U} \tag{2.6}$$

in which, because of the large collision frequency, the first three terms on the right-hand side of (2.6) are less important and can be neglected. The velocity of charged particles is therefore eventually the same as that of the neutrals. This implies the fact that, when the collision effect is more important than the magnetic gyration effect, charged particles could simply be considered as being dragged by and moving with the neutrals. It appears as if the plasma were not magnetised. This situation is sometimes referred to as collision controlled or unmagnetised.

If $\nu_{jn} << \omega_{Bj}$, then, the second term on the left-hand side of (2.3) becomes more important than the first term, as is the case for electrons in the E-region, and for both electrons and ions in the F-region. Ignoring the less important term, (2.3) × **B** gives

$$\omega_{Bj}\mathbf{B}\times(\mathbf{v}_j\times\hat{\mathbf{B}}) = \frac{q_j}{m_j}\mathbf{E}\times\mathbf{B} + \mathbf{g}\times\mathbf{B} - \frac{k_B T_j}{m_j}\frac{\nabla n_j}{n_j}\times\mathbf{B} + \nu_{jn}\mathbf{U}\times\mathbf{B} \tag{2.7}$$

Expanding and rearranging (2.7) gives

$$\begin{aligned}\mathbf{v}_{j\perp} &= \mathbf{E}\times\mathbf{B}/B^2 \\ &+ \frac{\mathbf{g}\times\hat{\mathbf{B}}}{\omega_{Bj}} - \frac{k_B T_j}{\omega_{Bj}}\frac{\nabla n_j}{n_j}\times\hat{\mathbf{B}} + \frac{\nu_{jn}}{\omega_{Bj}}\mathbf{U}\times\hat{\mathbf{B}}\end{aligned} \tag{2.8}$$

The first term of (2.8) is usually the most important term. The other terms are less important because of the large gyration frequency ω_{Bj}. Thus, equation (2.8) may be simplified as

$$\mathbf{v}_{j\perp} = \mathbf{E}\times\mathbf{B}/B^2 \tag{2.9}$$

which means that, when the effect of magnetic gyration is much more important than the collisions with neutrals, charged particles may be considered as moving in the $\mathbf{E}\times\mathbf{B}$ direction (Hall direction) at the velocity $|\mathbf{E}\times\mathbf{B}/B^2|$, regardless of their mass and charge. Then, the charged particles of this species are said to be strongly magnetised.

The above discussion shows that in directions other than parallel to the magnetic field the motion of charged particles depends largely on the relative importance of the effects of the collisions with neutrals and magnetic gyration. If the magnetic gyration is more important, the charged particles are mainly driven by electromagnetic force and move in the $\mathbf{E}\times\mathbf{B}$ direction, in which case, the charged particles are considered to be strongly magnetised. If collisions are more important, then the plasma can be treated as if it were not magnetised, that is, collision controlled or unmagnetised.

The above discussion can be readily applied to plasma motions in both the ionospheric E- and F- regions. In the E-region, since $\nu_{en} << \omega_{Be}$ and $\nu_{in} >> \omega_{Bi}$, electrons are strongly magnetised and ions are collision controlled or unmagnetised. Thus, electrons move in the Hall direction while ions move with the neutrals. This implies that at E-region heights electrons and ions move at different speeds in different directions. Strong electric currents termed electrojets are thus produced. In the F-region, collisions with neutrals become less important for both electrons and ions. Thus, both electrons and ions are considered to be strongly magnetised. They move at more or less the same speed $\left|\mathbf{E} \times \mathbf{B} / B^2\right|$ in the same direction (Hall direction). No significant currents are produced at this altitude.

2.3 HIGH-LATITUDE AURORAL E-REGION PLASMA INSTABILITIES

Small-scale ionospheric irregularities are believed to be produced and sustained by various plasma instabilities, the small-scale electrostatic turbulence in the medium. In the high-latitude auroral E-region, the two most important instabilities are the cross field two-stream instability, also called the Farley-Buneman instability (Farley, 1963; Buneman, 1963), and the gradient drift instability (Simon, 1963; Hoh, 1963; Rogister and D'Angelo, 1970). These instabilities generate plasma density waves at auroral E-region heights giving rise to auroral radar backscatter. The streaming nature of the two-stream instabilities in the E-region causes them to collocate with ionospheric electrojets, which can then be located and studied by ground-based coherent scatter radar systems (Greenwald *et al.*, 1975).

2.3.1 Coherent radar studies of auroral E-region irregularities

The first extensive study of the high-latitude ionospheric convection using ground-based coherent scatter radars started in 1970s with the development of the Scandinavian Twin Auroral Radar Experiment (STARE) in northern Scandinavia (Greenwald *et al.*, 1978). STARE consists of two bistatic phased-array radars and is capable of determining a two-dimensional vector velocity map of irregularities in the E-region

using the Doppler data from the two radars. STARE was then extensively used for studies of the two-dimensional structure and dynamics of ionospheric plasma convection. The success of the STARE research led to the development of several other VHF radar systems, such as the Sweden And Britain Radar Experiment, SABRE, (Nielsen *et al.*, 1983) and the Bistatic Auroral Radar System, BARS, (McNamara *et al.*, 1983). Since then, a large amount of data has been obtained and some elegant linear and non-linear theories have been developed.

The spectra of received auroral radar signals are classified into four types, numbered from I to IV, as shown in figure 2.1. Type I and IV are due to the two-stream instability with type IV of enhanced ion-acoustic velocity due to elevated electron temperature. Type II is caused by gradient drift instability and type III is interpreted as due to collisional electrostatic ion-cyclotron waves.

2.3.2 Linear theory of E-region instabilities

At the height of the auroral electrojets, ~ 110 km, electrons are strongly magnetised and move in the $\mathbf{E} \times \mathbf{B}$ direction, while ions are collision controlled and stay with the neutrals. Driven by the electromagnetic force $\mathbf{E} \times \mathbf{B}$, electrons can move very fast through ion gas. Turbulence may be triggered by the friction between these two gas constituents. This process is known as the two-stream instability.

Gradient drift instability occurs when some triggering conditions are satisfied by favourable geometry of the background electron density gradient ∇n, the ambient electric field **E**, and the geomagnetic field **B**. A schematic diagram is shown in figure 2.2, which illustrates that, when the geometry conditions are met, any kind of initial perturbations in density δn is likely to be amplified by the electromagnetic force $\delta\mathbf{E}\times\mathbf{B}$ driving the lower density plasma up the gradient and the higher density plasma down the gradient. The polarised electric fields $\delta\mathbf{E}$ are produced by charge separation due to $\mathbf{E} \times \mathbf{B}$ drift of electrons (Hall current).

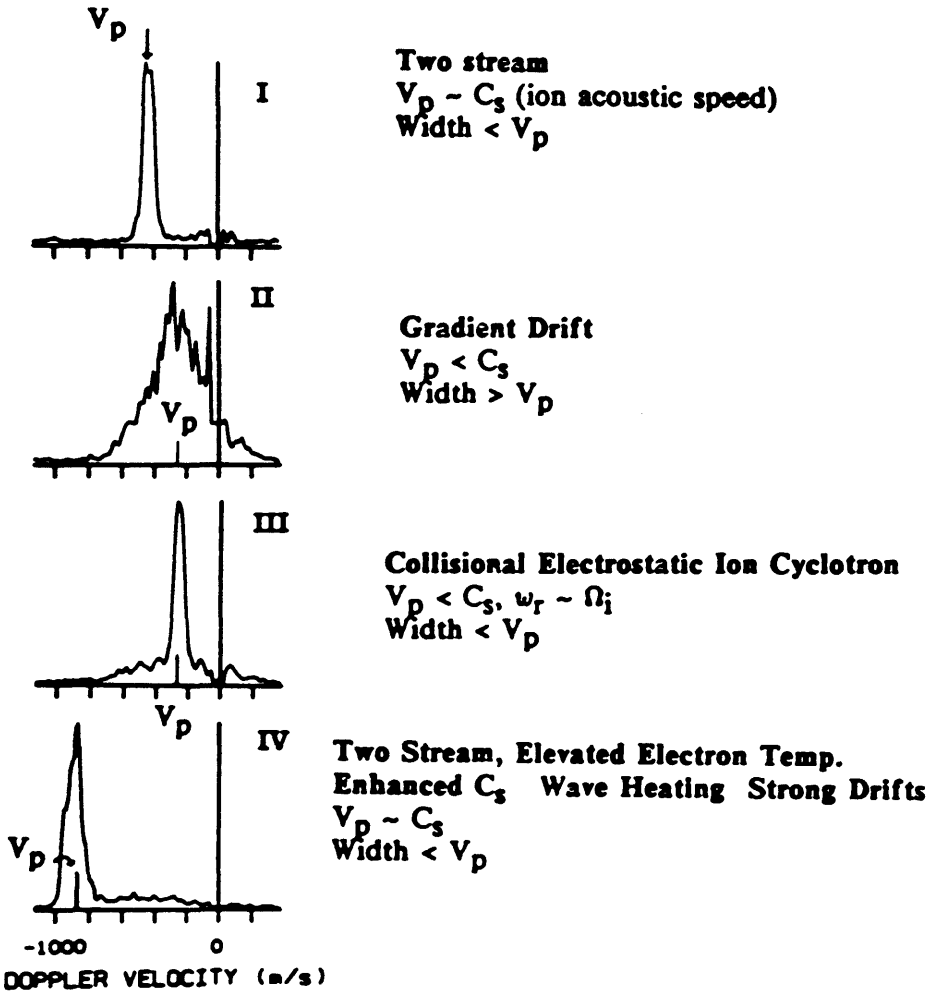

Figure 2.1 The four types of radar spectra that are observed in the auroral electrojet (courtesy of J. Providates)

In the existing linear theory, both the ambient electric field and electron density gradient are considered as two primary driving terms in the generation of electrostatic plasma density waves. These two driving terms are readily included in one dispersion relation, representing the modified two-steam and gradient drift instabilities, respectively. For the generated electrostatic waves, the two most important parameters are oscillation frequency ω and growth rate γ, which are given by

$$\omega_k = \frac{kV_d}{1+\Psi}\cos\theta \tag{2.10}$$

$$\gamma_k = \frac{\Psi}{(1+\Psi)}\left[\frac{\omega_k^2 - k^2C_s^2}{\nu_i} + \frac{\Omega_e\omega_k}{\nu_e kL}\right] \tag{2.11}$$

where

$$\Psi = \frac{\nu_e\nu_i}{\Omega_e\Omega_i}\left(1+\frac{\Omega_e^2}{\nu_e^2}\sin^2\alpha\right)$$

α	termed magnetic aspect angle defined as the angle between the propagation vector **k** and the direction perpendicular to magnetic field **B**
$C_s = \sqrt{\frac{K_B(T_e+T_i)}{<m_i>}}$	ion-acoustic speed
K_B	Boltzmann constant
T_e, T_i	electron and ion temperatures, respectively
$<m_i>$	mean ion mass
k	plasma wave number
$\theta = \arccos(\hat{\mathbf{k}}\cdot\hat{\mathbf{V}}_d)$	flow angle
$\mathbf{V}_d = \mathbf{V}_e - \mathbf{V}_i$	relative electron-ion drift velocity
$L = \frac{n_O}{(dn_O/dx)}$	the gradient scale length of electron density along the ambient electric field
n_o	background electron density
ν_e, ν_i	electron-neutral and ion-neutral collision frequencies, respectively
Ω_e, Ω_i	electron and ion gyrofrequencies, respectively

In the absence of density gradient, i.e. L = ∞, the instability becomes pure Farley-Buneman instability. The plasma becomes unstable when

$$V_d \cos\theta \geq C_s(1+\Psi) \tag{2.12}$$

2.3.3 Nonlinear theory

Early comparisons of observations between coherent scatter radar and EISCAT (European Incoherent Scatter radar) (Nielsen and Schlegel, 1985) showed that the phase speeds at metres scale of Farley-Buneman waves are limited to values near the ion-acoustic speed. For very large electric fields, the ion acoustic velocity can be enhanced due to wave heating of electron gas. This electron wave heating phenomenon in the auroral plasma can be explained satisfactorily in terms of extra collisions between electrons and plasmons by introducing a parameter ν_e^*, termed the anomalous electron collision frequency, which takes into account the momentum transfer between electrons and plasma waves due to electron scattering by waves (Robinson, 1986; St-Maurice, 1987; Haldoupis *et al.*, 1993; Robinson, 1994). Then, the above ν_e in (2.11) should be replaced by $\nu_e+\nu_e^*$. The essence of the nonlinear theory is that this extra collision process leads to wave drag and wave heating in the electron plasma and serves as a negative feedback mechanism stabilising the waves.

2.4 HIGH-LATITUDE F-REGION INSTABILITIES

The F-region ionosphere contains a wealth of electron density irregularities. These irregularities are also produced by plasma instability processes. Early studies show that irregularities are especially abundant at high latitudes (Aarons, 1973). As discussed in section 2.2, in the F-region, collisions between charged particles and neutrals become less important than the effect of magnetic gyration. Both electrons and ions are considered as being strongly magnetised and move in the $\mathbf{E}\times\mathbf{B}$ direction at more or less the same speed. Thus, in the F-region, there are no significant Hall currents (electrojets) and no two-stream instability at all. Plasma density irregularities may also

be formed by structured particle precipitation or images of magnetospheric turbulence. The most common plasma instability is the generalised $\mathbf{E} \times \mathbf{B}$ instability, responsible for the generation of plasma waves with relatively long wavelengths. An energy cascading process is believed to be responsible for producing secondary waves of shorter wavelengths which give rise to frequently observed HF coherent backscatter at auroral latitudes (Kelley and Heelis, 1989).

2.4.1 Coherent radar studies of auroral F-region irregularities

Historically, most early radar studies of F-region irregularities have been confined to low and mid-latitudes where VHF or UHF radars can achieve the required orthogonal condition with the earth's magnetic field (Woodman *et al.*, 1976; Tsunoda *et al.*, 1979). At high-latitudes, it is practically impossible for VHF or UHF radar waves in the F-region to achieve the required orthogonality in order to get the radar signals scattered back to the radar site. In the past decade, HF radars have been increasingly used to study the F-region irregularities in the high-latitude ionosphere. Taking advantage of the ionospheric bending effect, these HF radars can achieve the required orthogonality in both the E- and F- regions. They also extend the wavelength range of irregularity investigations out to 19 meters, thereby bringing the observations into a regime where plasma fluid effects dominate over plasma kinetic effects. Following the deployment of the Goose Bay HF radar, the prototype for the current generation of HF coherent backscatter radars (Greenwald *et al.* 1985), many other similar HF radar systems have been developed and put in operation (Greenwald *et al.*, 1995). Among them are the Polar Anglo-American Conjugate Experiment (PACE) and the Cooperative UK Twin Located Auroral Sounding System (CUTLASS). PACE is directed toward conjugate phenomena with emphasis on plasma convection (Baker *et al.*, 1989a, 1989b), while the CUTLASS HF radar is designed to be capable of resolving the vector velocity of plasma convection perpendicular to the earth's magnetic field and determining the elevation angle of arrival of backscattered signals (Milan *et al.*, 1997a). More detailed discussions of these two HF radars will be given in later chapters.

2.4.2 Generalised $E \times B$ instability

The generalised $\mathbf{E} \times \mathbf{B}$ instability is a high-latitude F-region implementation of the generalised gradient drift instability, which is developed out of the linear theory of the Rayleigh-Taylor instability first proposed by Dungey (1956) as a mechanism for the formation of equatorial spread F. In Dungey's model, the gravitational acceleration $\mathbf{g}$ is the only destabilising force. It is quite clear in (2.8) that gravity is a destabilising force, but not the only one. The ambient electric field $\mathbf{E}$ and the neutral winds $\mathbf{U}$ can also contribute under favourable geometric condition. The zero-order density gradient term does not contribute, since $\nabla n \times \mathbf{B}$ is always perpendicular to the background density gradient and can never contribute in moving the lower density plasma up the gradient and the higher density plasma down the gradient to generate waves. The generalised gradient drift instability takes all the destabilising terms into account. This is particularly important for the high-latitude ionosphere as here $\mathbf{g}$ is nearly parallel to the geomagnetic field $\mathbf{B}$ and hence $\mathbf{g} \times \mathbf{B}$ is negligible. The neutral wind $\mathbf{U}$ can be readily included if we use the electric field measured in the neutral frame of reference, given by $\mathbf{E}' = \mathbf{E} + \mathbf{U} \times \mathbf{B}$. Thus, at high-latitudes, the generalised gradient drift instability becomes the generalised $\mathbf{E} \times \mathbf{B}$ instability.

A schematic illustration is shown in figure 2.3 of the generalised $\mathbf{E} \times \mathbf{B}$ instability. When the geometry condition is satisfied any initial perturbations are very likely to produce a polarised electric field $\delta\mathbf{E}'$ due to charge separation produced by the Pedersen current $\sigma_p\mathbf{E}'$. The resulting electromagnetic force $\delta\mathbf{E}' \times \mathbf{B}$ drives the lower density plasma up the gradient and higher density plasma down the gradient. Thus, the initial perturbations in density are amplified by the instability. For the high-latitude F-region ionosphere, the geometry condition is given by

$$(\mathbf{E}' \times \mathbf{B}) \cdot \nabla n > 0 \qquad (2.13)$$

where $\mathbf{E}'$ is the electric field measured in the neutral frame of reference, $\mathbf{B}$ the magnetic field and ∇n the background zero-order density gradient. A good example of this geometry condition is given by a series of satellite data (figure 2.4), in which there is a

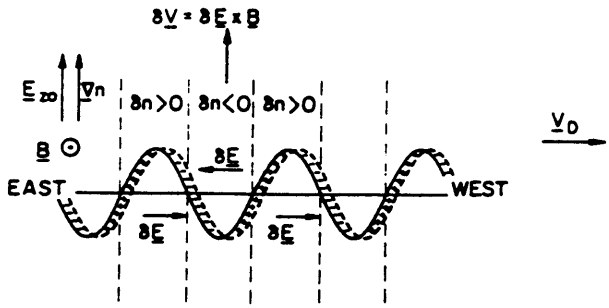

Figure 2.2 Schematic diagram showing the (E-region) gradient drift process for daytime conditions

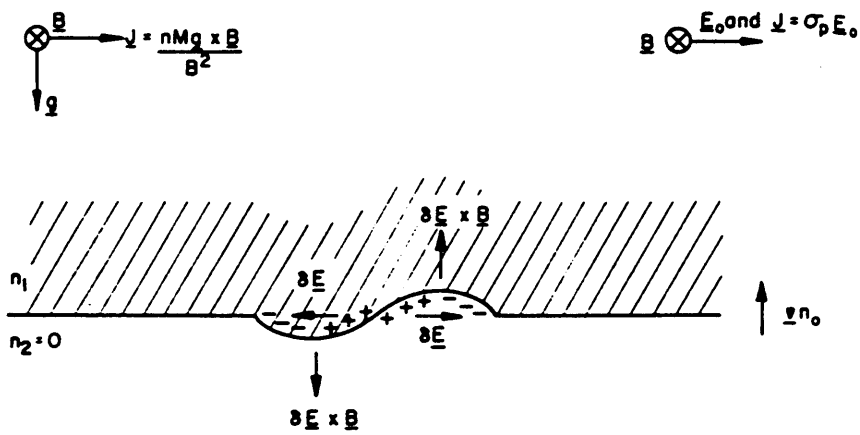

Figure 2.3 Schematic diagram of the generalised **E×B** instability at high-latitudes (or the Rayleigh-Taylor instability at equatorial F-region)

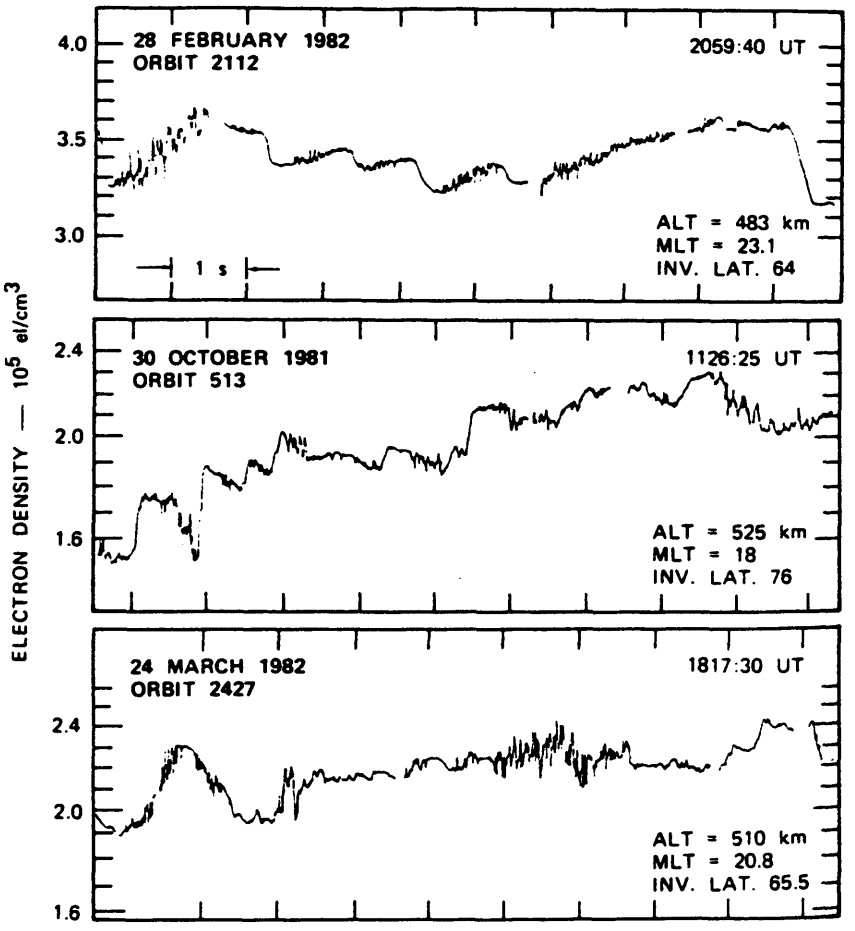

Figure 2.4 Examples of satellite data showing the preferential structuring of plasma density enhancements on gradients of a particular sign

[After Cerisier *et al.*, 1985]

clear preferential structuring of plasma density enhancements on gradients of a particular sign. In fact, the F-region generalised $\mathbf{E} \times \mathbf{B}$ drift instability is quite similar to the E-region gradient drift instability. The main difference is that in the F-region the polarised electric field is produced by the Pedersen current, whereas in the E-region it is mainly produced by the Hall current.

2.4.3 Waves of shorter wave-lengths

The wavelengths of F-region density irregularities which have frequently been observed by ground-based HF coherent backscatter radars are, in general, shorter than that of the waves generated by the generalised $\mathbf{E} \times \mathbf{B}$ drift instability. It is suggested that it is very likely that secondary waves of shorter wavelengths are generated through cascading processes in a manner similar to neutral turbulence, but of much more complexity (Kelley and Heelis, 1989).

2.4.4 Slow phase velocity

In searching for the origin of those waves responsible for the Doppler shift of the radar received signals, comparisons were carried out by Ruohoniemi *et al.* (1987) of simultaneous measurements made with both HF coherent and incoherent scatter radars at Sondre Stromfjord, figure 2.5. Two data sets show quite good agreement which implies that in plasma frame of reference the wave phase velocity is quite small. This is because the coherent scatter radar measures the phase velocity of plasma waves, whereas the incoherent scatter radar measures the velocity of ion-drift. In this sense, in the F-region, the phase velocity measured by a ground-based HF coherent scatter radar could be taken as plasma drift velocity in that region.

2.5 SUMMARY

To summarise, this chapter gives a brief review of the theory and radar studies of the plasma instabilities in the high-latitude ionosphere. Some concepts will be used in later

chapters, such as the geometry consideration for HF radar coherent detection of F-region irregularities in the high-latitude ionosphere.

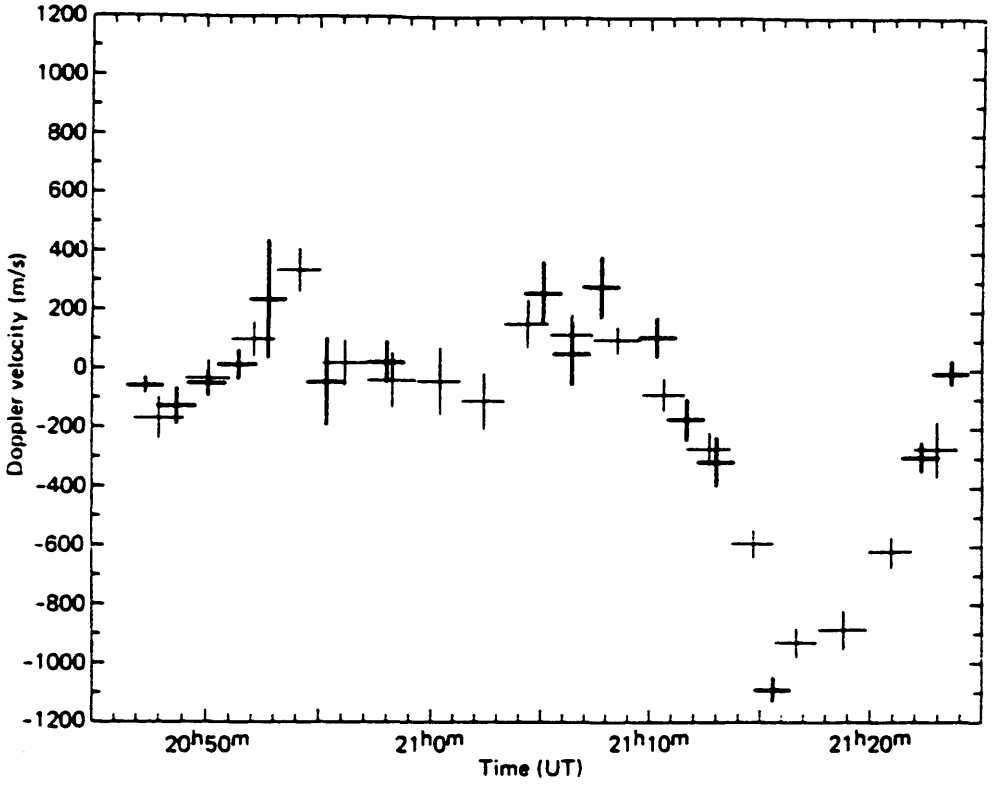

Figure 2.5 Comparison of time series data for HF (heavy crosses) and incoherent scatter (light crosses) velocity estimates calculated for the returns received from the nearby volumes. [After Ruohoniemi *et al.*, (1987)]

CHAPTER 3

COHERENT SCATTERING AND DETECTION

3.1 INTRODUCTION

In both equatorial and high-latitude ionospheric regions, pronounced radar backscatter is frequently received from small-scale ionospheric irregularities. This fact implies the possibility of studying the ionospheric small-scale dynamics using ground-based radar systems. Perhaps the first use of radio techniques to study irregularities was the work of Berkner and Wells who used an ionosonde to study spread F (1934) and sporadic E (1937) in the equatorial region. The use of techniques other than ionosondes to investigate ionospheric E-region irregularities probably started with investigations of the radio aurora (Collins and Forsyth, 1959). Harang and Stoffregen (1938, 1961) were the first to observe and describe the scattering of VHF radio waves (on communication circuits). An outline of the theory of coherent scattering of radio waves from ionospheric irregularities was initiated by Booker (1956) and extended by Walker *et al.* (1986). The analysis of scattering in terms of plasma waves developed by Farley (1963), Buneman (1963), Rogister and D'Angelo (1970), and others, is summarised and compared with experimental results by Fejer and Kelley (1980) in a comprehensive review of ionospheric irregularities. Detailed discussion of ionospheric radar techniques can be found in the handbook for Middle Atmosphere Program (Fukao, 1989) and Radio Techniques for Probing the Terrestrial Ionosphere (Hunsucker, 1991). This chapter is not intended to go through the detailed theory of coherent scattering and radar techniques. It only discusses those principles of coherent scattering and radar techniques which will be used in discussions of later chapters.

3.2 CLEAR-AIR RADAR SCATTER

The clear-air radar scatter from the ionospheric region is believed to be caused by small fluctuations of refractive index, which are in turn caused by the fluctuations of electron density in that region. For a plane electromagnetic wave incident upon a scattering volume v, which is large compared to the wavelength of the incident radar signal and small enough to ensure the statistical uniformity, the electric field of the scattered wave is given by (Haldoupis, 1989)

$$E_s(t) \propto \int_v \Delta n(\mathbf{r},t)\exp(-j(\mathbf{k}_i - \mathbf{k}_s)\cdot\mathbf{r})d^3\mathbf{r} \tag{3.1}$$

where $\Delta n(\mathbf{r},t)$ is the fluctuation of electron density from the background, $\mathbf{k}_i$ and $\mathbf{k}_s$ are wave vectors of incident and scattered radar signals, respectively. The integral of (3.1) is a Fourier spatial wave component of $\Delta n(\mathbf{r},t)$ with wave vector $\mathbf{k} = \mathbf{k}_i - \mathbf{k}_s$. In other words, the electric field of the scattered wave is proportional to a particular Fourier spatial wave component of the fluctuations of electron density. In the backscatter case, because $\mathbf{k}_s = -\mathbf{k}_i$, then

$$\mathbf{k}_i = \frac{\mathbf{k}}{2} \tag{3.2}$$

Therefore, for backscatter detection, radar signals scatter from a particular Fourier spatial wave component of ionospheric irregularities, provided that (3.2) is satisfied.

3.3 FIELD-ALIGNED DENSITY IRREGULARITIES

Having established the concept that for backscatter detection a radar identifies one particular spatial wave component of electron density structures (irregularities) in the ionosphere, it is now pertinent to take a closer look at the ionospheric scattering agents, small-scale electron density irregularities produced by various ionospheric instability mechanisms. Because of the existence of the external magnetic field, the ionospheric plasma is no longer isotropic electrically. Charged particles move very easily along the imposed external field direction, but not across it. This anisotropic nature makes the

ionospheric plasma tend to form structures elongated along the external magnetic direction when it is disturbed. Now if we assume that the field-aligned density structure has an autocorrelation function which is also field-aligned and may ideally be taken as a pencil-like function $\rho(\mathbf{r},\tau)$, we can then investigate the power spectrum of this field-aligned structure. Note that this is a very idealised picture, since there is nothing like typical pencil-like structure. The power spectrum of the density structure is simply a Fourier transform of the autocorrelation function $\rho(\mathbf{r},\tau)$, for the spatial Fourier transform, this is

$$\Phi(\mathbf{k},\tau) = \frac{1}{(2\pi)^3} \int_{-\infty}^{\infty} \rho(\mathbf{r},\tau) \exp(-j\mathbf{k}\cdot\mathbf{r}) d^3\mathbf{r} \tag{3.3}$$

where $\mathbf{k}$ is the wave vector of the Fourier spatial wave components. It is not difficult to envisage the general shape of the power spectrum $\Phi(\mathbf{k},\tau)$ in $\mathbf{k}$-space, since the Fourier transform of a pencil-like function is a pancake-like function. That means, if the ionospheric small-scale irregularities are elongated along the earth's magnetic field lines, the wave vectors of the main spectral components (Fourier spatial wave components) should be very close to perpendicular to the local geomagnetic field lines, i.e. $\mathbf{k}$ should be very close to perpendicular to $\mathbf{B}$. Therefore, equation (3.2) suggests that for backscatter detection the radar probing wave vector $\mathbf{k}_i$ should also be very close to perpendicular to the earth's magnetic field lines, the so-called orthogonality condition required for the coherent detection of field-aligned irregularities.

If there is any dynamic process in the medium associated with the density structure, it can be revealed by the temporal Fourier transform of $\Phi(\mathbf{k},\tau)$, which is given by

$$\Phi(\mathbf{k},\omega) = \frac{1}{(2\pi)} \int_{-\infty}^{\infty} \Phi(\mathbf{k},\tau) \exp(-j\omega\tau) d\tau \tag{3.4}$$

where ω is the frequency of temporal oscillation associated with each spatial wave component in the spectrum. Then, the phase velocity of each spatial wave component is given by

$$V = \frac{\omega}{|\mathbf{k}|} \tag{3.5}$$

The above discussions, (3.2) and (3.3), suggest that for backscatter detection a radar can only receive ionospheric scatter from regions where orthogonalities are achieved between the radar probing wave vectors and the local geomagnetic field lines. The Doppler signature, given by (3.4) and (3.5), provides dynamic information on how fast the density structure changes with time.

3.4 RADAR FREQUENCIES AND GEOMETRY CONSIDERATION

The basic principle discussed in the above two sections on radar backscatter detection of field-aligned small-scale irregularities in the ionosphere is that radars can only see irregularities in those regions where the orthogonality condition is achieved between the radar probing wave vectors and the local geomagnetic field lines. At high-latitudes, the earth's magnetic field lines are nearly vertical, and therefore, there is no difficulty for a ground-based VHF or UHF radar to achieve the required orthogonality condition in the E-region, as rays should propagate nearly in straight line at these frequencies. In the F-region, because of lack of ionospheric refraction at the VHF and UHF frequencies, it is practically very difficult for radar waves at these frequencies to reach the orthogonality condition for radar backscatter detection. This is why historically most early radar studies of F-region irregularities have been confined to low and mid-latitudes where the requisite orthogonality condition can be easily achieved since the earth's magnetic field there is nearly horizontal.

Ionospheric refraction, however, does become important at HF frequencies. Taking advantage of this, a new approach to coherent backscatter utilising radars operating at HF frequencies has been developed. At these lower frequencies ionospheric refraction allows the orthogonality condition to be satisfied in both the E- and F- region of the ionosphere as illustrated in figure 3.1. The nearly vertical magnetic field lines at high-latitudes lead to non-orthogonal scattering at VHF and higher frequencies with the scattered signals propagating into space. In contrast, the refraction which occurs at HF

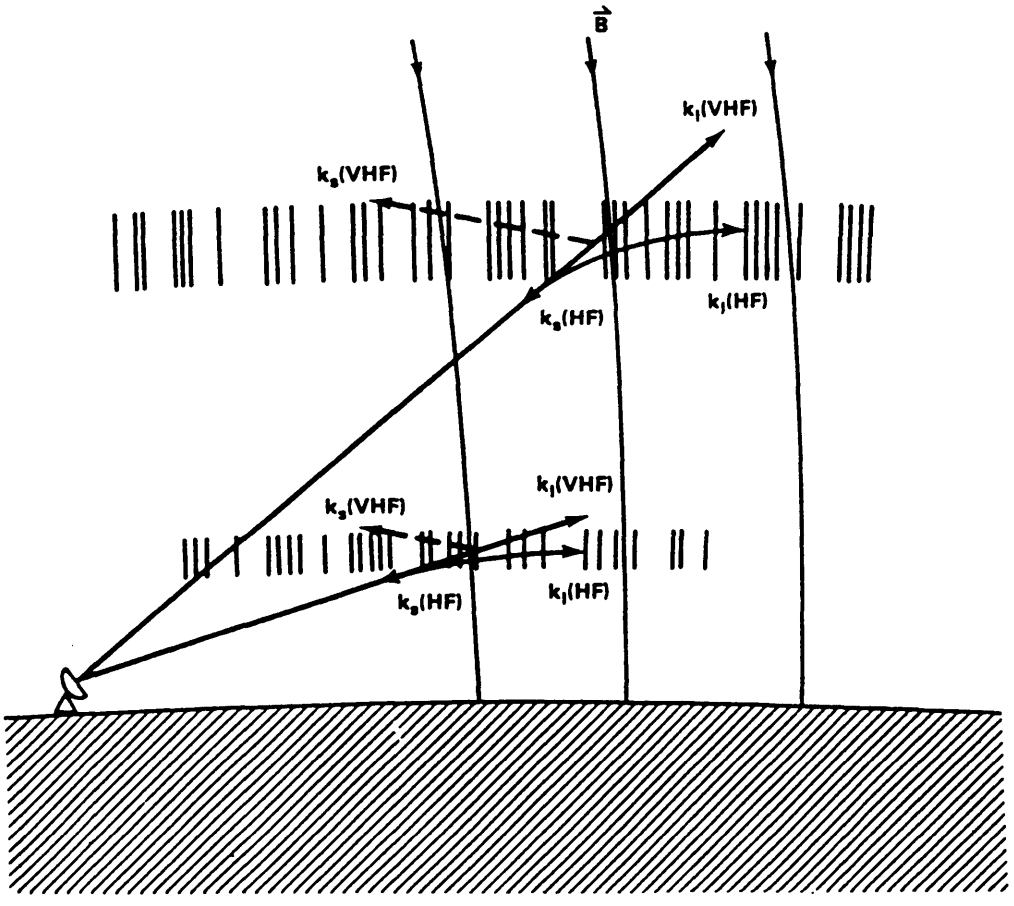

Figure 3.1 Schematic diagram showing that VHF and higher frequency radio waves can achieve orthogonality with the earth's magnetic field lines in the E-region, whereas HF radar signals can satisfy the orthogonality condition in both the ionospheric E- and F- regions.

frequencies causes the radar signals to become orthogonal to the magnetic field lines. If there were ionospheric irregularities in these regions, they would backscatter the radar signals back to the radar site. In other words, radars operating at VHF or UHF frequencies are good for backscatter detection in the high-latitude E-region, whereas radars operating at HF frequencies are generally good for both the E- and F- regions.

3.5 COHERENT SCATTERING

The field-aligned ionospheric density irregularities discussed in section 3.3 are large enough in space for the scattered waves to be coherent in phase. The constructive interference of these scattered waves means that the final radar echoes are strong enough to be detectable by a relatively low powered ground-based radar system. This scattering is referred to as coherent scattering. Therefore, the geometry consideration is very important for coherent backscatter detection. All the modelling study to be discussed in later chapters of this thesis is wholly based on this model of coherent backscattering from field-aligned density irregularities. If off orthogonality, the radar signals are then mainly backscattered by the background thermal fluctuations, the lowest level fluctuations in plasma density. This scattering is known as incoherent scattering in contrast to coherent scattering. Incoherent scattering is not a subject for this thesis. The interested reader is therefore referred to International School on Atmospheric Radar (Fukao, 1989) and Introduction to Incoherent Scatter Measurements (Nygren, 1996).

3.6 BASIC CONCEPTS OF RADAR DETECTION

Radar is a very broad concept. It includes anything to do with radio ranging and detection. Detailed discussion on radar techniques can be found in Radio Techniques for Probing the Terrestrial Ionosphere (Hunsucker, 1991) and International School on Atmospheric Radar (Fukao, 1989). For the modelling study to be discussed in later chapters, some basic radar concepts are introduced below.

3.6.1 Ray group path, phase path, and Doppler velocity

It is well known that the speed of electromagnetic waves in free space is the same as the speed of light c. If we can ignore the small difference between the speed of electromagnetic waves in free space and that in the ionosphere, then the time of flight of a radar signal from the radar transmitting antenna to target multiplied by the speed of light gives a rough estimate of the distance of the target from the radar site. This 'distance' is referred to as the group path, which is slightly longer than the geometrical ray path length. Because it is easy to calculate and convenient to use, the ray group path is widely used in radar engineering for measuring the 'distance' of radar target.

Besides the group path, another very important parameter widely used in radar techniques is the ray phase path, which gives an equivalent ray path in free space for the same amount of phase shift in the ionosphere. The rate of change of the phase path gives the Doppler shift, the dynamic information of the radar target. For our coherent backscatter detection of field-aligned density irregularities, the Doppler information gives the phase velocity of irregularities, equation (3.5). When using radar techniques to investigate a dynamic process of a distributed target such as the density fluctuations in the ionosphere, spectral width proves to be a parameter of interest. The spectral width is a parameter which measures another aspect of a dynamic process, random turbulence in the plasma motion. Both the Doppler shift and spectral width are used extensively in the interpretation of radar observations of small-scale ionospheric dynamics.

3.6.2 Range and range resolution of a pulsed radar

In practice, the radar signals are normally modulated with a series of pulses and each pulse has a finite duration called pulse-width. If the time of flight for such a pulse from the radar to a stationary point target and then back to radar is t, the range (group path) of this point target from the radar is given by

$$r = \frac{ct}{2} \tag{3.6}$$

Because pulses are employed to modulate the radar signals, no matter how narrow they are, each pulse has a finite duration, say $\Delta\tau$, which can readily be interpreted in terms of range known as range resolution, given by

$$\Delta r = \frac{c\Delta t}{2} \tag{3.7}$$

Range resolution is a radar parameter which gives the minimum distance in group path within which the pulsed radar can not distinguish between any two targets. Figure 3.2 gives a schematic illustration, showing the basic idea of range, range resolution, and aliasing.

3.6.3 3D schematic view of radar received signals

Equation (3.6) gives an easy way of measuring the range of a stationary point target using a pulsed radar. When a train of pulsed signals is transmitted from a radar antenna and backscattered from a distributed target, the radar echoes can be best illustrated in a three-dimensional plot shown in figure 3.3, in which the vertical axis is the intensity of radar scatter, and the other two axes are time. One is the time of pulse transmission (t), the (discrete) time at which the pulse was transmitted, and the other is the delay time after the time of pulse transmission (t'). This 3D plot gives a very clear schematic view of radar backscattered signals when an equal-interval pulse scheme is used to modulate the radar signals. Nowadays, this equal-interval pulse scheme is not popular in radar practice, a more complex pulse scheme such as a multi-pulse modulation is used in stead. However, even if a complementary multi-pulse transmission has been used, after filtering and decoding of radar received backscattered signals, we can still talk about identical pulses and use figure 3.3 to interpret the radar backscatter. The broken line in figure 3.3 shows how the intensity of radar scatter at a given range changes with time.

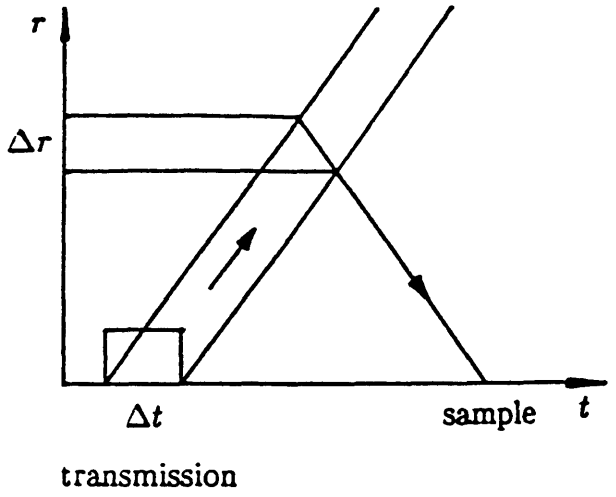

Figure 3.2 Time-height section showing the relation of the size of a range-cell and the length of a pulse for distributed targets

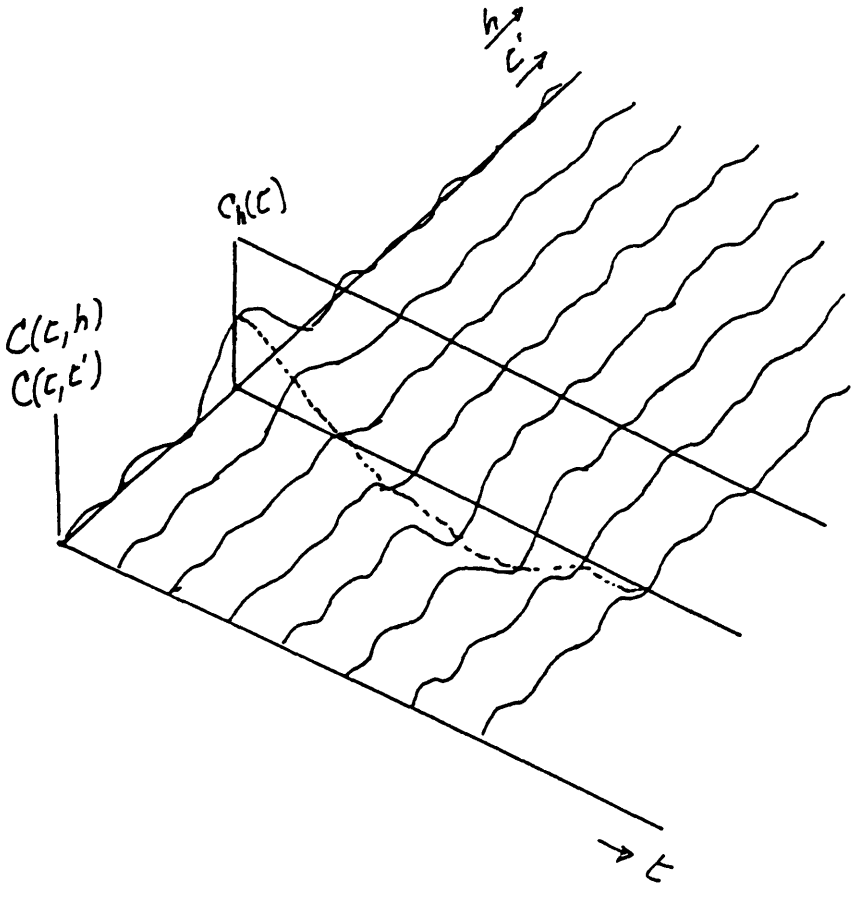

Figure 3.3 A 3D view of radar received signals

3.7 SUMMARY

This chapter discusses a number of important concepts on coherent scattering of radar signals from field-aligned ionospheric irregularities. It is stressed that small-scale density irregularities in the ionosphere are field-aligned and the geometry consideration is important for the coherent detection of radar backscattered signals. It is pointed out that radars identify only one particular spatial wave component of the density structures instead of the whole spectrum. A brief discussion is also given on some basic radar concepts which will be used in later chapters.

CHAPTER 4

JONES3D AND ITS MODIFICATIONS

4.1 INTRODUCTION

The research work presented in this thesis is mainly concerned with a computer modelling study of HF coherent detection of field-aligned small-scale irregularities in the high-latitude ionosphere. The study relies heavily on computer modelling of the propagation of HF radio waves through various realistic high-latitude ionospheres. To do this, a powerful three-dimensional ray tracing computer programme, Jones3D (Jones and Stephenson, 1975), has been modified. The modified version is capable of computing not only the usual HF ray paths and relevant parameters through an ionosphere, but also the potential positions of field-aligned small-scale irregularities in the high-latitude ionosphere, which could be detectable by a ground-based HF coherent radar system. This chapter describes the ray tracing programme, and the modifications made to the programme.

4.2 RAY TRACING MODELLING

Ray tracing provides a method of calculating the ray paths and other relevant ray parameters step by step through a medium in the time-domain. The technique is wholly based on ray theory rather than the wave approach. Tracing rays through an ionosphere is in principle similar to those used in other branches of wave propagation, such as optics and atmospheric waves, except for the anisotropic nature of the ionosphere. The problems associated with tracing rays through anisotropic media have been extensively

discussed by Booker (1949), Haselgrove (1955), Kelso (1964), Jones (1968), Jones and Stephenson (1975), and Budden (1985) and several useful ray tracing methods have been developed (e.g. Booker, 1949; Haselgrove, 1955). These methods require the so-called step-by-step integration of a set of simultaneous differential equations.

4.3 THE JONES3D PROGRAMME

The Jones3D programme is one of the most widely used ray tracing computer programmes for radio waves in the ionosphere. For example, it has been used to trace HF rays at high-latitudes using measured meridional electron density distributions (Villain, *et al.*, 1984), to locate the SAFARI HF radar echoes (Villain, *et al.*, 1985), to simulate the effect of atmospheric gravity waves on the Goose Bay HF radar observations (Samson, *et al.*, 1990), and to investigate OTH equatorial spread Doppler clutter problems (Anderson, *et al.*, 1996). The Jones3D programme was developed by Jones (1968) and described by Jones and Stephenson (1975). It is a versatile three-dimensional ray tracing computer programme, solving a set of six simultaneous differential equations and capable of computing not only the ray paths through an ionosphere, but also a number of other useful ray parameters, such as group path, phase path, Doppler shift, absorption, and polarisation.

4.3.1 Main features

The main features of the Jones3D programme are summarised in table 4.1.

Table 4.1 Main features of Jones3D

coordinate systems	• geographic • computational
magnetic field models	• constant dip and gyrofrequency • constant dip with gyrofrequency proportional to $1/R^3$, $R=R_E + h$, where R_E is the earth radius and h the height above the surface

	• earth-centred dipole model • spherical harmonic expansion
models of profile of electron density	• TABLEX for tabulated electron density profile, which can be calculated from ionogram reduction or from EISCAT measurement • Chapman layer, with tilts, ripples and gradients • Chapman layer with variable scale height • two Chapman layers with tilts • linear model • plain or quasi parabolic • bulge, analytical model of equatorial F2 layer • exponential model
models of perturbation in electron density	• torus • double torus • trough, increase in electron density at any latitude • increase in electron density produced by shock wave • gravity wave perturbation • gravity wave type 2 • spherically symmetric cloud (added at Leicester Ionospheric Physics Group) • TID -- horizontally stratified ionosphere (added at Leicester) • Gaussian density perturbation
models of collision frequency	• TABLEZ for tabulated profile of collision frequency • constant collision

	• exponential profile • combination of two exponentials
numerical scheme	time-domain 4th order Runge-Kutta/Adams-Moulton approach with variable step-length

4.3.2 Discussion

The Jones3D programme uses two coordinate systems, the geographic and computational. The geographic coordinate system is used only for the initial model inputs and the computational coordinate system is used for the ray tracing computation.

In Jones3D, there are a number of built-in magnetic field models available for different purposes of ray tracing modelling (see table 4.1). When the earth-centred magnetic dipole field is used, the computational coordinate system is eventually the same as the magnetic coordinate system.

Generally, to trace rays through an ionosphere, the most important thing to specify is the vertical distribution of electron density in the ionosphere. Jones3D provides a number of analytic and numerical models to simulate different ionospheric situations. For example, to investigate the propagation of radio waves under realistic ionospheric conditions, TABLEX is the best choice.

It is possible to trace rays through an ionosphere using Jones3D when some ionospheric perturbation exists. A variety of electron density perturbation models are available within Jones3D to assist the investigation of the effect of ionospheric perturbations on radio wave propagation. Thus, one can trace rays using Jones3D through a normal ionosphere either with or without one of the built-in ionospheric perturbation models. This mechanism offers a great flexibility to tackle various ionospheric situations.

There are also several models of electron collision frequency to choose from within Jones3D if the collision effect is taken into account in the computation of the radio refractive index (see table 4.1).

In Jones3D, a set of six simultaneous differential equations is integrated step by step in the time-domain by a numerical scheme known as the 4th order Runge-Kutta/Adams-Moulton approach. The integration step-length is variable and self-adjusted by a built-in accuracy-checking mechanism. In every two successive integration steps, if the result is found to be too accurate, Jones3D doubles its integration step-length and recomputes that integration; if the result is poorer than a predefined error tolerance, then Jones3D halves the step-length and repeats the integration.

4.4 MODIFICATIONS TO JONES3D

As mentioned above, the research work presented in this thesis relies heavily on the modelling of HF propagation through various high-latitude ionospheres. Some problems in the Jones3D code were identified and solved whilst modifications to the code were also made to suit the purpose of this research work.

4.4.1 Fitting the model input profile of electron density

The Jones3D programme is able to use either an analytic (such as Chapman layer, parabolic layer, etc.) or a numerical ionospheric model (such as that calculated from ionograms or EISCAT measurements) to trace rays through an ionosphere. When a numerical ionosphere is used, Jones3D fits a vertical curve to the (numerical) discrete data points and extrapolates both upwards and downwards in altitude to get a complete profile. The extrapolated top-side ionosphere is the same in electron density as the top of the input numerical ionosphere. The bottom-side profile is computed exponentially downwards to the surface of the earth using the lowest two data points of the numerical ionosphere.

During the course of the modelling, it was found that the built-in scheme of data fitting and extrapolation in TABLEX is not good enough. Occasionally, the scheme causes enormous difficulty and no rays can be launched at all. The main reason is that the vertical curve fitting and extrapolation scheme in TABLEX extrapolates the bottom-side profile of electron density exponentially downwards to the surface of the earth using the lowest two data points of the input numerical ionosphere. These two data points are, therefore, vitally important in determining the gradient of the downward exponential extrapolation. Using this curve fitting and extrapolation scheme in TABLEX, there could be four possibilities.

(1) When the lowest data point of an input numerical profile is much smaller than the second lowest point in electron density, the downward exponential extrapolation works well. It gives a reasonable bottom-side profile of electron density down to the surface of the earth.

(2) If the lowest data point is not very much smaller than the second lowest point in electron density, then the extrapolated profile of electron density below 60 km altitude could still be significant. For example, the electron density at 60 km altitude could be only one order less than that of the lowest point. This situation happens very often.

(3) If the lowest data point is of more or less the same value as the second lowest point in electron density, then the extrapolated electron density on the ground would be more or less of the same value as the lowest data point of the input numerical ionosphere.

(4) If the lowest data point is greater than the second lowest data point in electron density, the extrapolated bottom-side profile of electron density increases with decreasing height. This situation results in no rays being launched at all, as they are reflected back to ground when they are launched. This point will be further discussed in chapter 7 where the EISCAT CP1 data measured in Tromso (Norway) are used for the model inputs of realistic ionospheric conditions.

In resolving the above difficulty of fitting an input numerical ionosphere, it has been noticed that adding an extra data point of zero electron density at 60 km altitude will result in a somewhat oscillating bottom-side profile with a few points of negative electron density. This proves not to be a good way to solve the problem.

A good way of tackling the problem is to use a Gaussian-like function instead of exponential. The advantage of using a Gaussian function is based on the fundamental difference between Gaussian and exponential. First of all, a Gaussian is everywhere differentiable, which makes the final fitted profile of electron density (to Jones3D) numerically better than that fitted by an exponential scheme. Secondly, compared to an exponential, a Gaussian decreases more slowly at the beginning and much faster at the end. Furthermore, the width of a Gaussian function is controllable. It is, therefore, possible to extrapolate the bottom-side profile of electron density with the lowest two data points.

Using a Gaussian-like function, the bottom-side profile of electron density is now given by

$$N = N_p e^{-\frac{(H-Hp)^2}{\sigma^2}} \tag{4.1}$$

where (N_p, H_p) is the peak of this Gaussian-like function, with N for electron density and H for height. Assuming the lowest and second lowest data points of an input numerical ionosphere are (N_1, H_1) and (N_2, H_2), respectively, two cases should be considered, one is N_1 less than N_2 and the other is N_1 greater than or equal to N_2.

For $N_1<N_2$, both (N_1, H_1) and (N_2, H_2) are used to compute the bottom-side profile of electron density, which is given by

$$N = N_2 e^{-\frac{(H-H_2)^2}{\sigma^2}} \quad , \quad H \leq H_1 \tag{4.2}$$

where $\sigma = \sqrt{\dfrac{(H_1 - H_2)^2}{\ln(\frac{N_2}{N_1})}}$

Thus, above the height of the lowest data point, (N_1, H_1), the fitted numerical profile of electron density is used. Below this height, the bottom-side profile is computed using equation (4.2).

When $N_1 \geq N_2$, in order to keep the first order derivative of the computed profile of electron density continuous, we add one extra data point (N_o, H_o) at 60 km altitude and still use two data points, (N_1, H_1) and (N_o, H_o), to compute the bottom-side profile of electron density, assuming that (N_1, H_1) is at the peak of this downward Gaussian profile. It is well known in ionospheric physics that N_o should be very small at 60 km altitude. Here, N_o is set to 100 cm^{-3}. Thus,

$$N = N_1 e^{-\frac{(H-H_1)^2}{\sigma^2}}, \quad H \leq H_1 \tag{4.3}$$

where $\sigma = \sqrt{\dfrac{(H_1 - H_o)^2}{\ln(\frac{N_1}{N_o})}}$, $N_o = 100$ (n/cm^3), $H_o = 60$ (km)

An example of the comparison between the exponential and Gaussian extrapolation is illustrated in figure 4.1, in which the top panel shows an input numerical ionosphere, based upon CP1 data from the EISCAT UHF experiment in Tromso. The middle panel gives the fitted ionosphere with the bottom-side profile extrapolated by the exponential scheme. The bottom panel shows the fitted ionosphere with the bottom-side profile extrapolated by the Gaussian-like function (4.1). It is seen that, although the input CP1 data has a very well shaped bottom-side profile of electron density (top panel), the exponentially extrapolated electron density on the ground is still unrealistically too large (middle panel). This result implies that the exponential extrapolation scheme in TABLEX is not good for ray tracing modelling using realistic ionospheric data, unless the extrapolation of the bottom-side profile is improved. In contrast to the exponential scheme, the Gaussian extrapolation gives a very reasonable bottom-side profile of electron density, which decreases smoothly downwards to 60 km altitude. The electron

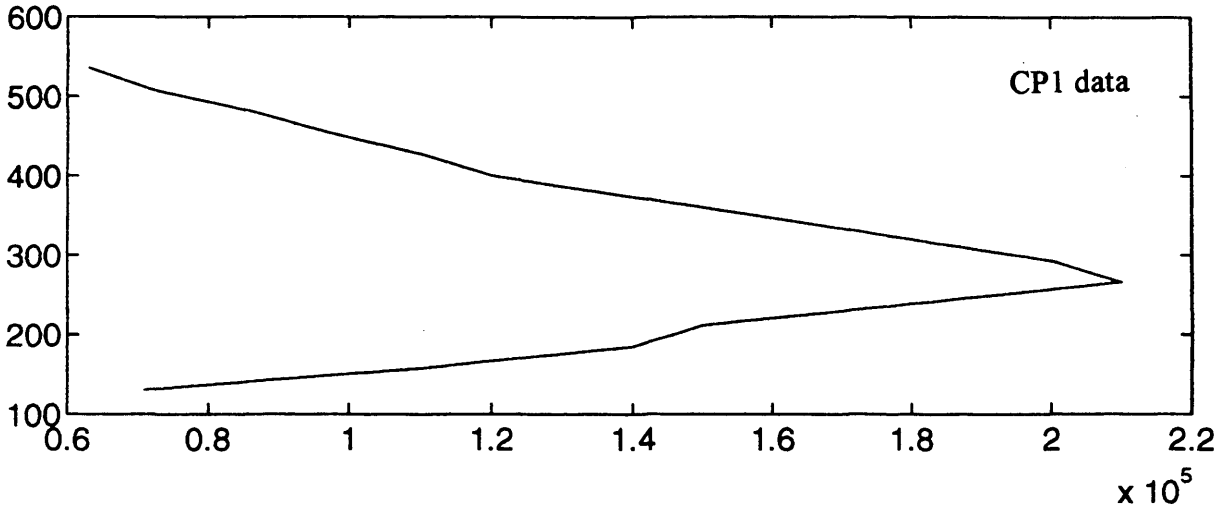

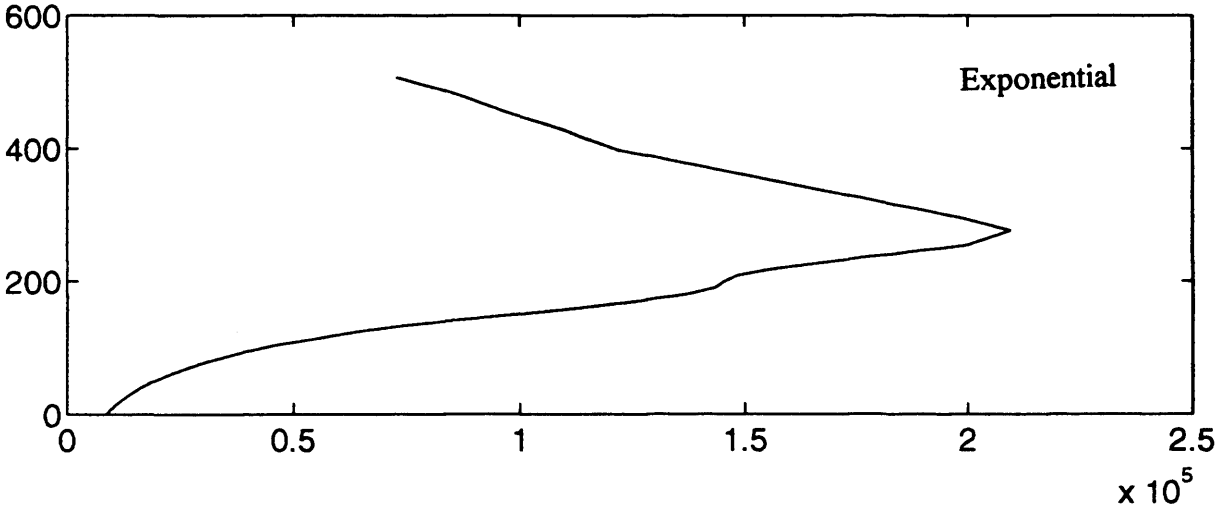

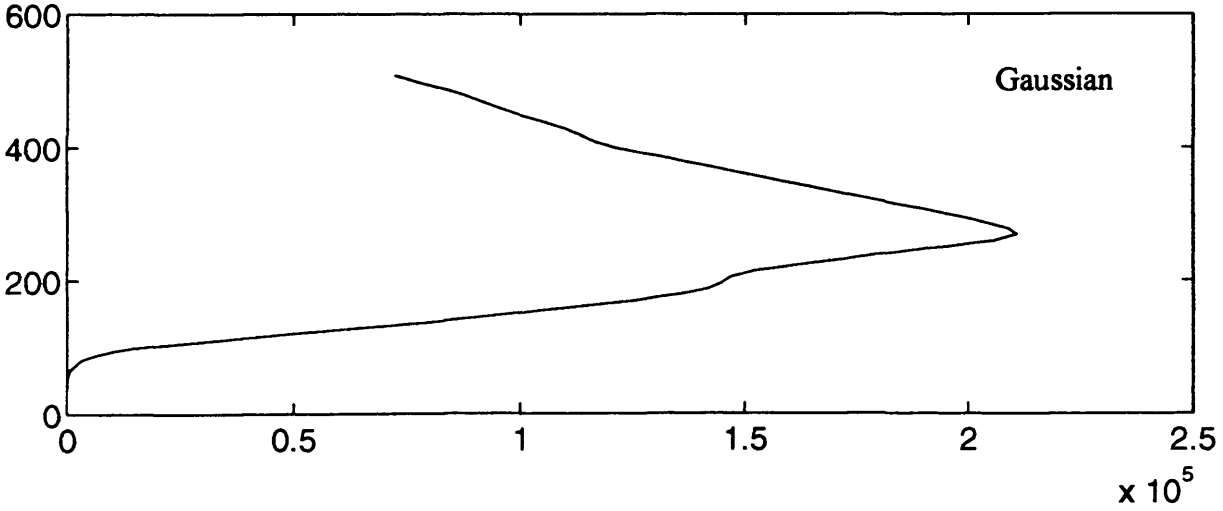

Figure 4.1 TABLEX extrapolation scheme

density below 60 km is very small and can be taken as zero. This is what is expected in ionospheric physics.

A similar extrapolation problem exists with the numerical model of electron collision frequency, TABLEZ, and should be tackled in exactly the same way as that discussed above for the electron density extrapolation for TABLEX.

4.4.2 Orthogonal detection of density irregularities

According to plasma physics, small-scale density irregularities in the ionosphere are generated and sustained by plasma instabilities in the E- and F- regions, and are in general elongated along the earth's magnetic field lines (see chapter 3). In other words, their spatial wave vectors should be very close to perpendicular to the earth's magnetic field **B**. Thus, for wave-wave scattering, as discussed in chapter 3 (coherent scattering and geometry consideration), a ground-based coherent scatter radar can only receive backscattered signals from those regions where orthogonalities are achieved between the radar probing wave vector **k** and the local geomagnetic field **B**. For convenience the term 'orthogonal detection' is used for coherent backscatter detection. In our ray tracing modelling, the criterion used for the ray orthogonal detection of field-aligned irregularities is that when the angle of ray wave vector **k** to the local geomagnetic field **B** is within one degree of perpendicularity, i.e. within 89 to 91 degrees, orthogonality is assumed.

When plotting, small vertical bars are used to indicate where orthogonalities are achieved between the ray wave vectors and the local geomagnetic field lines.

Theoretically, if the density fluctuation level in an ionospheric region is high enough and equation (3.2) is also satisfied, irregularities in this region are generally detectable by ground-based coherent backscatter radar systems. The ray orthogonal detection discussed above gives the ray tracing prediction of all possible locations from where backscattered radar signals might be received. In this sense, the ray orthogonal

detection can be used to simulate the coherent radar backscatter detection of field-aligned small-scale irregularities in the ionosphere.

4.4.3 Penetration of the F2 peak

The Jones3D programme was originally written for a ground-based HF radio communication system with both transmitter and receiver located on the ground. Thus, when the ionospheric F2 peak is penetrated, Jones3D either stops tracing the ray any further or switches to trace another ray at the next elevation/azimuth angle. This is clearly illustrated in figure 4.2, in which small vertical bars are used to indicate orthogonalities with the earth's magnetic field lines. Once the peak is penetrated, either as shown in the top panel Jones3D stops tracing the ray any further or as seen in the middle panel the programme switches to trace another ray at the next elevation/azimuth angle. However, it is known that field-aligned small-scale density irregularities can be generated and sustained above the F2 peak. Therefore, in order to simulate HF radar coherent detection of these density irregularities, the Jones3D programme has been modified in such a way that it is able to trace the rays up to any user specified height of interest. An example produced by the modified version of Jones3D is shown in the bottom panel of figure 4.2. It demonstrates that orthogonalities above the F2 peak are computed by the modified version of Jones3D.

4.4.4 Upper and lower height limits for the computation of orthogonalities

Both theoretical studies and radar observations show that field-aligned small-scale irregularities in the ionosphere are mainly confined in the ionospheric E- and F- regions (Kelley and Heelis, 1989; Greenwald *et al.*, 1995). Lower and upper height limits are therefore introduced for the computation of orthogonalities. Although rays are traced from the radar transmitter height up to the upper height limit, orthogonalities are only computed and plotted between the lower and upper height limits (see figure 4.2). In the modelling study to be discussed in chapters 6 and 7, the lower and upper height limits are set to 90 and 500 km altitude, respectively.

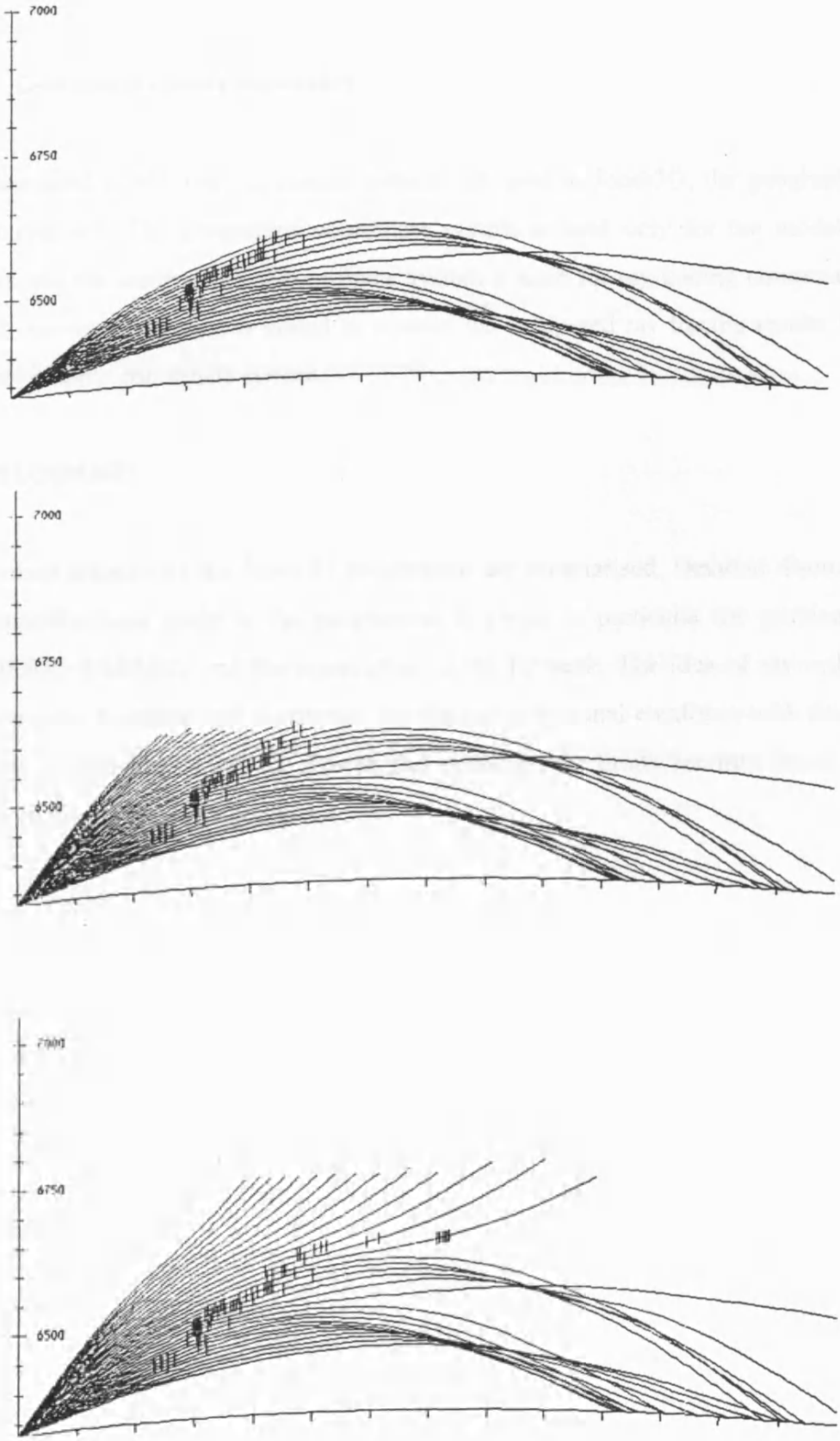

** TROMSO DATA (VERTICAL) CP-2-C 22/04/86 1030 UT **

1 **

F= 8.0000, INI AZ= -50.0000, FIN AZ= -50.0000, ORDINARY

INI EL= 10.0000, FIN EL= 40.0000, 100.0000 KM BETWEEN TICKMARKS

Figure 4.2

4.4.5 Coordinate system conversion

As discussed in 4.3, two coordinate systems are used in Jones3D, the geographic and computational. The geographic coordinate system is used only for the model initial inputs and the computational coordinate system is used for ray tracing computation. A small conversion routine is added to convert the computed ray tracing results back to the geographic coordinate system.

4.5 SUMMARY

The main features of the Jones3D programme are summarised. Detailed discussion of the modifications made to the programme is given, in particular the problems with TABLEX, TABLEZ, and the penetration of the F2 peak. The idea of ray orthogonal detection is discussed and a criterion for the ray orthogonal condition with the earth's magnetic field lines is given. Lower and upper height limits are introduced for the computation of ray orthogonalities.

CHAPTER 5

HF RADAR MODELLING

5.1 INTRODUCTION

A general discussion was given in chapter 4 of the Jones3D programme and the modifications made to the programme to undertake the research presented in this thesis. This chapter discusses HF radar modelling using the modified version of Jones3D. All discussions in this chapter are based on two ground-based HF radar systems, the Halley HF radar in Antarctica and the CUTLASS HF radar in Finland. Discussions are given of the specifications of ray tracing modelling, the preparation of realistic ionospheric conditions, and different modes of radar modelling used in this study.

5.2 MODELLING SPECIFICATIONS OF JONES3D

The versatility of the Jones3D ray tracing programme provides a number of options to serve different purposes of ray tracing modelling (see chapter 4). The modelling specifications of the programme for this research are first listed and then discussed below.

5.2.1 Modelling specifications

The specifications are:

(1) Only O-mode rays are traced.

(2) The earth-centred dipole model is used for the earth's magnetic field.

(3) The profiles of electron density are either computed directly from ionogram data (for the Halley HF radar in Antarctica) or based upon the CP1 data from EISCAT UHF experiment in Tromso (for the CUTLASS HF radar in Finland).

(4) No ionospheric perturbations and no tilts are considered.

(5) A combination of two exponentials is used for the profile of electron collision frequency.

(6) Radio refractive index is computed using the Appleton-Hartree formula with the magnetic field and electron-neutral collisions.

(7) The ray orthogonal condition: when the angle of ray wave vector **k** to the local geomagnetic field **B** is within one degree of perpendicularity, i.e. within 89 to 91 degrees, orthogonality is assumed.

(8) For both physics and computational purposes, ray orthogonalities with the earth's magnetic field lines are only computed and plotted between the user specified lower and upper height limits (see chapter 4). In the modelling study to be discussed in chapters 6 and 7, the lower and upper height limits are set to 90 and 500 km altitude, respectively.

5.2.2 Discussion

When using the Jones3D programme to trace rays through an ionosphere, it is optional to trace either O-mode rays or X-mode rays. Here, we choose O-mode rays based on the fact that the ionospheric absorption of the extraordinary waves is generally greater than that of the ordinary waves. This phenomenon can be seen from conventional ionogram data, which usually show much greater absorption of the X-mode traces than the O-mode traces.

As discussed in chapter 4, the Jones3D programme uses two coordinate systems, the geographic and computational. If the earth-centred dipole model is used for the earth's magnetic fields, the computational coordinate system becomes the same as the magnetic coordinate system. It is advantageous to use this earth-centred magnetic dipole model to investigate events which are organised by the earth's magnetic fields.

The aim of this research is to investigate HF coherent detection of field-aligned small-scale irregularities of the high-latitude ionosphere. To compare with radar observations, it is ideal to trace rays through realistic ionospheres. The realistic profiles of electron density used in the modelling study are either computed directly from ground-based dynasonde data, or based upon EISCAT CP1 data. These will be discussed in later sections.

The angle between radar wave vector **k** and the direction perpendicular to the earth's magnetic field **B** is termed the aspect angle. The aspect sensitivity was one of the first and most important features of auroral radar backscatter to be described (Chapman, 1953). Normally, radar echoes of small aspect angle are expected. This is not only predicted by theory, but also confirmed by VHF radar observations (Haldoupis, 1989). However, radar echoes of large off-orthogonal angle were reported and studied (Leadabrand, *et al.*, 1967; McDiarmid, 1972; Moorcroft, 1985). Radar echoes of large off-orthogonal angle are explained to be caused by tilted layers (Moorcroft, 1989; McDiarmid, 1990), or wave trapping by curved electron density layers (Uspensky, *et al.*, 1994). In this research, no ionospheric perturbations and no tilts are considered. Ray orthogonality is computed when the aspect angle is within one degree of perpendicularity ($89^{o} \sim 91^{o}$).

5.3 ELECTRON DENSITY PROFILE (1) -- HALLEY HF RADAR

To trace HF rays through an ionosphere, the most important piece of information needed is the vertical profile of electron density of the ionosphere. For the Halley HF radar in Antarctica, the realistic ionospheric profiles of electron density above the radar site are computed directly from Halley AIS dynasonde data by the Polynomial Analysis Program (POLAN) (Titheridge, 1985).

5.3.1 AIS dynasonde

The conventional equipment for measuring the virtual height of the ionosphere is a sweep-frequency pulsed radar device called an ionosonde. The basic standard

ionosonde utilises the amplitude of the returned pulse to estimate delay time and does not measure quantitatively the other characteristics of the returned radio frequency pulse, i.e. the exact frequency, phase, polarisation, and the direction of angle of arrival. The early history of ionosondes and their roles in radio science has been reviewed by Villard (1976). The AIS (Advanced Ionospheric Sounder) or dynasonde is a new generation of pulse-amplitude computer-based HF radar system. By using a suitable antenna system, it is capable of measuring the echo amplitude, Doppler shift of irregularities, location of echoes, polarisation of echoes, and has the ability to suppress noise and interference (Grubb, 1979; Wright and Pitteway, 1982). The operation of dynasondes can be grouped into three modes: the ionogram (I) mode, the kinesonde (K) mode, and the basic or intermediate (B) mode (Davies, 1990). In the modelling study of the Halley HF radar (to be discussed in chapter 6), the ionogram (I) mode data are used. The programme used to invert the equivalent vertical profiles of electron density from ionogram data is discussed in the next section.

5.3.2 Polynomial Analysis Program -- POLAN

To compute the vertical distributions of ionospheric electron density from ground-based ionosonde data, there are a number of numerical techniques available for this kind of inversion with the influences of the earth's magnetic field and collisions being considered. Among them, the most comprehensive is the Polynomial Analysis Program, POLAN, developed by Titheridge (1967, 1985).

POLAN is designed for maximum accuracy and reliability and is capable of using both ordinary and extraordinary data points to make possible the estimation of the size of a valley between two ionospheric layers. For general purpose or routine usage, users are not expected to fine tune most of the predefined program parameters, i.e. POLAN can be used as a black-box and the output results are generally good. In this modelling study, however, it has been noticed that some care should always be exercised when interpreting and sampling ionogram data. Some corrections may be needed in order to obtain the best estimation of POLAN inverted profiles of electron density.

5.3.3 Interpretation and sampling of AIS dynasonde data

Some general rules have been set out for the interpretation and sampling of conventional ionogram data (Piggott, *et al.*, 1972; Piggott, 1975). However, great care should always be exercised. This is particularly true for the high latitude ionosphere, as it is quite common for some type of disturbance to be present, e.g. spread F, (auroral) sporadic E, substorm effects, and gravity wave events. Besides, at high latitudes, sometimes there could be tilt or trough effects present in ionogram data. The presence of these disturbances could make the interpretation of ionogram data more difficult and challenging than expected. A list of basic rules adopted in this modelling study in interpreting and sampling of the AIS ionogram data is given below.

(1) When possible, overhead ionogram data points should be used, e.g. those data points whose angles of arrival are less than 16 degrees from zenith (F. Sedgemore, private communication, 1994). This is generally good for the sampling of F-region traces, but a bit difficult for E-region data points where there is a problem caused by interference aliasing, which arises from the mutual coupling between individual antennas, a common problem for all direction finding radio systems. Usually, when the frequency is below 1.5 MHz, the angle of arrival parameter should not be used. Only use the parameter range of time of flight.

(2) Always make use of those data points with large echo amplitudes.

(3) When possible, use the second hop trace to help locate the true first hop trace.

(4) Neighbouring plots should be used to check and locate sporadic E, which should not be sampled when using POLAN to invert the real height profile of electron density.

(5) Checking and smoothing by eye is more important than holding strictly to measured ionogram data points, especially when there are missing data points, or wave events present in an ionogram. In other words, smoothing by eye is generally better than POLAN's interpolation work.

5.3.4 The ionosphere above Halley

The location of the Halley AIS dynasonde is near the Halley HF radar site, which is in the subauroral region, where the ionosphere can be affected by a number of ionospheric processes such as particle precipitation and ionospheric plasma convection. It is quite common for some type of ionospheric disturbance to be present in the Halley dynasonde data. Three examples, shown in figures 5.1, 5.2, and 5.3, illustrate the Halley AIS ionogram data for 8 December 1988 and demonstrate how to sample ionogram data with various small ionospheric disturbances present. Figure 5.1 shows the ionogram data at 05:00:00 UT. The top panel displays the whole ionogram data, both the O-mode and X-mode traces. The middle and bottom panels are the O- and X-mode data, respectively. The figure shows that both the O- and X- mode F-region traces are quite spread. The sampled data points are shown by the large dots in the middle and bottom panels. Figure 5.2 shows the ionogram data at 06:00:00 UT, with an E_s trace underneath the E trace. Similar to figure 5.1, the top panel of figure 5.2 is for the whole ionogram data. The middle and bottom panels are for the O- and X- mode data, respectively. The sampled data points are again plotted in large dots. It is shown in the middle panel of figure 5.2 that the E_s trace is not sampled, as is required when using POLAN. The Halley ionogram data for 07:45:08 UT are shown in figure 5.3, with a visible distortion on the F1 trace (evidence for gravity waves). The sampled data points in the middle panel are smoothed by eye and do not exactly follow the distorted F1 trace. The reason of smoothing the ionogram data by eye is to help POLAN to get the best fit of the sampled ionogram data points.

5.3.5 Sensitivity to POLAN starting point

Having sampled the Halley AIS dynasonde data, we can now compute the real height profiles of electron density using POLAN. It is noticed that the POLAN computed profiles of electron density are sometimes quite sensitive to the first few sampled data points of the ionogram E trace. An example of this sensitivity is illustrated in figure 5.4, which shows how important are the first few sampled data points of the E trace at 06:30:08 UT. The solid curve is the POLAN computed profile of electron density with

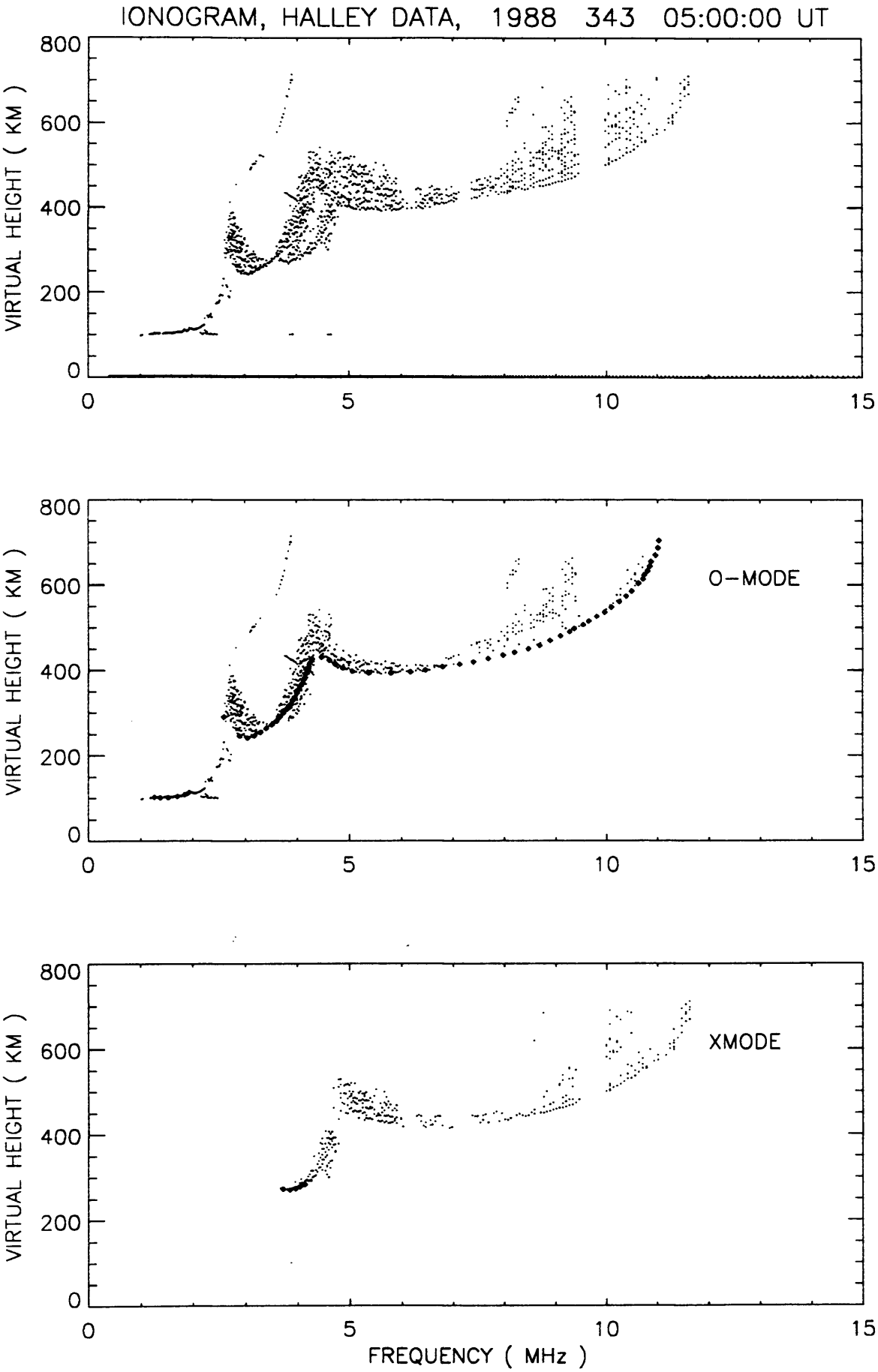

Figure 5.1 Halley AIS ionogram data at 05:00:00 UT, 8 December 1988

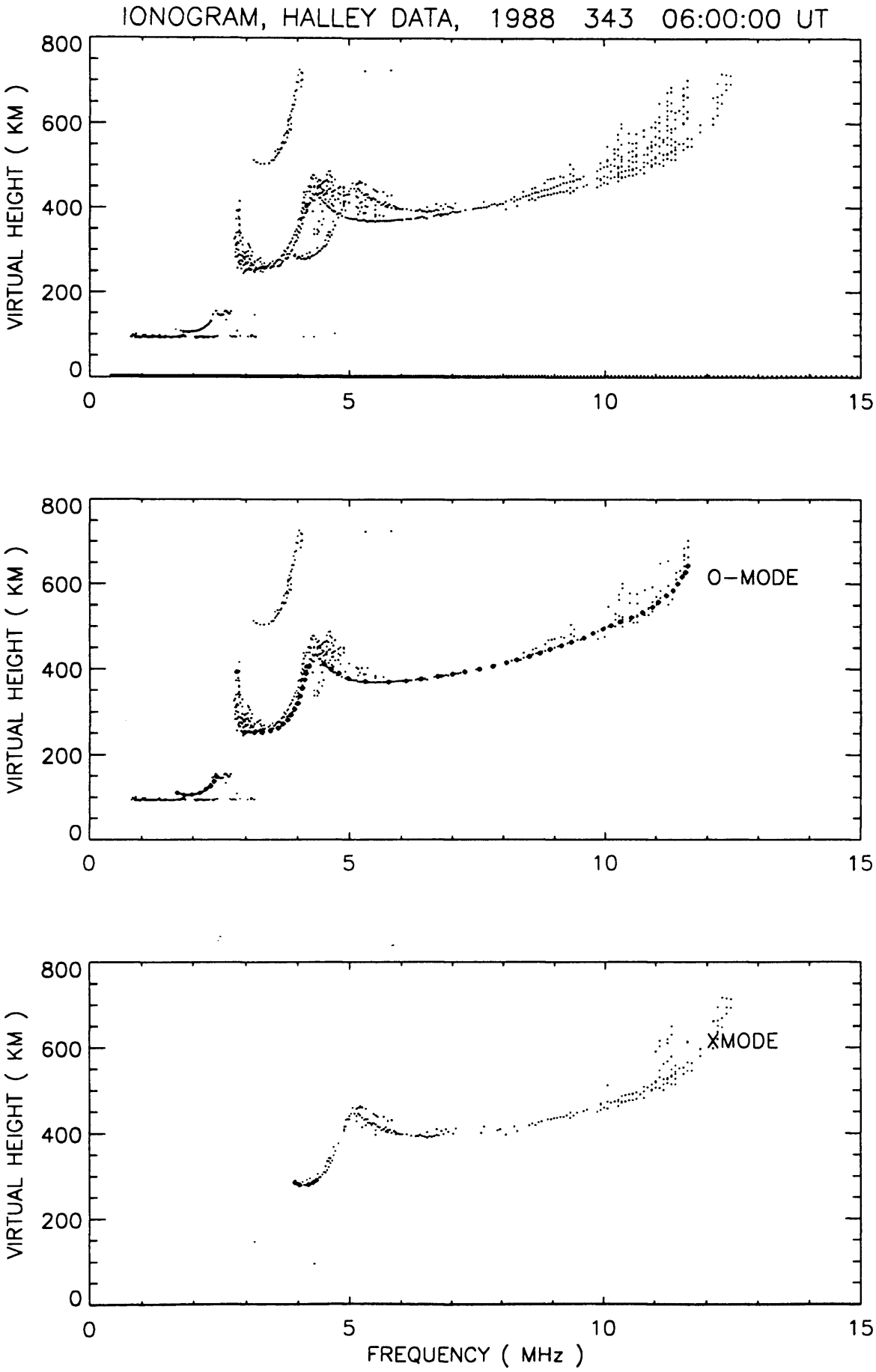

Figure 5.2 Halley AIS ionogram data at 06:00:00 UT, 8 December 1988

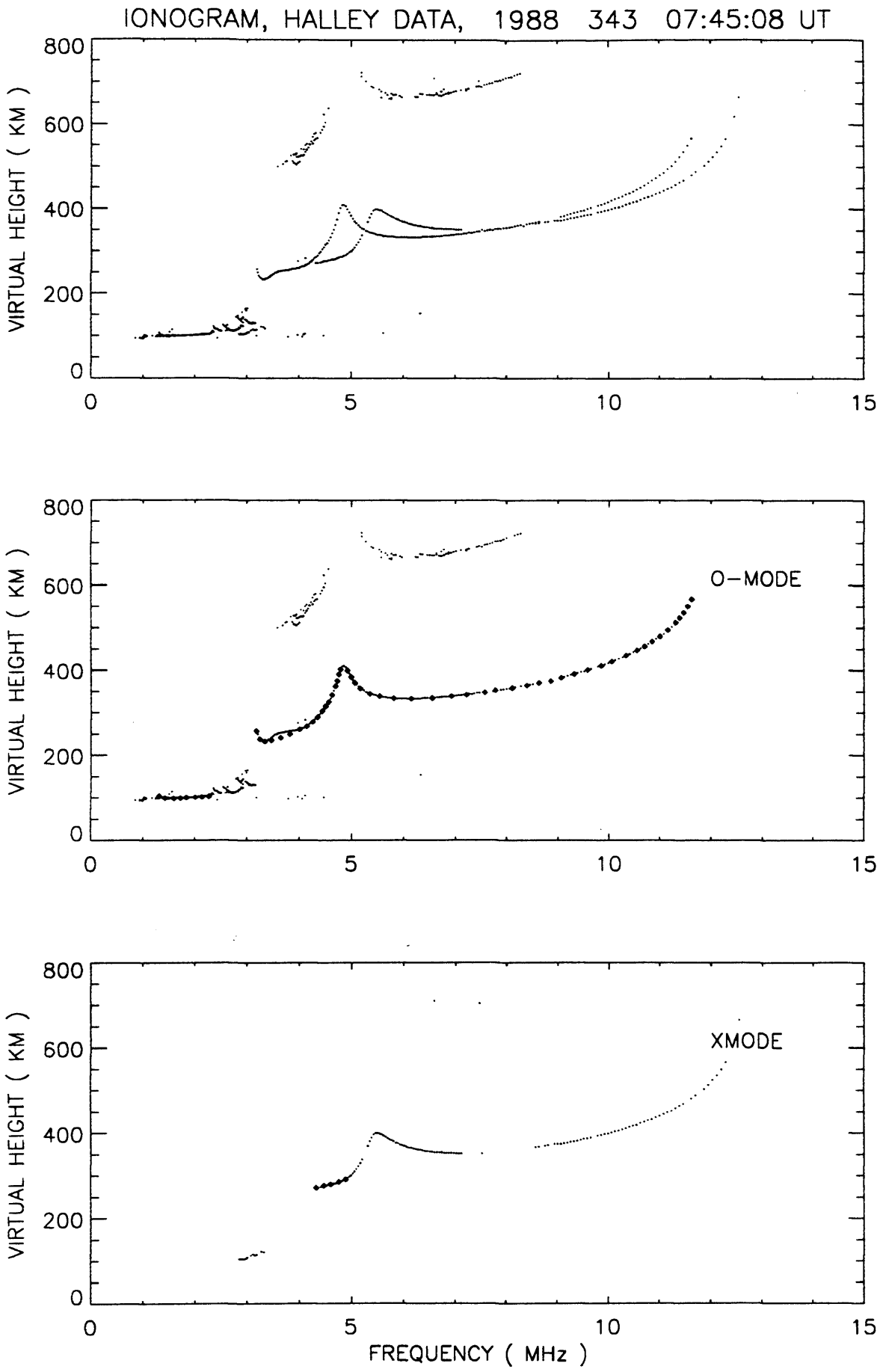

Figure 5.3 Halley AIS ionogram data at 07:45:08 UT, 8 December 1988

all sampled data points. The other three curves are POLAN computed profiles with the first one, three, and four sampled data points missed out. Figure 5.4 shows that the difference in both electron density and height could sometimes be significant with just the first one or two sampled (E-region trace) data points missed out. This sensitivity can have serious implications, especially when absorption causes the first few ionogram data points to be not observable or when the normal E trace is overlapped by sporadic E. In the latter case, the E_s trace should not be sampled when using POLAN to compute the real height profiles of electron density.

5.3.6 PIM correction of the POLAN starting point

The above sensitivity problem is caused by the way POLAN calculates its 'starting point'. For some practical reasons, ionogram data do not provide measurements below a certain minimum frequency, and hence there is an 'unobserved' section of the electron density profile below a certain height, the underlying ionisation. By default, POLAN uses the first three sampled (E-region trace) data points to extrapolate a starting point and makes use of both O-mode and X-mode measurements at low frequencies to estimate the unobserved underlying ionisation. Different sampled data points may result in different underlying ionisations, and therefore result in different profiles of electron density.

This difficulty can be resolved by specifying a reasonable starting point for the underlying ionisation. The user specified starting point is then used by POLAN to invert the real height profile of electron density from ionogram data. In the work described in this thesis, the Parameterised Ionospheric Model (PIM) is used to predict a reasonably good E-region starting point for various ionospheric conditions. Figure 5.5 gives the POLAN inverted vertical profiles of electron density using the same ionogram data as figure 5.4, but now using the PIM prediction of the POLAN starting point. This figure shows that the profiles of electron density with PIM corrections are more stable and consistent, especially at the E-region height. This proves to be a good way of getting the best possible POLAN computed profiles of electron density. Therefore, in

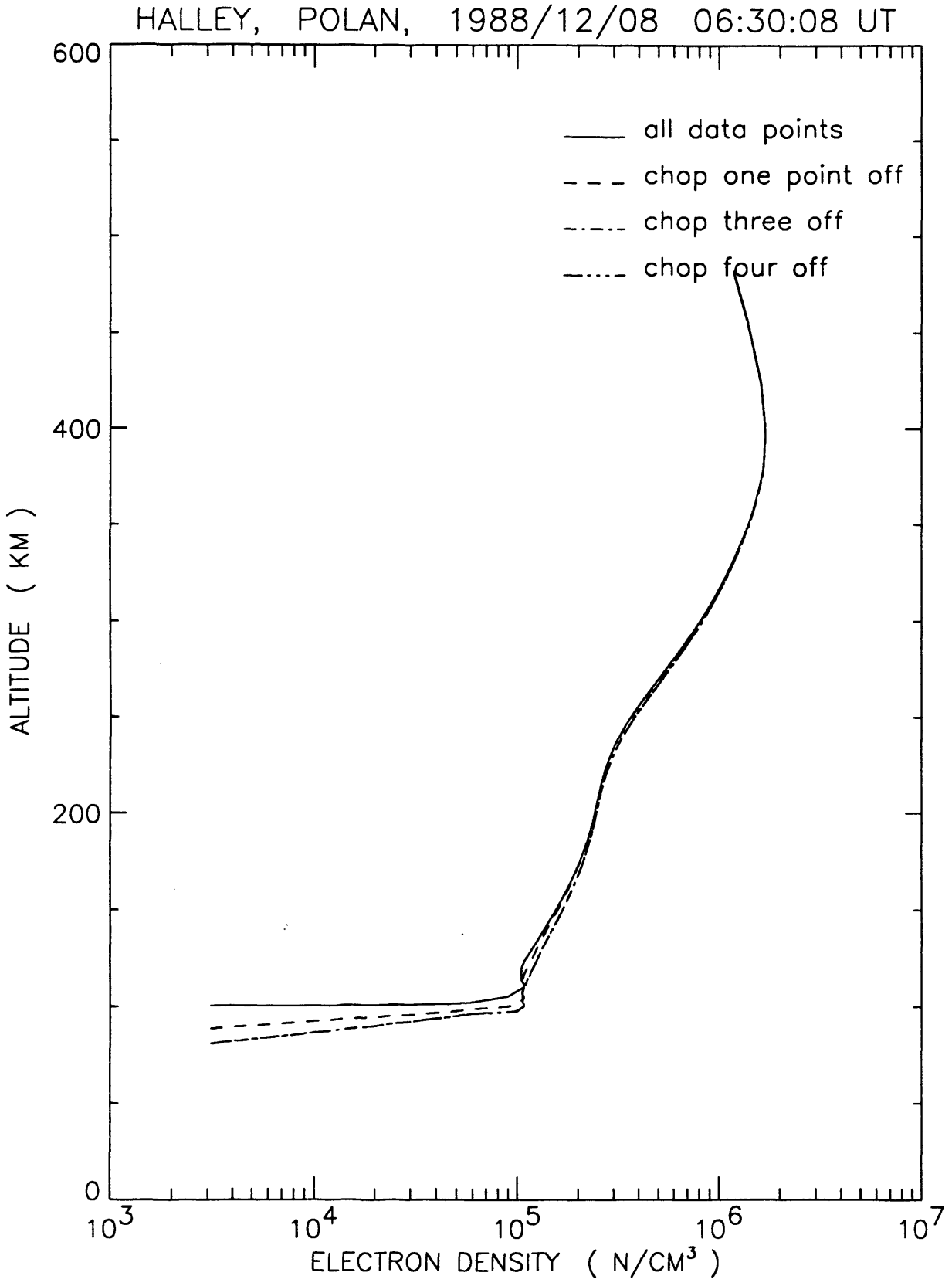

Figure 5.4 Sensitivity of POLAN inverted profiles of electron density to the first few sampled data points

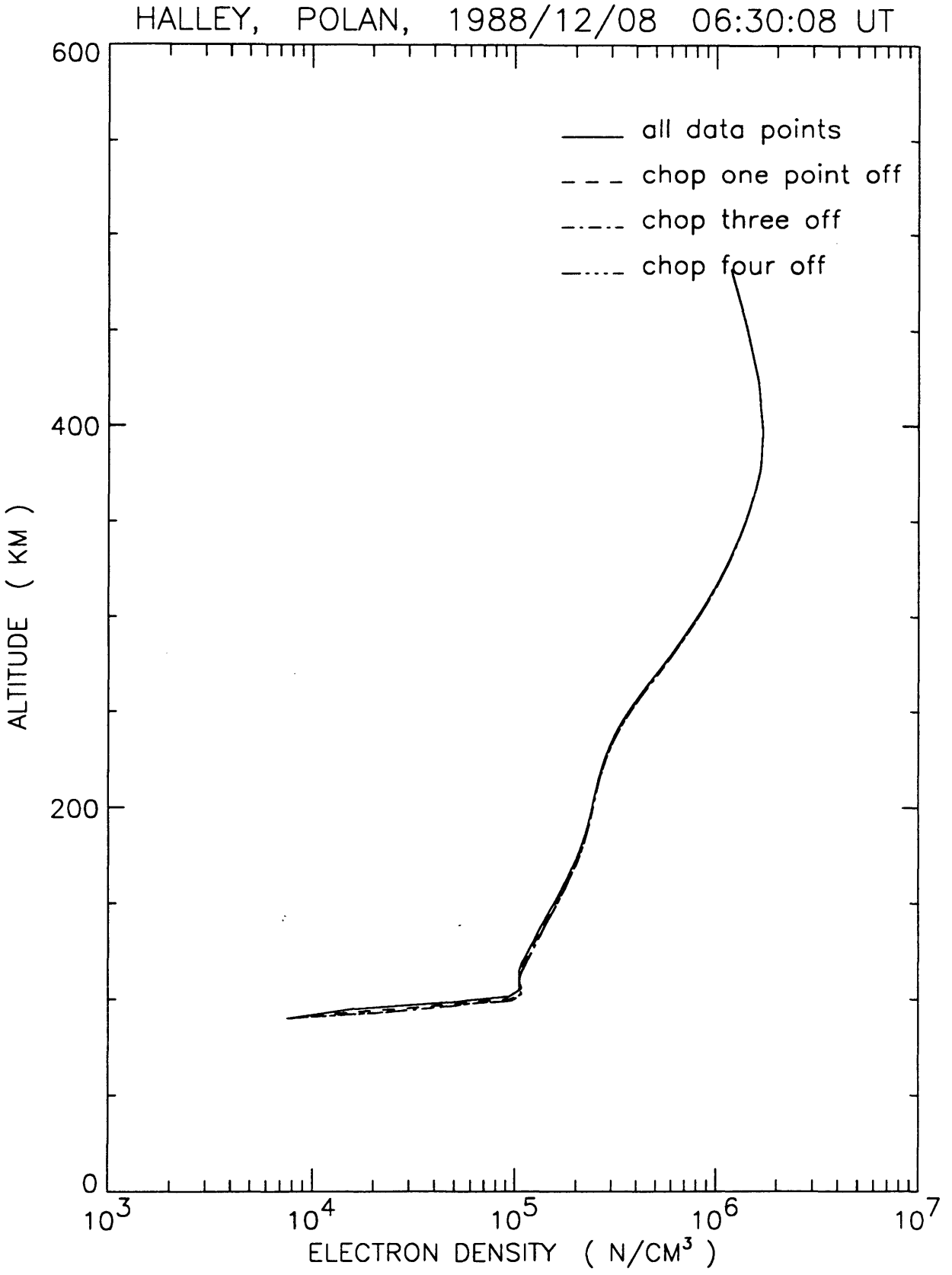

Figure 5.5 POLAN inverted profiles of electron density with PIM corrected starting point

this research, all of the POLAN profiles of electron density are computed with the PIM corrections of the POLAN starting point.

5.4 ELECTRON DENSITY PROFILE (2) -- CUTLASS FINLAND RADAR

For the Cooperative UK Twin Located Auroral Sounding System (CUTLASS) HF radar in Finland, the model inputs of realistic ionospheric conditions are provided by the EISCAT CP1 data measured at Tromso (Norway). The CP1 experiment measures the profiles of electron density along the geomagnetic field line, which is ~13° from vertical. Furthermore, the EISCAT radar at Tromso is in the CUTLASS radar field of view.

The CP1 profiles of electron density used in the modelling study to be discussed in chapter 7 consist of two parts, the alternating code data (below 142 km) and the long pulse data (above 142 km). The alternating code data have a very fine 3 km height resolution, whereas for the long pulse data the height resolution is 22 km. It is noticed that there is a non-trivial discrepancy in electron density between the two experiments. There is no good explanation available at the moment for the discrepancy between the two experiments. The possible effect of this discrepancy in electron density on the ray paths will be discussed in chapter 7.

Because in the subauroral region, the CP1 data measured at Tromso may sometimes display a reasonably large auroral E, which may have strong effect on the ray paths in regions of particle precipitation. This large auroral E makes the Gaussian extrapolation scheme of TABLEX essential to HF radar modelling (see chapter 4).

5.5 DIFFERENT MODES OF HF RADAR MODELLING

Both the Halley and the CUTLASS Finland HF radars have 16 beams numbered from beam 0 to beam 15 and operate in beam-scan mode. In this mode, the radar transmits and detects successively beam by beam from beam 0 to beam 15. For each beam, the radar measures and samples backscatter in terms of range-bins starting from a

predefined first range gate. In the modelling work, two different modes of radar modelling are performed, the B-mode and beam-scan mode. These are now discussed below.

5.5.1 B-mode ray tracing modelling

In the B-mode, all 16 radar beams are simulated into one big rectangular beam, whose overall radiation pattern is assumed to be flat. In modelling, the rays are traced stepping one degree per ray in both elevation and azimuth. The output results are (ionospheric) orthogonal ray points and ground ray points. Although ray tracing can not give dynamic parameters such as Doppler velocity and spectral width, which are used by radar to separate ionospheric echoes from ground backscatter, ray tracing modelling can provide another way of doing this. That is, ray tracing modelling can distinguish between those ray points for which orthogonal conditions are satisfied and those ray points which reach the ground.

The advantage of this modelling mode lies in its statistical meaning of the computation of orthogonal ray points and ground ray points. Statistically, the more orthogonal ray points (or ground ray points) that are computed in a range-cell, the better the chance for the radar to receive ionospheric (or ground) backscatter from the range-cell. Detailed B-mode modelling and comparison with radar observations will be given and discussed in chapter 6.

5.5.2 Beam-scan mode of ray tracing modelling

As described above, both the Halley and the CUTLASS HF radars operate in the beam-scan mode. This suggests that the best way of simulating the radar detection of ionospheric irregularities might be to trace all 16 radar beams individually one by one through the same ionosphere as the radar does in real operation. This way of simulation is referred to as the beam-scan mode of ray tracing modelling.

In this mode, each radar beam is treated individually and equally. That is, for each of the 16 beams, the rays are traced stepping every one degree per ray in both elevation and azimuth, the same as in the B-mode modelling. The output results are again (ionospheric) orthogonal ray points and ground ray points. The difference between the B-mode and the beam-scan mode is due to their different ways of backscatter sampling. In the B-mode, it is assumed that, in a range-cell, the more orthogonal ray points (or ground ray points) that are computed, the better the chance for the radar to receive ionospheric (or ground) backscatter from the range-cell. In the beam-scan mode, however, the sampling of each of the ray tracing beams is exactly the same as in the radar operation, starting from the first range gate by range resolution. Within a range-cell, if one or more (E-region orthogonal, F-region orthogonal, or ground) ray points are sampled, then we say the radar has received (E-region, F-region, or ground) backscatter from this range-cell. Although this way of sampling of ray tracing results suppresses the statistical meaning of the computation of orthogonal ray points and ground ray points, it makes the range comparison easier between ray tracing results and radar scan data. The beam-scan mode is able to separate radar backscatter into E- and F-region scatter, whereas it is difficult for an HF radar to do so. Detailed modelling in the beam-scan mode and comparison with radar observations will be discussed in chapters 6 and 7.

5.6 RADAR GROUND BACKSCATTER

The existence of radar ground backscatter is obvious from radar observations. Much work, both experimental and modelling, has already been done studying the HF radar ground backscatter. For example, the radio echo sounding of ice sheets has been studied by Robin *et. al.* (1969) and West and Dermarest (1987); the analyses of backscatter ionograms have been studied by Maliphant (1968) and Croft (1972); the seascatter problem has been discussed by Jones *et al.* (1986); the modelling study of HF radar ground backscatter has been addressed by Villain *et al.* (1984) using a realistic high-latitude ionosphere derived from measurements made with an incoherent scatter radar; and Samson *et al.* (1990) have studied HF radar propagation through an ionosphere

modulated by gravity waves. However, there is still no satisfactory theory established for the radar ground backscatter.

In practice, the radar criteria in use are mainly based on the radar measured parameters of Doppler velocity and spectral width. For both the Halley and the CUTLASS HF radars, the ground backscatter is defined as radar scatter whose velocity and spectral width are both less than 50 m/s, while in ray tracing modelling the ray ground backscatter is defined as those ray points which have been reflected by the ionosphere and reached the ground.

5.7 SUMMARY

A detailed discussion is given of the preparation of model inputs of realistic ionospheric conditions. Different modes of HF radar modelling are discussed. The definitions of radar ground backscatter and ray tracing ground backscatter are also given. All discussions are based on two HF coherent backscatter radar systems, the Halley HF radar in Antarctica and the CUTLASS HF radar in Finland. The contents of this chapter will be used in detailed discussions of HF radar modelling for the two radars, given in chapters 6 and 7.

CHAPTER 6

THE HALLEY HF RADAR AND COMPUTER MODELLING

6.1 INTRODUCTION

It is well known that HF coherent backscatter radar is a powerful tool for sounding the F-region small-scale irregularities of the high-latitude ionosphere with the help of the ionospheric bending effect on the radio waves (Greenwald *et al*, 1995). Because of this ionospheric refraction, the exact path of the radar signal through the ionosphere is then unknown. In practice, it is important to determine how accurately the radar echo sources can be located given the echo parameters, such as group path, elevation angle and azimuth angle. This problem has been addressed by Villain *et al.* (1984), who modelled HF ray propagation in a realistic high-latitude ionosphere derived from measurements made with an incoherent scatter radar. Samson *et al.* (1990) have discussed ray paths of HF radar propagation through an ionosphere modulated by gravity waves.

HF radar observations also consist of direct backscatter from the ground. A further uncertainty arises due to the difficulty in separating true ground backscatter from ionospheric scatter which fulfils the radar criteria. A study of the early data from the Goose Bay radar has shown that the characteristics of ground backscatter are dependent on the power, i.e. weak ground scatter tends to have shorter decorrelation times (Baker *et al.,* 1987). Bristow *et al.* (1995) have briefly discussed ray paths for ground

backscatter from a horizontally uniform ionosphere and an ionosphere which is perturbed by a sinusoidal perturbation.

Therefore, studying the separation of radar ionospheric echoes from its ground backscatter is of practical importance in both radar operation and data interpretation. This chapter discusses ray tracing modelling of HF coherent detection of small-scale irregularities of the high-latitude ionosphere and its comparison to radar observations made by the Halley HF radar in Antarctica. Emphasis is given to the separation of radar ionospheric backscatter from ground backscatter.

6.2 THE HALLEY HF RADAR

The Halley HF radar in Antarctica (-75.52N, -26.63E) is a ground-based HF coherent backscatter radar system for the study of small-scale dynamics of the high-latitude ionosphere. The radar forms part of the Polar Anglo-American Conjugate Experiment (PACE). Two radars, one at Halley and the other at Goose Bay, Labrador, view geomagnetically conjugate sectors of the high-latitude ionosphere. A general discussion of the experiment has been given by Baker *et al.* (1989a, b). The Halley radar is similar to that at Goose Bay which was deployed in 1983 by the Johns Hopkins University, Applied Physics Laboratory (APL) and has been described by Greenwald *et al.* (1985).

6.2.1 Radar basic operational parameters

Table 6.1 gives a list of radar basic operational parameters (courtesy of M. Pinnock, private communication 1994).

Table 6.1 the radar basic operational parameters

location:	Antarctica (-75.52N, -26.63E)
antenna mast:	6 meters above the ice, or 150 meters above the ground
total number of beams:	16 beams, numbered from 0 to 15
beam width:	2.5^{0} at 20 MHz and 6^{0} at 8 MHz

angular separation:	3.24^{o} (between two adjacent beams)
central azimuth:	165° from north
total azimuth sweep:	16 × 3.24 (139.08 - 190.92)
working frequency:	12 - 16 MHz
peak elevation angle:	~ 38°
total elevation angle:	36° ?
integration time:	6 seconds per beam, 96 seconds per scan
total range bins:	75
first range:	135 km
range resolutions:	Halley radar can use 15, 30, 45 km

Note that the radar frequency and range resolution used in the work described here are 12.1 MHz and 45 km, respectively.

6.2.2 Radar ground backscatter

For the Halley HF radar, ground backscatter is defined as radar backscatter whose velocity and spectral width are both less than 50 m/s. The existence of radar ground backscatter at Halley is perhaps unexpected, as most of Antarctica is covered with very thick ice/snow. However, from the radar observations, ground backscatter is seen by the radar. The thickness of ice/snow on the central plateau is typically of around 2,000 to 3,500 metres (Leonard, 1991). Theoretically, for this sort of thick ice/snow, one would expect a severe attenuation of radar signals rather than big ground backscatter. Although much work has already been done studying the radio echo sounding of ice sheets (Robin *et al.* 1969; West and Demarest, 1987), there is still no satisfactory theory established for radar ground backscatter. It will be shown in this chapter that part of the radar ground backscatter might be produced by irregularities from somewhere within the ice and part could be misinterpreted ionospheric backscatter.

6.3 RAY TRACING COMPUTER MODELLING

Using an HF coherent backscatter radar system to study small-scale dynamics of the high-latitude ionosphere, it is very important to locate the radar echo source and to separate the radar ionospheric echoes from ground backscatter. In practice, radars use the measured range (group path) information to locate the radar echo source, and use the measured Doppler velocity and spectral width to separate radar ionospheric echoes from ground scatter.

Here, we use ray tracing technique to investigate this problem under realistic ionospheric conditions. Ionospheric backscatter is computed when the ray orthogonal condition is satisfied between the ray wave vectors and the earth's magnetic field lines, whereas ground backscatter is computed when the rays are reached the ground after being reflected by the ionosphere (see chapters 4 and 5). Using modelling prediction of HF ionospheric and ground backscatter, it helps to study the physics of wave-wave scattering as well as the radar criteria used in separating the radar ionospheric backscatter from ground backscatter.

6.4 B-MODE RAYING TRACING MODELLING

In this case study, the B-mode ray tracing modelling simulates all 16 beams of the Halley HF radar as one big rectangular beam, whose central azimuth angle is 165° from the north (139.08° - 190.92°), and the peak elevation angle is 38°. The overall radiation pattern of this one-big-rectangular beam is assumed to be flat.

6.4.1 B-mode modelling and comparison to radar observations

Figures 6.1 and 6.2 illustrate the ray paths predicted for the Halley HF radar at 06:30 UT on 8 December 1988. In figure 6.1 a vertical projection of the ray paths is given, whilst in figure 6.2 the projection of the ray paths is onto the ground. In both plots, small vertical bars are used to indicate where the ray orthogonalities are computed. For the purpose of illustration, in figure 6.1, the rays are traced through at a fixed azimuth

SPECIAL NOTICE

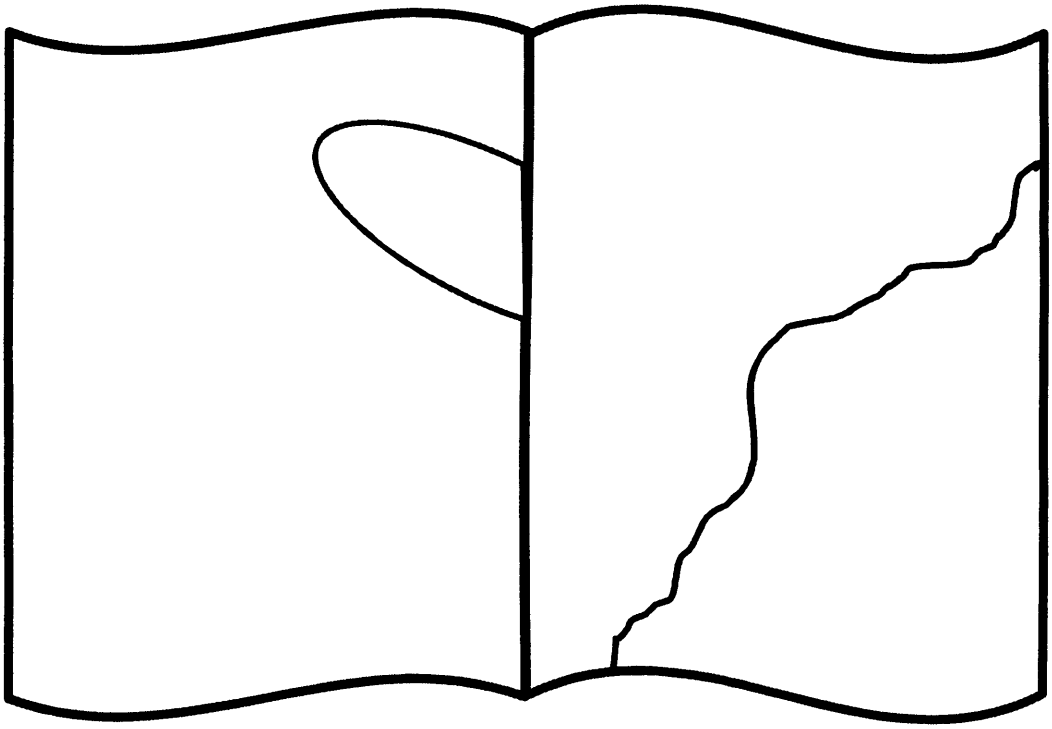

DAMAGED TEXT - INCOMPLETE IMAGE

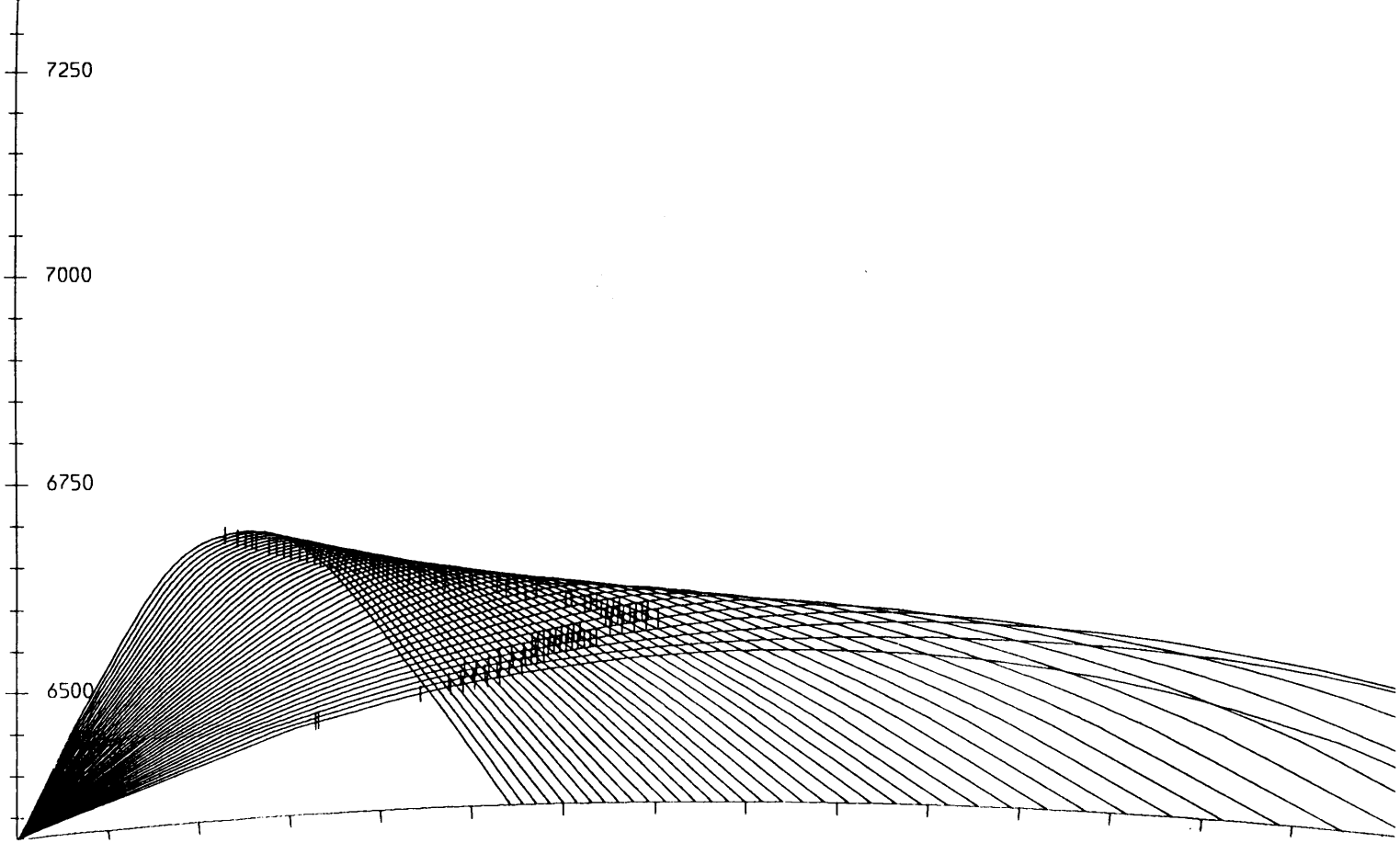

POLAN DATA, HALLEY BAY 08/12/88 0630 UT

BAS

F= 12.1000, INI AZ= 165.0000, FIN AZ= 165.0000, ORDINARY

INI EL= 15.0000, FIN EL= 56.0000, 100.0000 KM BETWEEN TICKMARKS

Figure 6.1

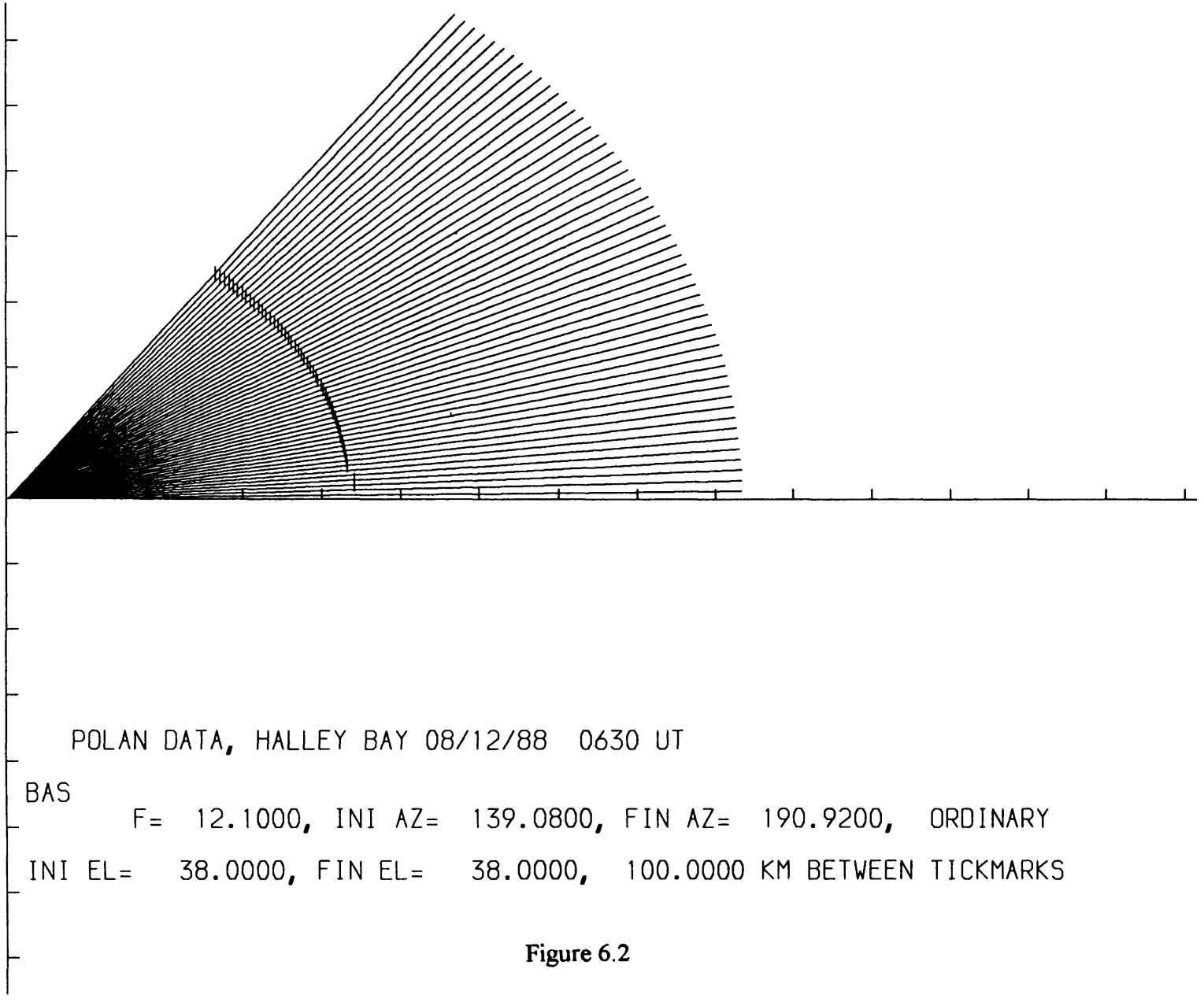
POLAN DATA, HALLEY BAY 08/12/88 0630 UT
BAS
F= 12.1000, INI AZ= 139.0800, FIN AZ= 190.9200, ORDINARY
INI EL= 38.0000, FIN EL= 38.0000, 100.0000 KM BETWEEN TICKMARKS

Figure 6.2

angle of 165 degrees from the north and in figure 6.2 at a fixed elevation angle of 38 degrees.

A comparison of the B-mode ray tracing modelling with the radar observations is given in figure 6.3. The top three panels give one radar scan data for 06:30:42 UT on 8 December 1988 at 12.1 MHz. The bottom three panels are the B-mode modelling results. All plots are arranged in the same geographic coordinate system. For the top three panels, the left panel is colour-scaled in radar backscatter power dB, the central panel colour-scaled in regions with the ionospheric backscatter in green and ground backscatter in red, and the right panel colour-scaled in group path. The bottom left panel displays the altitude of ray orthogonal points and ground points in km. The bottom central panel identifies the ray orthogonal points from the ray ground points, with the F-region ray points in green, the E-region ray points in blue and the ground ray points in red. The bottom right panel is colour-scaled in group path. From the two right-hand panels of group path, it is seen that the radar received backscatter and the B-mode ray tracing results agree quite well in group path. This implies that the physics of the modelling is generally correct. The comparison of the two central panels is not good. This is because two different methods are used to separate the radar ionospheric echoes from ground backscatter. The radar uses the measured Doppler velocity and spectral width, whereas ray tracing modelling uses the heights of orthogonal ray points. No conclusion can be drawn without further analysis and comparison. And these will be discussed in the next section.

6.4.2 Range-bin statistical analysis

To investigate the above comparison in more detail, further analysis is necessary. One approach is to investigate the range bins of radar scatter. This is termed the range-bin analysis. This range-bin analysis is based on a suggestion that the range (group path) is one of the four radar measured parameters and should be as important as the other three parameters and be able to provide useful information on backscatter identification. The other three radar measured parameters are the Doppler velocity, spectral width, and backscatter power.

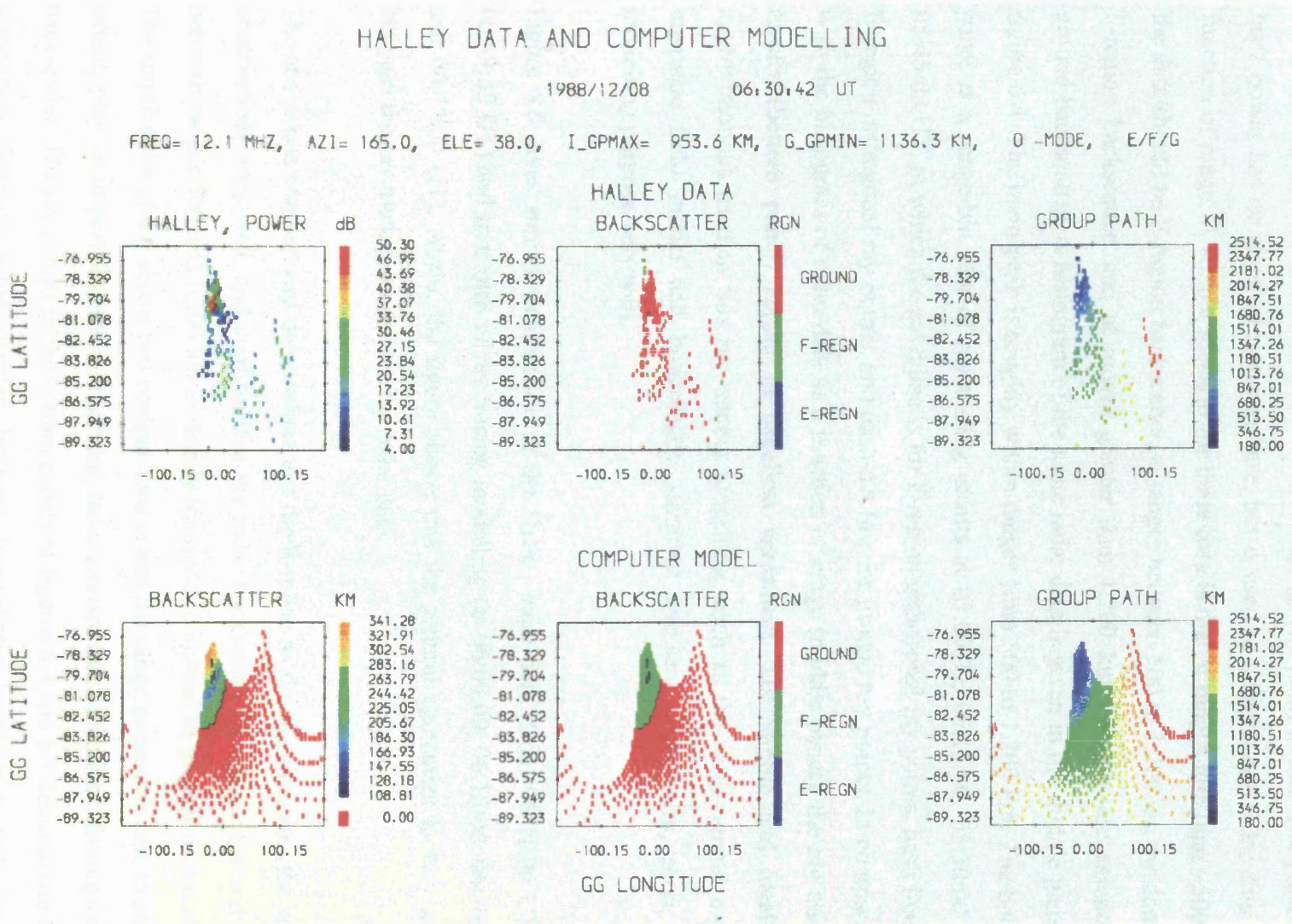

Figure 6.3 Comparison between Halley radar one scan data and the B-mode ray tracing results

The radar data in the top panel of figure 6.4 are backscatter from all 16 beams from 05:04:00 to 05:58:55 UT on 8 December 1988. The ordinate of the top panel is the measured lag0_power and the abscissa is the range (group path) in km. The parameter lag0_power has no physical meaning here, but is used to demonstrate radar data as a function of range. A simple scenario for these data is that at ranges less than ~500 km the data should be E-region backscatter, at ranges between 500 to 1,200 km the data are F-region backscatter, and at ranges greater than 1,200 km the data are essentially ground backscatter. A histogram of the same radar data is given in the middle panel of figure 6.4. The main peak is roughly within ranges from 500 to 1,200 km. The bottom panel is a range-bin plot of ray tracing results at 05:00:00, 05:15:00, 05:30:00 and 05:45:00 UT, in which the solid line is for F-region orthogonal ray points, dash line for E-region orthogonal ray points, and dash-dot line for ground ray points. In comparison with the histogram of radar data as a function of range (middle panel), the ray tracing results (bottom panel) appear in excellent agreement. The simple and idealised approximations used in this ray tracing modelling, such as the earth-centred dipole magnetic field model and horizontally stratified overhead ionosphere, serve the modelling purpose very well.

Figure 6.5 gives another comparison of the Halley radar data (from 06:01:00 UT to 06:59:55 UT) and four runs of ray tracing modelling (at 06:00:00, 06:15:00, 06:30:00, and 06:45:00 UT). Again, the figure shows that the general agreement is very good between the ray tracing results and the radar data.

The above two comparisons demonstrate that the B-mode modelling simulates the radar observations very well, and confirm that the radar backscatter in figures 6.4 and 6.5 between ranges 500 and 1,100 km is largely ionospheric instead of ground backscatter. The implication of the above two comparisons is that the range parameter can, to some extent, play an important part in separating radar ionospheric backscatter from ground backscatter. The ray results in the bottom panels of figures 6.4 and 6.5 demonstrate that sometimes there is some overlap between ionospheric backscatter and ground backscatter (figure 6.5) and sometimes no overlap at all (figure 6.4).

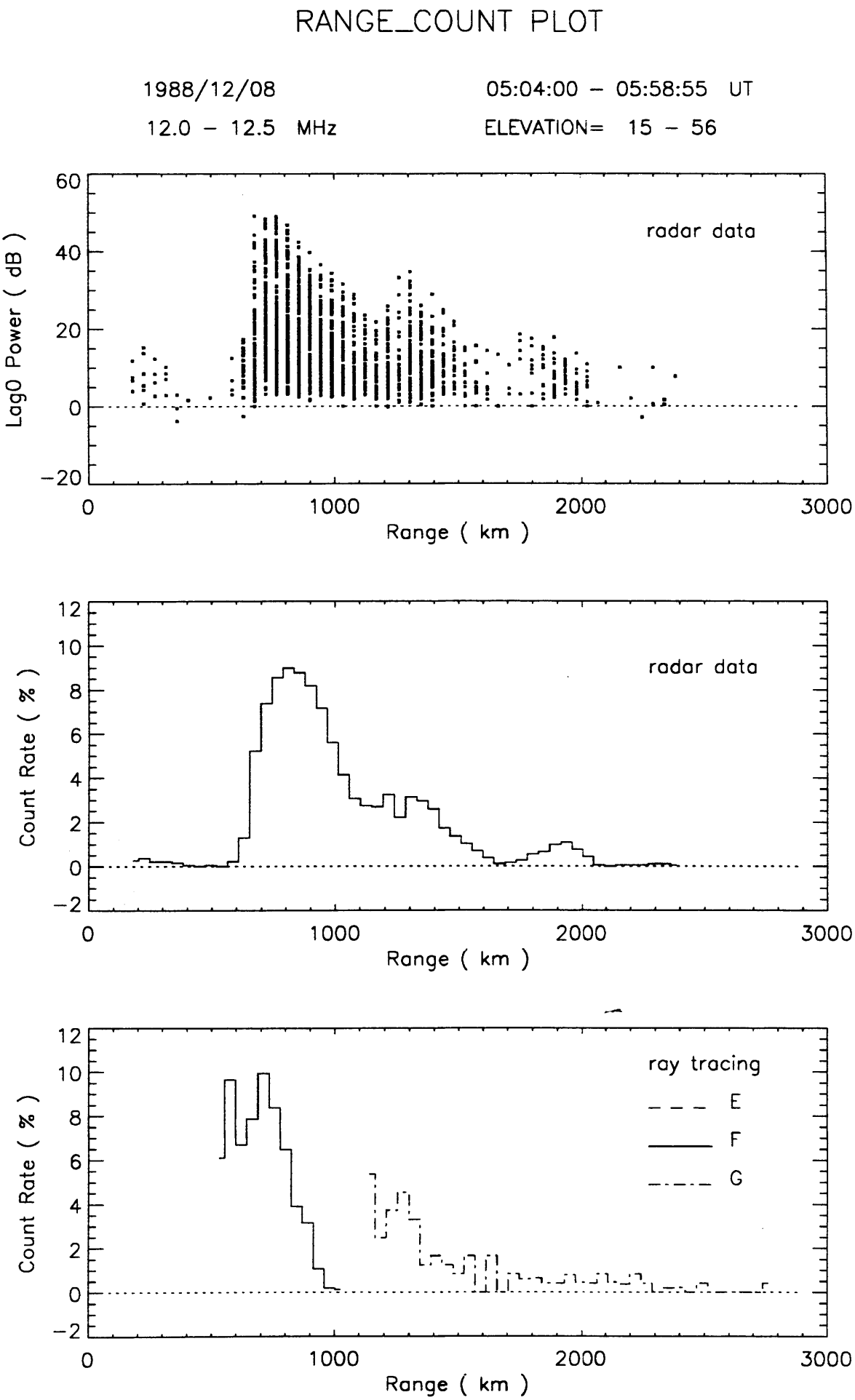

Figure 6.4 The B-mode ray tracing results and the range-bin statistical analysis

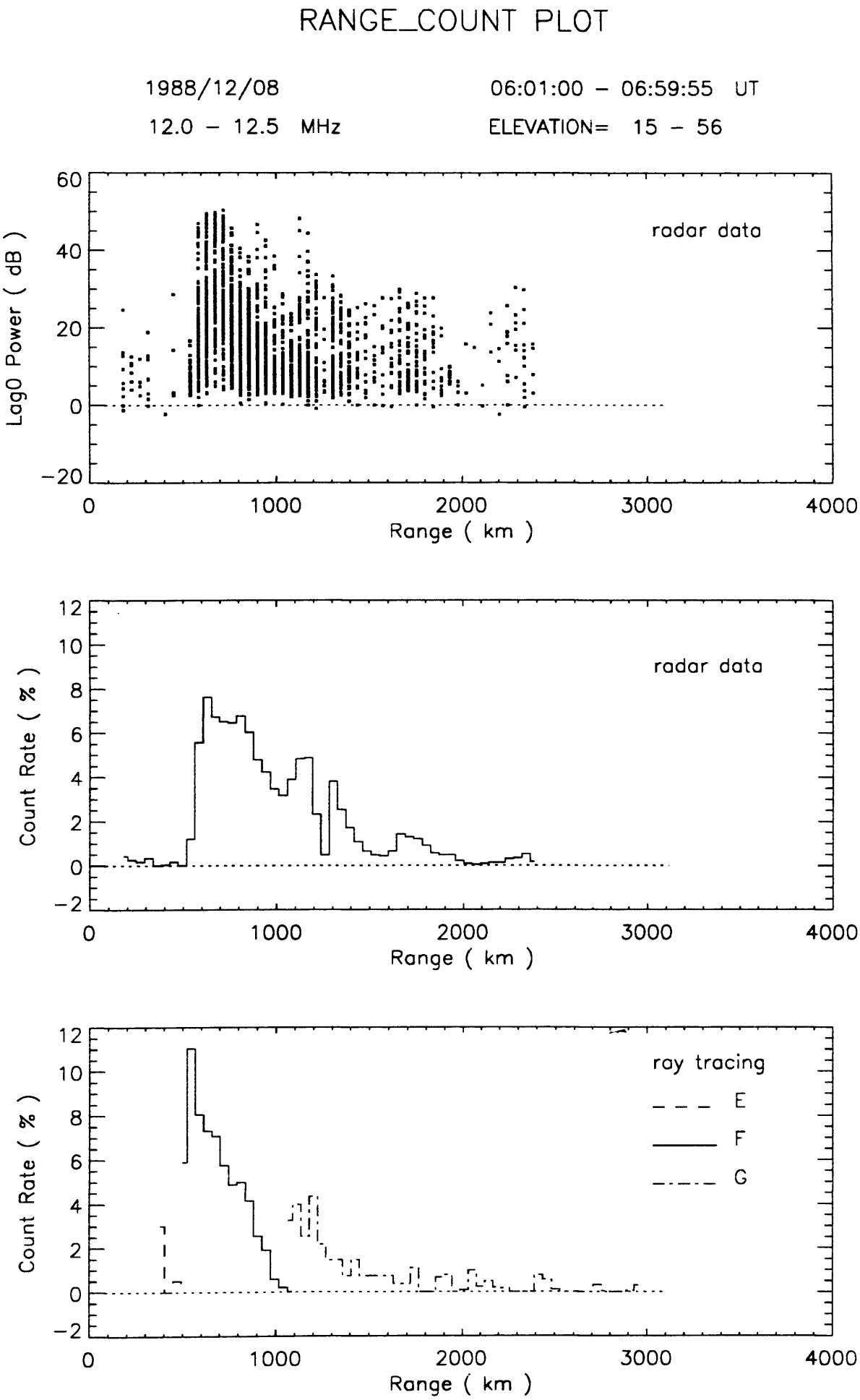

Figure 6.5 The B-mode ray tracing results and the range-bin statistical analysis

It is also seen in the above two comparisons that the agreement between the E-region radar observations and ray tracing results is not so good. This problem might be caused by a number of factors. First of all, the ray tracing may be affected by the POLAN computed E-region profiles of electron density, due to fewer data points in the E-region trace of ionogram data. Secondly, the assumptions of the lowest elevation angle of the radar beams and of the earth-centred dipole magnetic field model may cause the E-region ray tracing results to be less reliable. The F-region sharp overshoot in the bottom panel of figure 6.5 may result from using only four runs of ray tracing. More runs may improve the comparison, but this is subject to the availability of ionogram data.

6.5 BEAM-SCAN MODE OF RAY TRACING MODELLING

Because of the beam-scan mode operation of the Halley HF radar, intuitively, it may be more appropriate to simulate the radar 16 beams individually one by one through the same ionosphere as the radar does in real operation. This is the beam-scan mode of ray tracing modelling (see chapter 5).

6.5.1 Ray tracing/radar beam parameters

A list of azimuthal spread of all sixteen beams from beam 0 to beam 15 of the Halley HF radar in Antarctica is given in table 6.2 (Mike Pinnock, private communication 1994).

Table 6.2 Beam parameters of the Halley HF radar, Antarctica

Beam No	Beam Central Position	Beam Spread
0	189.3	(187.3 - 191.3)
1	186.06	(184.1 - 188.1)
2	182.82	(180.8 - 184.8)
3	179.58	(177.6 - 181.6)
4	176.34	(174.3 - 178.3)
5	173.1	(171.1 - 175.1)

6	169.86	(167.9 - 171.9)
7	166.62	(164.6 - 168.6)
The central azimuth: 165 degrees from the north		
8	163.38	(161.4 - 165.4)
9	160.14	(158.1 - 162.1)
10	156.9	(154.9 - 158.9)
11	153.66	(151.7 - 155.7)
12	150.42	(148.4 - 152.4)
13	147.18	(145.2 - 149.2)
14	143.94	(141.9 - 145.9)
15	140.7	(138.7 - 142.7)

For the Halley HF radar, one scan consists of 16 beams which are numbered from beam 0 to beam 15 in counter-clockwise direction (SuperDARN convention of numbering radar beams for radars in the southern hemisphere). The beam-width is 6 degrees at 8 MHz and 2.5 degrees at 20 MHz (Leonard, 1991). Here, we take 4 degrees for 12 MHz.

6.5.2 Beam-scan mode modelling and radar observations

Examples of four scans of the Halley HF radar at 06:01:55, 06:16:19, 06:30:42 and 06:45:07 UT are given in figure 6.6 in backscatter power and figure 6.7 in velocity/region. In figure 6.7, according to the radar criteria most of the backscatter is classified as ground backscatter. For comparison, the ray tracing results in figure 6.8 are also arranged in the same way as the radar scan plots. In figure 6.8, it is seen that the close range scatter is ionospheric and the long range patch is ground backscatter. In the first three ray tracing plots of figure 6.8 (06:00:00, 06:15:00, and 06:30:00 UT), no overlap is seen between the ionospheric backscatter and ground backscatter. Only in the last ray tracing plot at 06:45:00 UT, there is a little overlap between the ionospheric and ground backscatter.

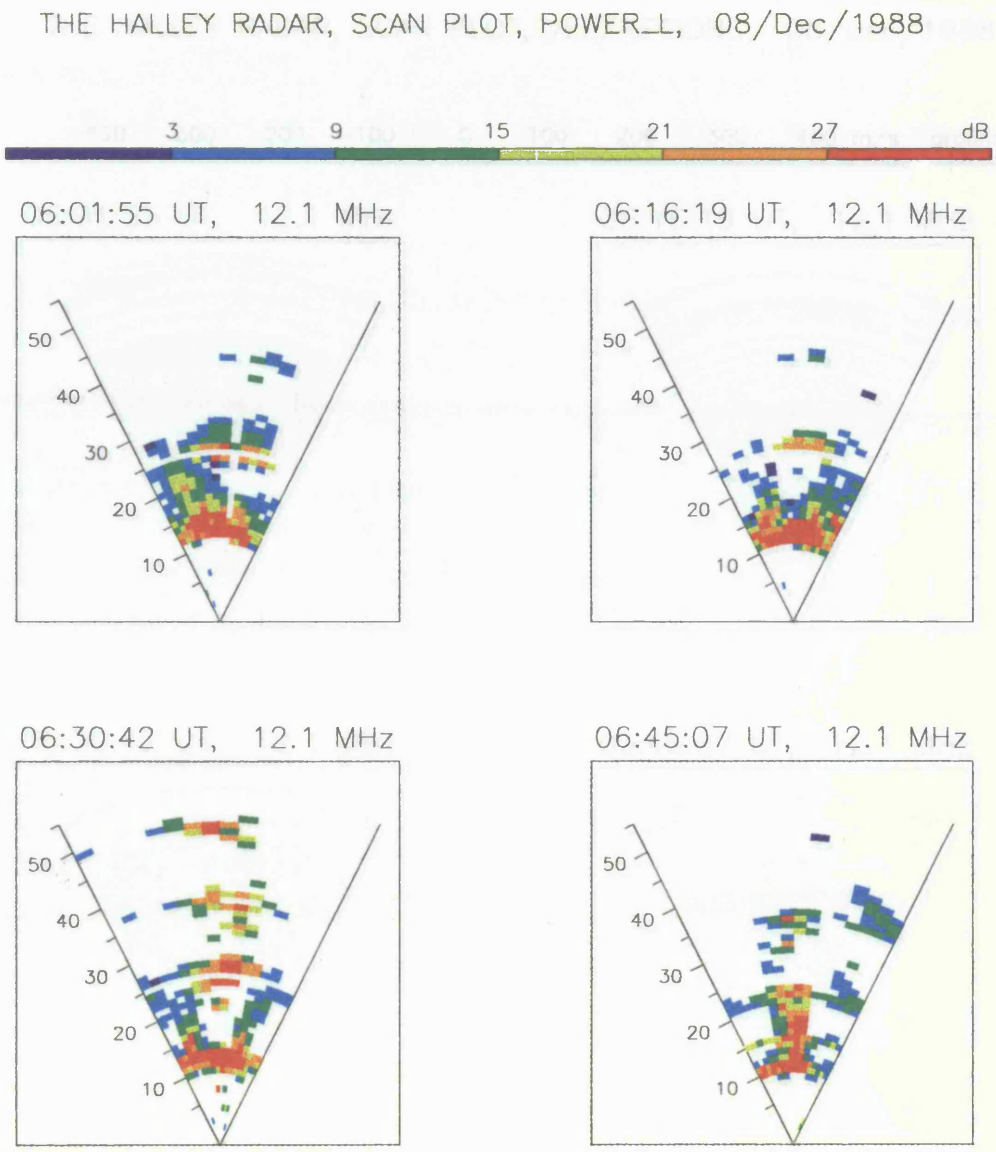

Figure 6.6 The Halley radar scan plots in backscatter power

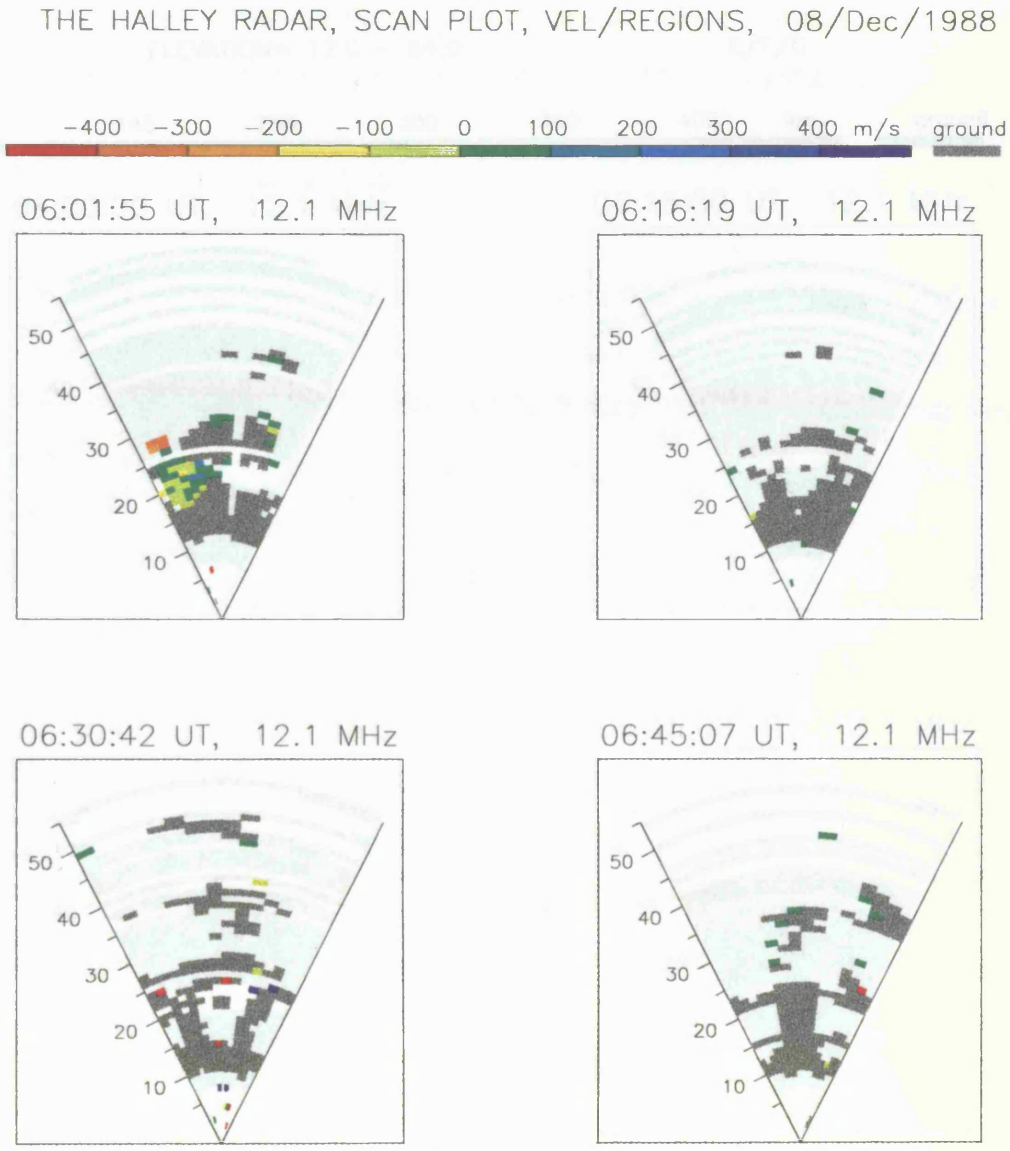

Figure 6.7 The Halley radar scan plots in velocity/region

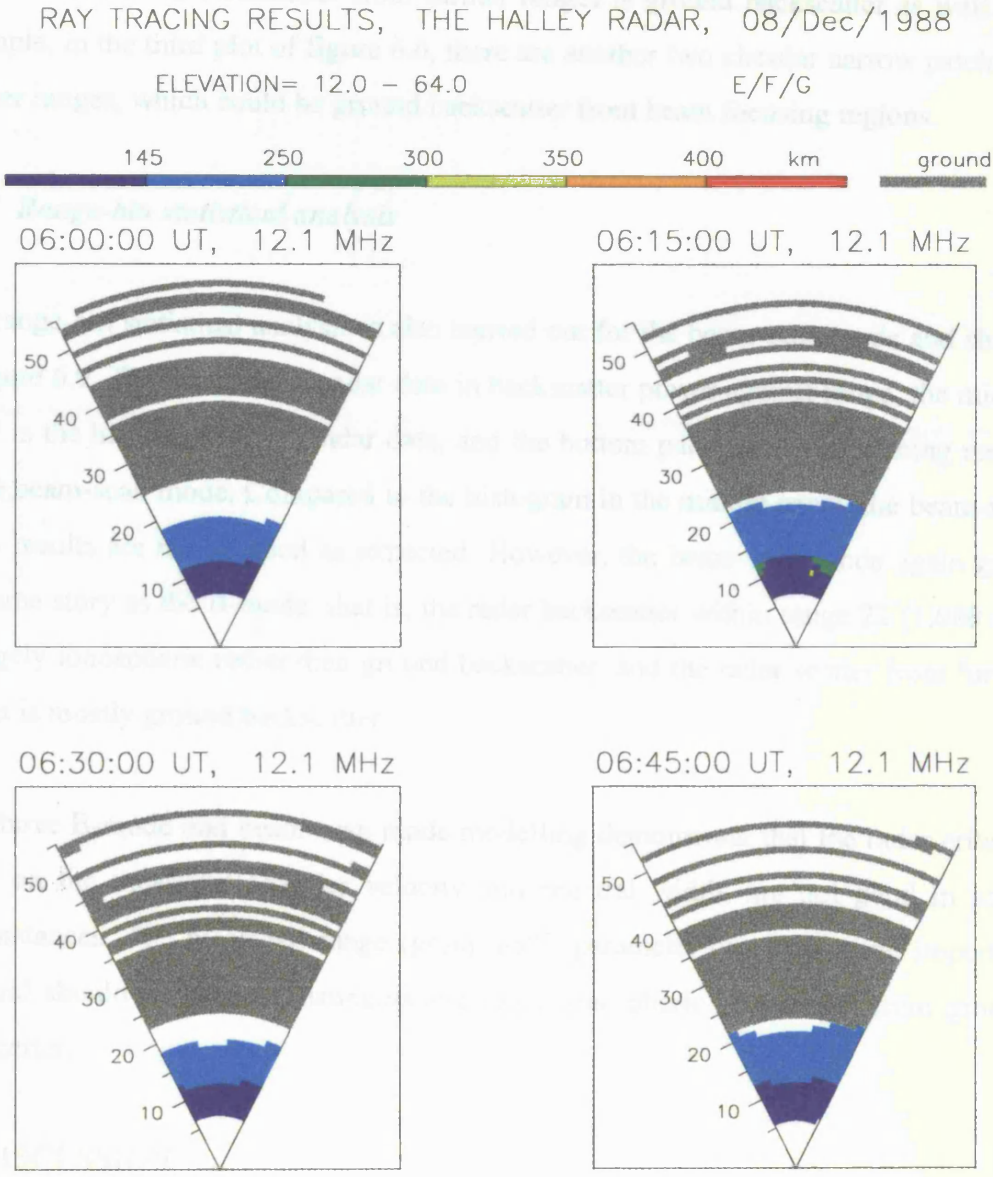

Figure 6.8 Ray tracing results in the beam-scan mode

Compared to the ray tracing results in figure 6.8, it appears that, in figure 6.6, the main red patches of shorter ranges (within ranges 10 - 20) are ionospheric backscatter. Those red circular narrow steady patches at further ranges (at range 25 for the first two plots at 06:01:55 and 06:16:19 UT, at range 23 - 24 for the third plot at 06:30:42 UT, and at range 21 - 22 for the fourth plot at 06:45:07 UT) are ground backscatter from skip distance. The radar backscatter from further ranges is ground backscatter as well. For example, in the third plot of figure 6.6, there are another two circular narrow patches at further ranges, which could be ground backscatter from beam focusing regions.

6.5.3 Range-bin statistical analysis

The range-bin statistical analysis is also carried out for the beam-scan mode and shown in figure 6.9. The top panel is radar data in backscatter power against range, the middle panel is the histogram of the radar data, and the bottom panel is the ray tracing results in the beam-scan mode. Compared to the histogram in the middle panel, the beam-scan mode results are not as good as expected. However, the beam-scan mode again gives the same story as the B-mode, that is, the radar backscatter within range 22 (1,080 km) is largely ionospheric rather than ground backscatter, and the radar scatter from further ranges is mostly ground backscatter.

The above B-mode and beam-scan mode modelling demonstrate that the radar criteria, based on the measured Doppler velocity and spectral width, are not good in some circumstances. The measured range (group path) parameter can play some important part and should be used in distinguishing radar ionospheric backscatter from ground backscatter.

6.6 DISCUSSION

Having discussed the B-mode and beam-scan mode modelling of the Halley HF radar in Antarctica, a general summary of the ionospheric conditions above the radar site on 8 December 1988 is now given below. Some of the problems encountered in the modelling are also discussed.

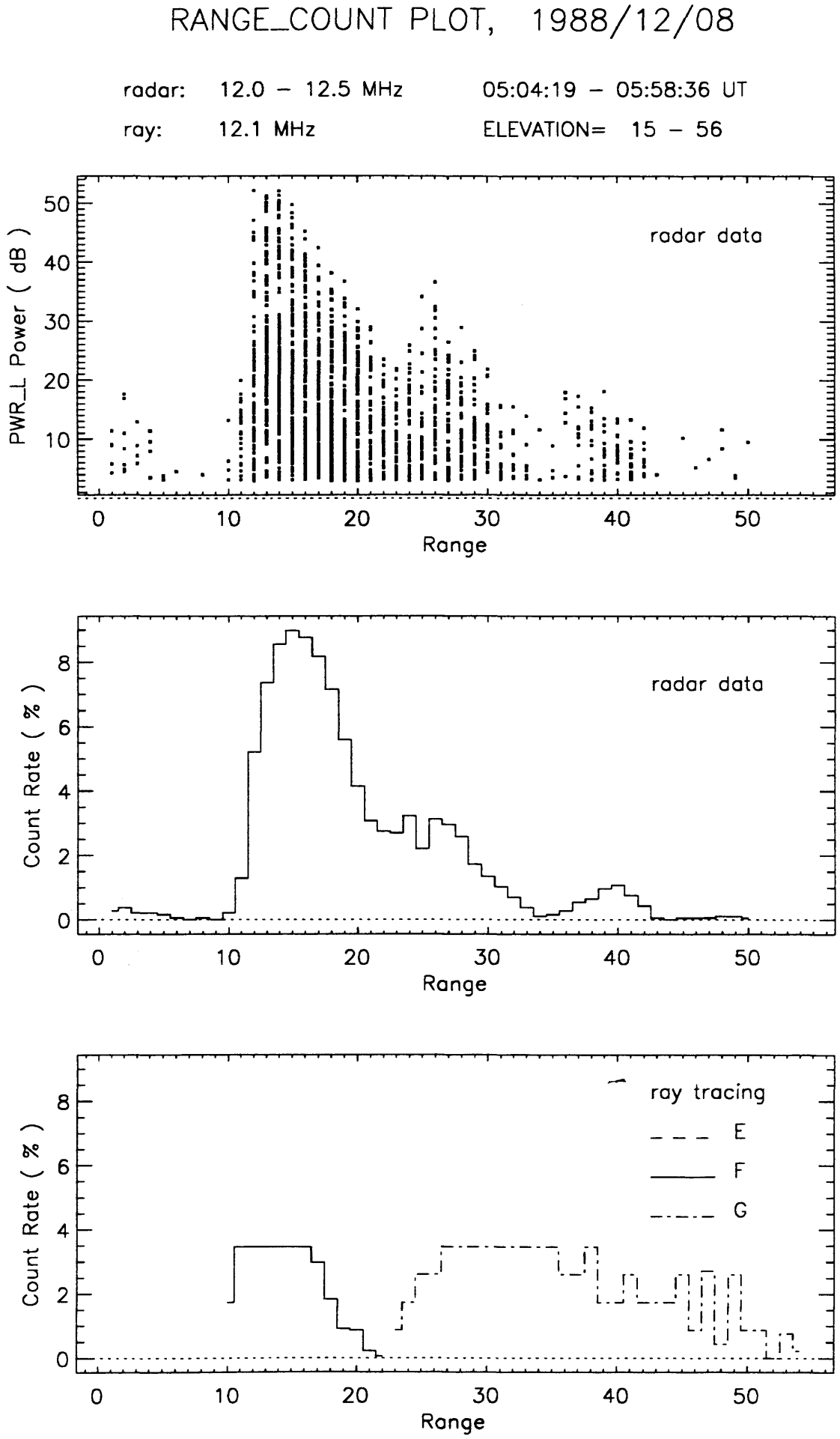

Figure 6.9 The beam-scan mode results and the range-bin statistical analysis

6.6.1 The ionospheric condition above Halley

On 8 December 1988, from 05:00:00 to 07:00:00 UT, it was geomagnetically quiet with k_p=2. A summary view of the Halley AIS ionogram data from 04:30:00 to 08:45:00 UT is shown in figure 6.10 and a corresponding skymap is given in figure 6.11. Some general features of the ionosphere during that period of time are summarised below.

(1) From 05:15:00 UT, there is clear evidence of persistent sporadic E, which should not be sampled when using POLAN to compute the real height profiles of electron density.
(2) Before 06:30:00 UT, the ionograms are a bit spread. But afterwards, ionogram data are of reasonably good quality.
(3) From the summary plot in figure 6.10, it is seen that foF2 increases steadily up to roughly 12 MHz, which is larger than expected for the same time in other years. The foE and foF1 are of normal values.
(4) From 07:00:00 UT, there is some evidence of gravity waves (see figures 5.3 and 6.10).
(5) From the skymap in figure 6.11, before 06:30 UT the data are spread, but after 06:30 UT signals are mainly from overhead.
(6) No evidence of tilts is seen from either the summary plot in figure 6.10 or the skymap in figure 6.11.

6.6.2 Difficulties in determining the radar beams in elevation

In this modelling study, it has been found that the most difficult and uncertain parameter to determine is the radar beams in elevation. The radar antenna is composed of many simple elements aligned in a straight line perpendicular to the central direction of radar field of view. It is easy to understand, by the principle of optical interference, that the final radar beam would be quite narrow in azimuth, but very broad in elevation. However, due to the challenge of making accurate experimental measurement, no good answer is available at the moment for the lower elevation angle of the radar beams. Some experiments were attempted on radar beam 8 at 12.3 MHz at Halley in 1993 and

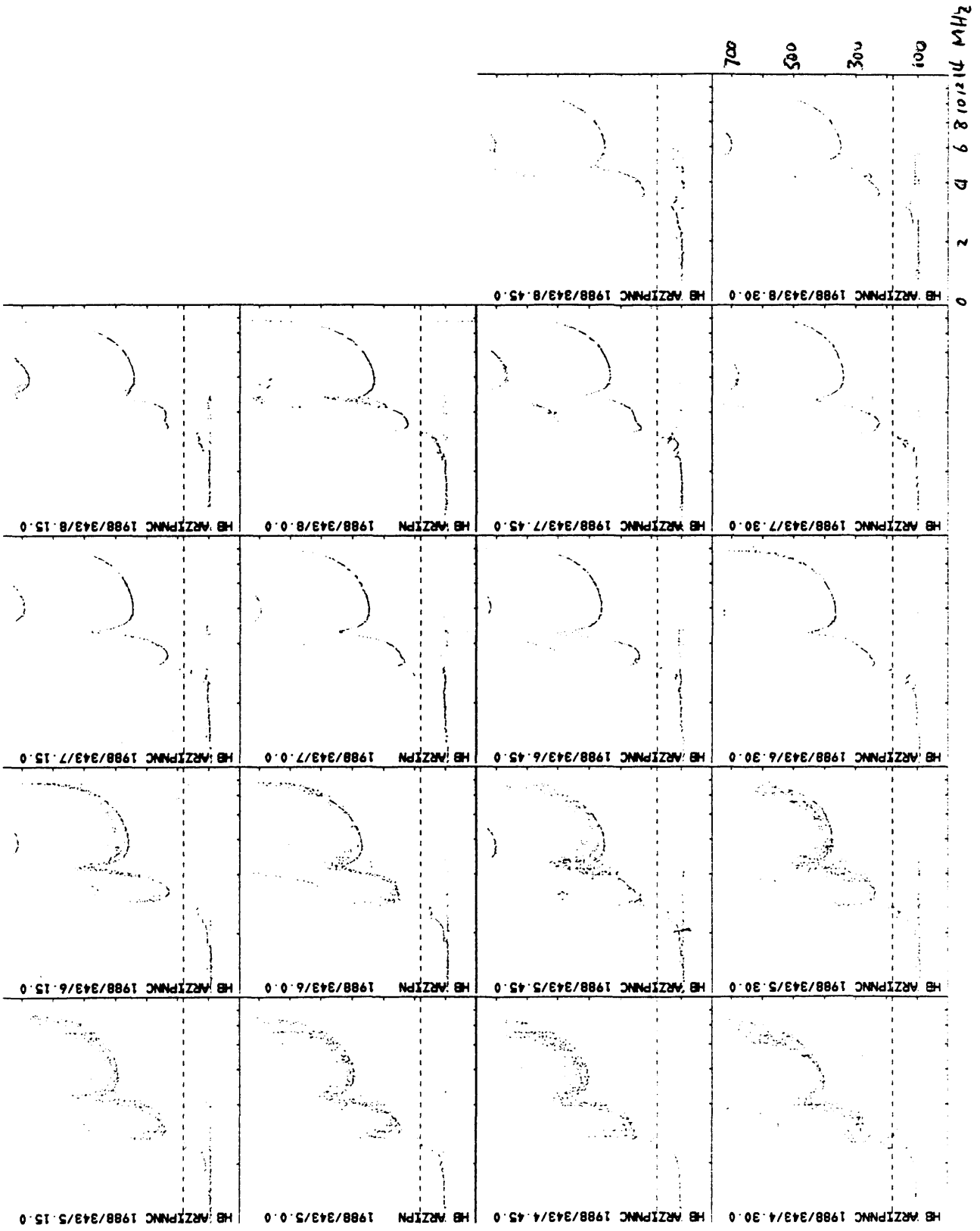

Figure 6.10 Summary plot of Halley AIS ionogram data

Figure 6.11 Sky map of Halley AIS dynasonde data

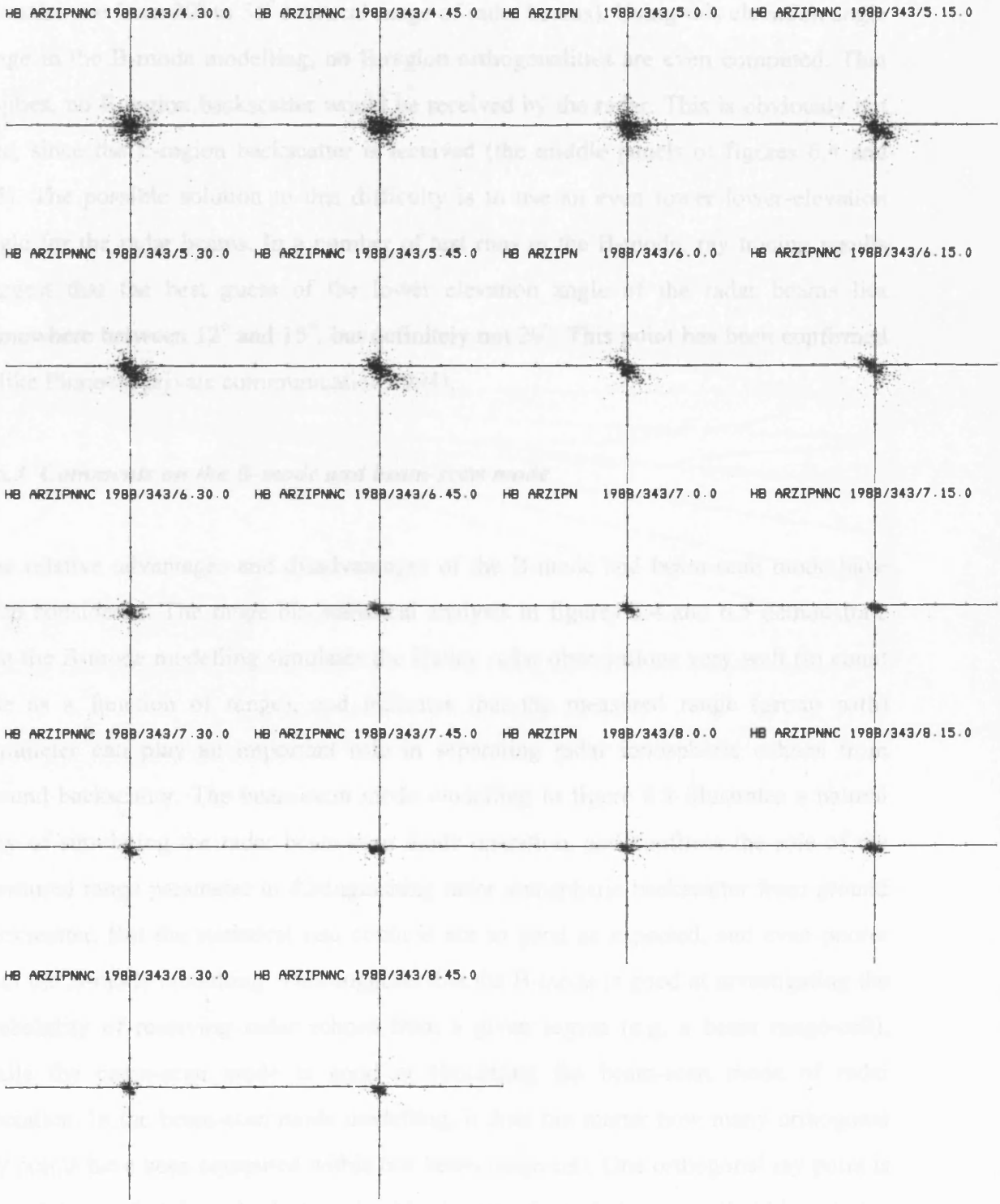

first-hand results were presented in the 1994 Orleans SuperDARN workshop (Pinnock *et al.*, 1994). These results are reproduced here. Figures 6.12 and 6.13 give the radar beam radiation pattern in azimuth and elevation, respectively. From the measurement, 38° is taken for the peak elevation angle and 36° for the beam width in elevation. Assume the radiation pattern is symmetric about the peak, then the radar beams in elevation are from 20° to 56° (vertical range of radar beams). Using this elevation angle range in the B-mode modelling, no E-region orthogonalities are even computed. That implies, no E-region backscatter would be received by the radar. This is obviously not true, since the E-region backscatter is received (the middle panels of figures 6.4 and 6.5). The possible solution to this difficulty is to use an even lower lower-elevation angle for the radar beams. In a number of test runs in the B-mode, ray tracing results suggest that the best guess of the lower elevation angle of the radar beams lies somewhere between 12° and 15°, but definitely not 20°. This point has been confirmed (Mike Pinnock, private communication 1994).

6.6.3 Comments on the B-mode and beam-scan mode

The relative advantages and disadvantages of the B-mode and beam-scan mode have been considered. The range-bin statistical analysis in figures 6.4 and 6.5 demonstrate that the B-mode modelling simulates the Halley radar observations very well (in count rate as a function of range), and indicates that the measured range (group path) parameter can play an important role in separating radar ionospheric echoes from ground backscatter. The beam-scan mode modelling in figure 6.8 illustrates a natural way of simulating the radar beam-scan mode operation, and confirms the role of the measured range parameter in distinguishing radar ionospheric backscatter from ground backscatter. But the statistical rate count is not as good as expected, and even poorer than the B-mode modelling. This suggests that the B-mode is good at investigating the probability of receiving radar echoes from a given region (e.g. a beam range-cell), while the beam-scan mode is good at simulating the beam-scan mode of radar operation. In the beam-scan mode modelling, it does not matter how many orthogonal ray points have been computed within one beam range-cell. One orthogonal ray point is enough to say that the radar has received backscatter from that range-cell. Although this

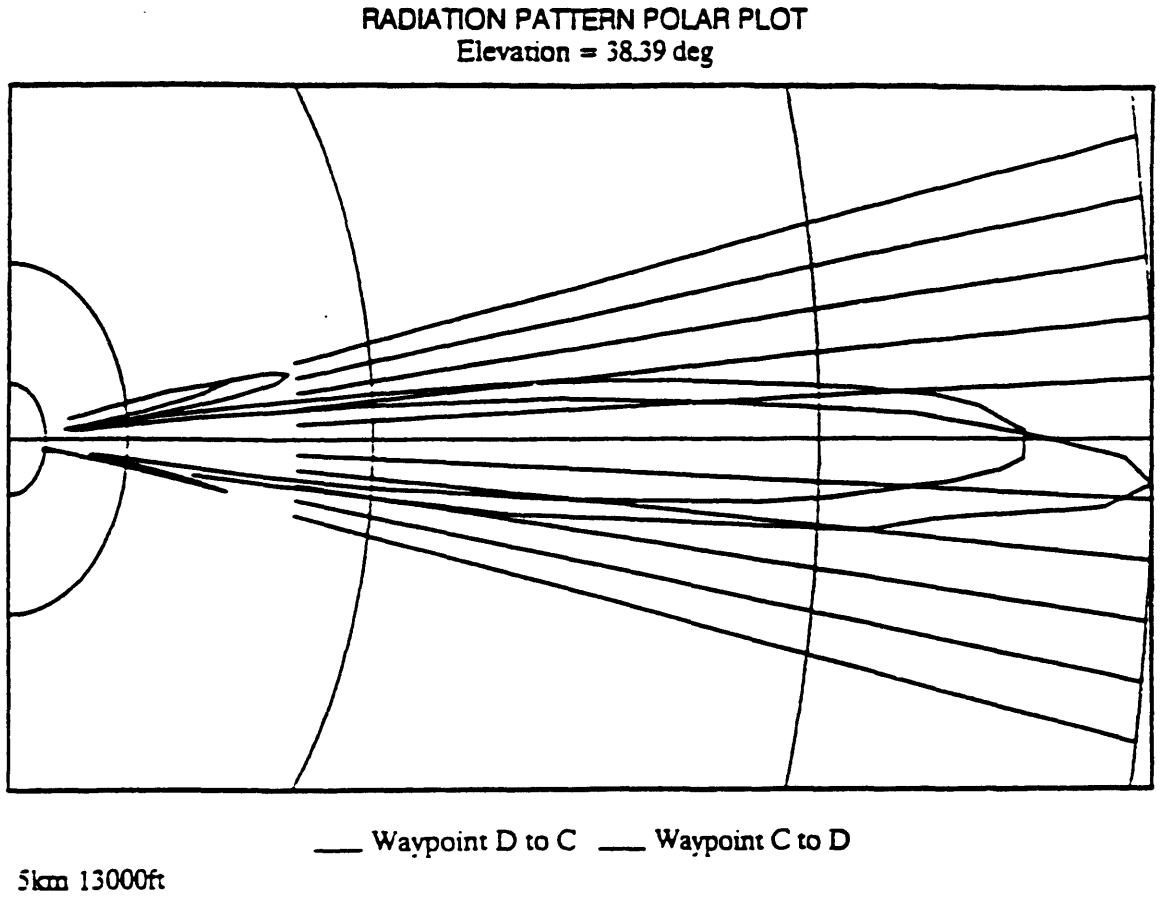

Figure 6.12 The Halley radar radiation pattern in azimuth
[After Pinnock *et al.*, 1994]

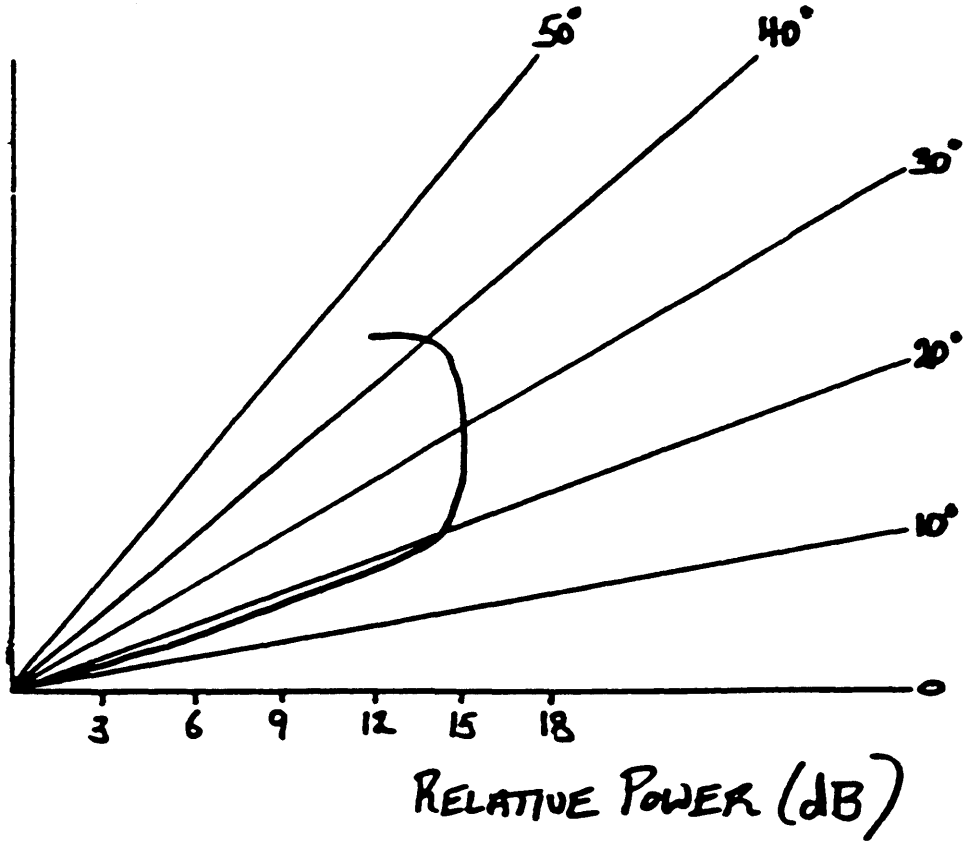

Figure 6.13 Antenna radiation pattern (in elevation) of the Halley HF radar in Antarctica (courtesy of M. Pinnock)

is quite similar to the way that the radar samples its received signals, the beam-scan mode actually suppresses the statistical meaning of the computation of orthogonal ray points. In fact, the more orthogonal ray points that are computed in a given beam range-cell, the better the chance for the radar to receive backscatter from the range-cell. It is this statistical meaning of the computation of orthogonal ray points which makes sense to the B-mode modelling.

6.7 SUMMARY

In this case study for the Halley HF radar in Antarctica, two different modes of ray tracing modelling are performed, the B-mode and beam-scan mode. In general, the modelling results simulate the radar observations very well in terms of the group path. The case study shows that the radar criteria used to distinguish radar ionospheric echoes from ground backscatter are not always sufficient, and the measured range (group path) parameter is also important in separating radar backscatters. Comments on the two modelling modes are given. That is, the B-mode is good at investigating the probability of receiving radar echoes from a given region (e.g. a beam range-cell), while the beam-scan mode is good at simulating the beam-scan mode of radar operation. The statistical meaning of the computation of orthogonal ray points is discussed.

CHAPTER 7

THE CUTLASS HF RADAR AND COMPUTER MODELLING

7.1 INTRODUCTION

This chapter discusses ray tracing computer modelling for the CUTLASS HF radar in Finland. EISCAT CP1 data measured in Tromso (Norway) are used for the model inputs of realistic ionospheric conditions. In this case study, both the beam-scan mode and radar summary plot modelling are performed, and comparison is made between modelling results and radar observations. Emphasis is given to the separation of radar ionospheric echoes from ground backscatter and the possible effect from the second hop HF ray propagation.

7.2 THE CUTLASS HF RADAR (IN FINLAND)

CUTLASS, the Co-operative UK Twin Located Auroral Sounding System, is a twin-station HF coherent backscatter radar system for the study of small-scale dynamics of the high-latitude ionosphere. One radar is located in Iceland and the other is in Finland, and both look north into a volume over and to the north of Scandinavia, covering Tromso and Svalbard Archipelago, see figure 7.1. The Finland radar started in operation in February 1995 and the Iceland radar in the following autumn, November 1995. The use of these two radars enables the ionospheric convection velocity vector perpendicular to the earth's magnetic field to be resolved.

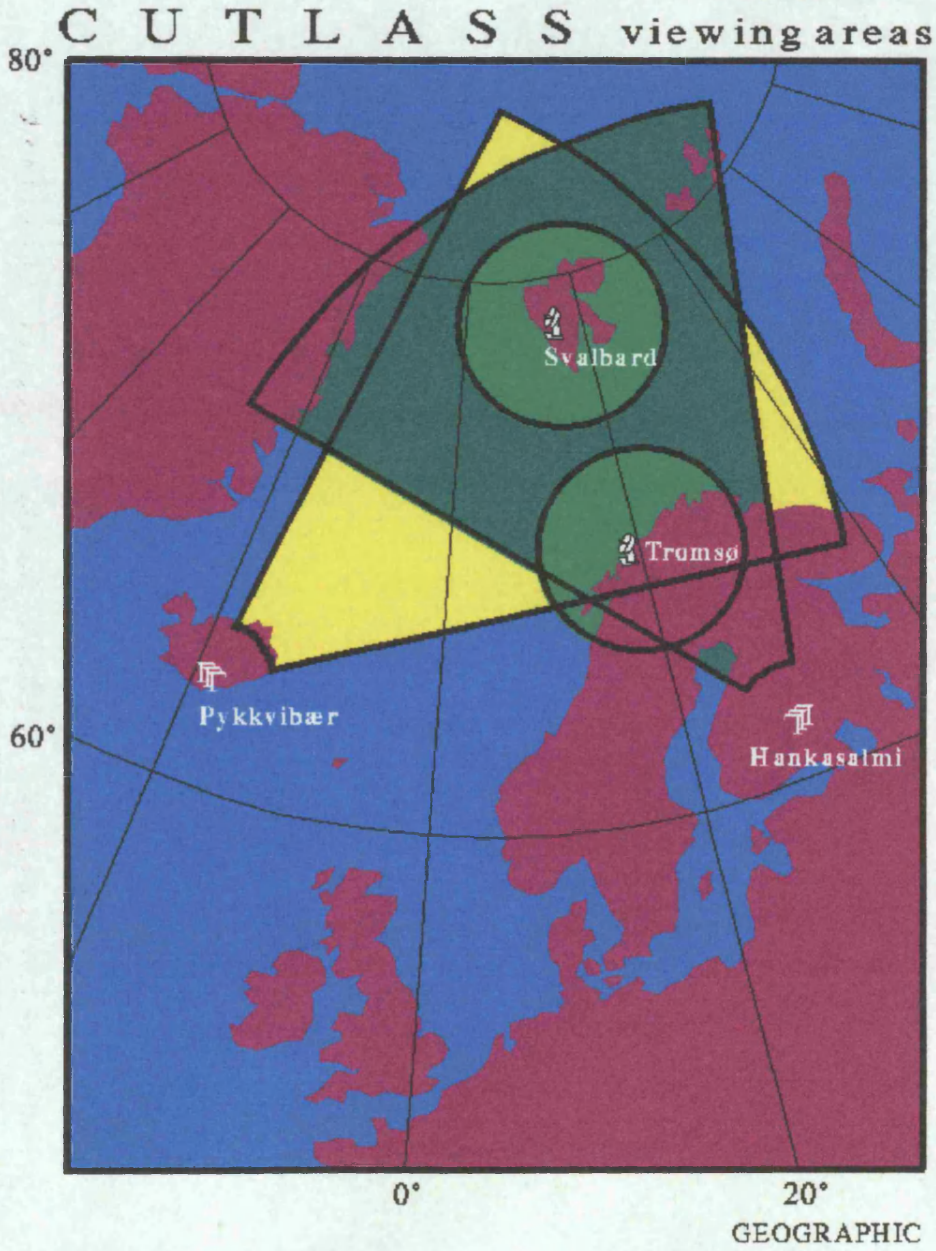

Figure 7.1 Viewing area of the CUTLASS HF radars

Each radar has two log-periodic antenna arrays. The main antenna array has 16 transmitting antennas, separated by 15 m, with both transmit and receive capability, and in front of this an interferometer of 4 antennas with receive capability only, which allows the (elevation) angle of arrival of the backscattered signals to be determined.

The CUTLASS HF radars also form part of SuperDARN, an international network of similar radars covering almost 180 degrees longitude in the northern hemisphere and including conjugate stations in the Antarctica. This network will for the first time offer a truly global atmospheric monitoring which is so important if we are to understand our planetary environment.

7.2.1 Radar basic operational parameters

Table 7.1 summarises the basic operational parameters for the CUTLASS HF radar in Finland.

Table 7.1 Radar basic operational parameters

location:	Transmitter location (62.32^{o} N, 26.60^{o} E)
antenna mast:	15 meters above the ground
total number of beams:	16 beams, numbered from 0 to 15 in clockwise
beam width:	2.5^{o} at 20 MHz and 6° at 8 MHz (3 dB)
angular separation:	3.3^{o} (between two adjacent beams)
central azimuth:	-12° (from the north)
total azimuth sweep:	52.8^{o}
working frequency:	8 - 20 MHz
peak elevation angle:	25°
total elevation angle:	12° - 41° (3 dB)
integration time:	6 seconds per beam, and 96 seconds per scan
first range:	180 km (default)
range resolution:	45 km (default)
total range gates:	75 range gates

The values for the above listed radar peak elevation angle and total elevation angle are taken from figure 7.2, the antenna (elevation) radiation pattern. It is shown and suggested in the figure that the beam width in elevation is based on 3 dB attenuation in power. The total elevation angle is from 12° to 41°. According to a series of modelling trials, it seems that 10 dB attenuation in power would be more appropriate for the purpose of comparison of modelling results with radar observations. Therefore, the total elevation angle goes from 5° to 55° (see figure 7.2). All discussions in this chapter are based on this assumption of 10 dB attenuation in power.

7.2.2 Radar ground backscatter

The radar ground backscatter is defined as scatter, whose Doppler velocity and spectral width are both less than 50 m/s. The situations for the CUTLASS HF radar in Finland might be quite different from that of the Halley HF radar in Antarctica, where most of the land is covered with very thick snow/ice sheet. For the CUTLASS Finland HF radar, there is no such thick snow/ice covering. Therefore, ground backscatter from both land and sea, and from both first hop and second hop is expected.

7.3 THE IONOSPHERE ABOVE TROMSO

In this case study, the model inputs of realistic ionospheric conditions are based upon the CP1 data measured in Tromso. The profiles of electron density consist of two parts, the alternating code data (below 142 km altitude) and long pulse data (above 142 km). Figure 7.3 shows 24 CP1 profiles of electron density for 1 March 1995, one for each hour. The figure illustrates that the CP1 data may sometimes display quite large auroral E, (e.g. at 20:05:05, 21:00:05, and 22:05:05 UT of figure 7.3), which makes the Gaussian extrapolation scheme of TABLEX vital to the modelling study (see chapter 4). This feature of large auroral E will not be seen from the profiles of electron density computed by POLAN (see chapter 5). Figure 7.3 also shows that there is a persistent non-trivial discrepancy in electron density between the alternating code and long pulse data at around 142 km altitude. This discrepancy in electron density may produce a visible distortion on the ray paths at that altitude, and then affect the computation of ionospheric orthogonal and ground ray points. Except for corrupt profiles of electron

SPECIAL NOTICE

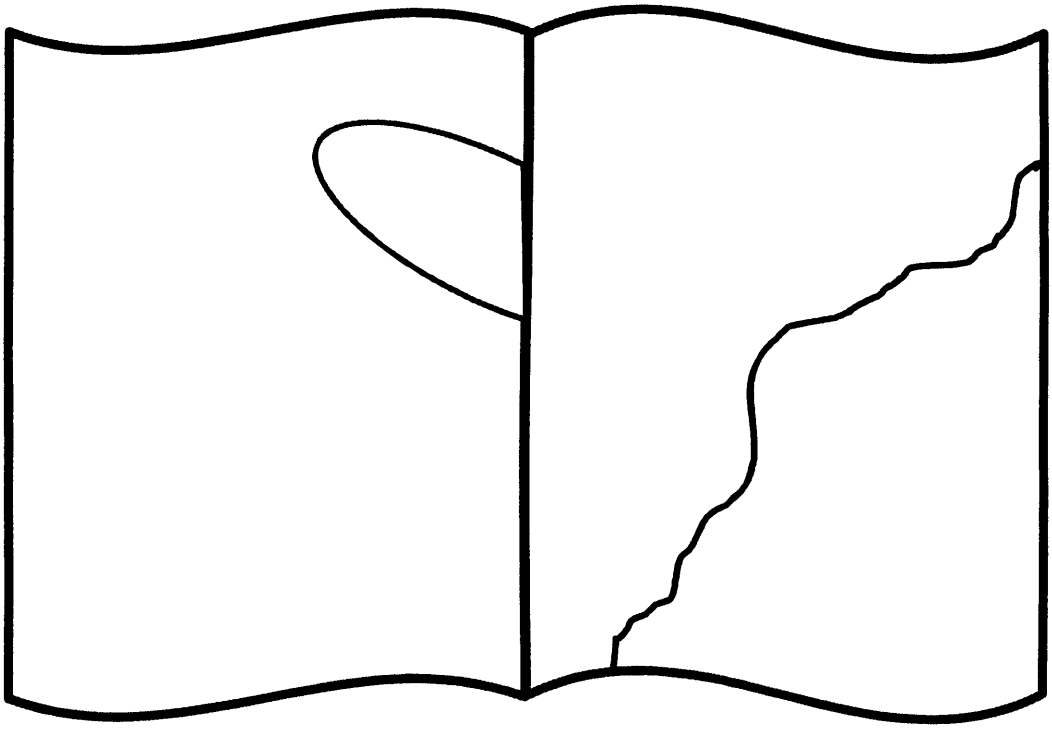

DAMAGED TEXT - INCOMPLETE IMAGE

al ground

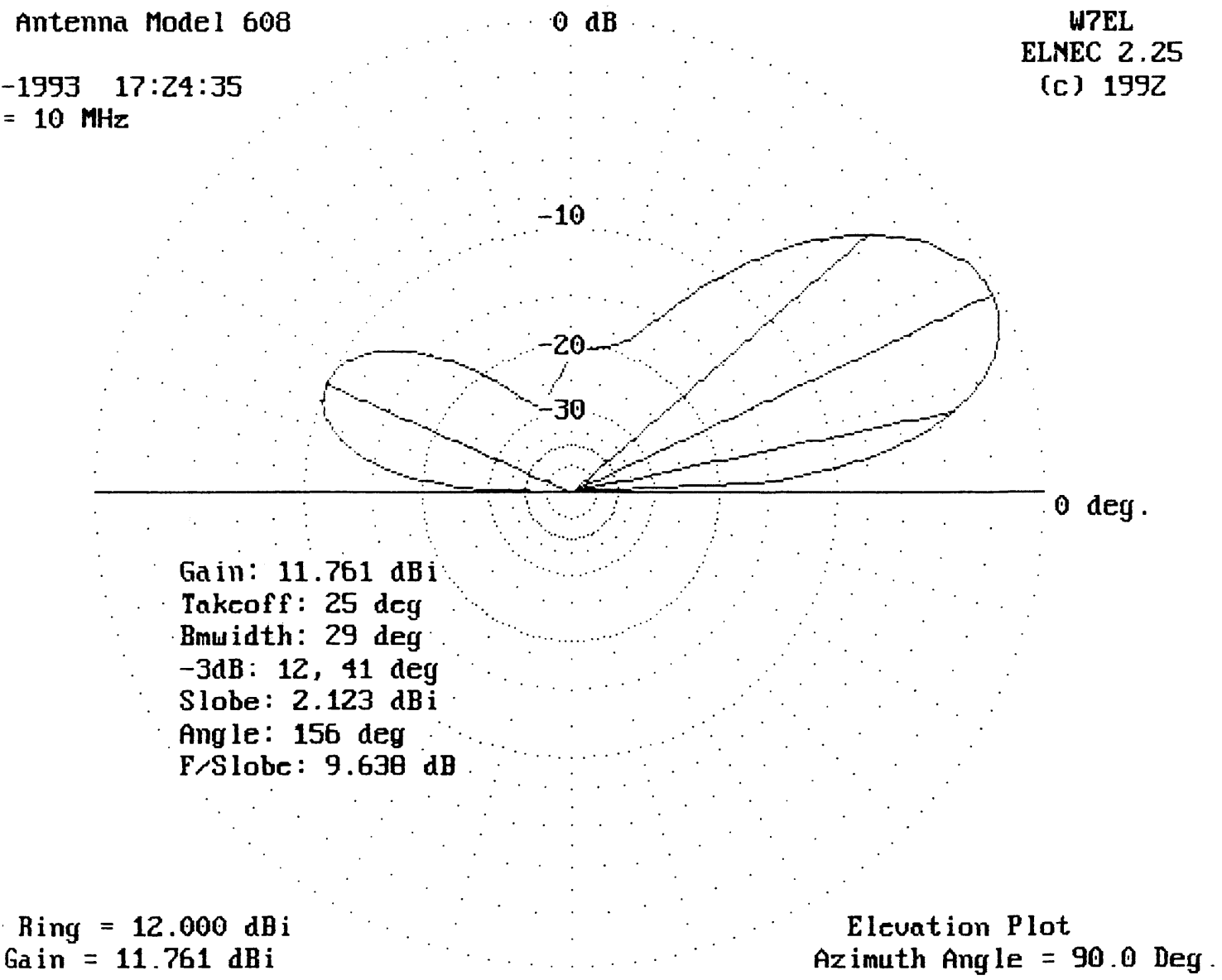

Figure 7.2 Antenna radiation pattern (elevation plot) of the CUTLASS HF radar in Finland

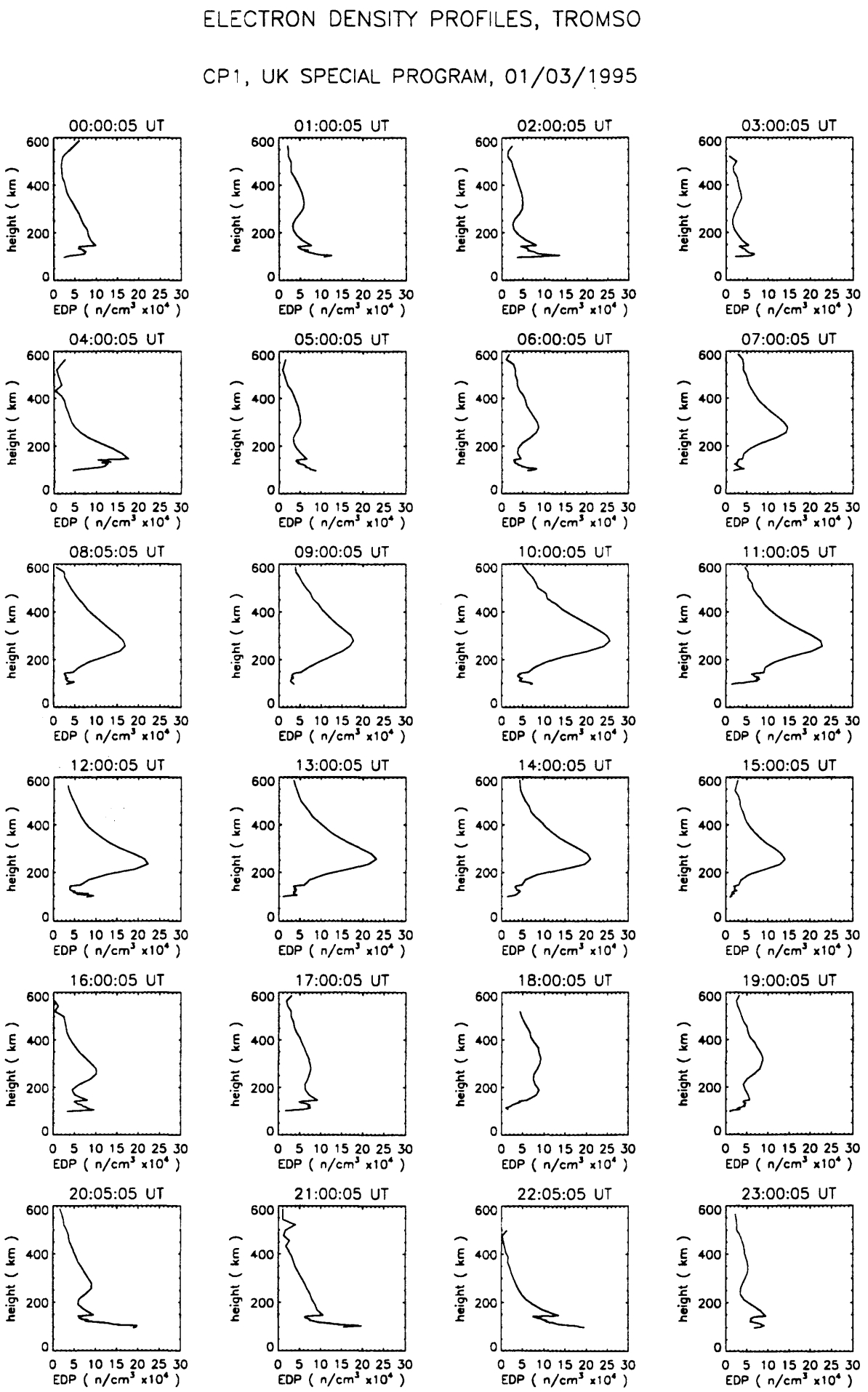

Figure 7.3 The CP1 data from the EISCAT UHF experiment at Tromso

density when spectral fitting failed and the above mentioned discrepancy in electron density between the alternating code and long pulse data, the CP1 data can almost always give quite reasonable profiles of electron density regardless of various small ionospheric disturbances.

7.4 BEAM-SCAN MODE MODELLING

Ray tracing modelling in the beam-scan mode traces each of the radar 16 beams individually, one by one from beam 0 to beam 15 (see chapter 5). The advantage of this mode is that it is easy to compare ray tracing results with radar scan data. Detailed discussion of the beam-scan mode modelling and comparison with the Finland radar observations is given below.

7.4.1 Ray tracing/radar beam parameters

Table 7.2 gives the azimuthal spread of all 16 radar beams, from beam 0 to beam 15.

Table 7.2 Beam parameters of the CUTLASS HF radar, Finland

Beam No	Beam Central Position	Beam Spread
0	-37	(-40, -34)
1	-33.7	(-36.7, -30.7)
2	-30.4	(-33.4, -27.4)
3	-27.1	(-30.1, -24.1)
4	-23.8	(-26.8, -20.8)
5	-20.5	(-23.5, -17.5)
6	-17.2	(-20.2, -14.2)
7	-13.9	(-16.9, -10.9)
The central azimuth: -12.25 degrees from the north		
8	-10.6	(-13.6, -7.6)
9	-7.3	(-10.3, -4.3)
10	-4.0	(-7.0, -1.0)
11	-0.7	(-3.7, 2.3)

12	2.6	(-0.4, 5.6)
13	5.9	(2.9, 8.9)
14	9.2	(6.2, 12.2)
15	12.5	(9.5, 15.5)

For the CUTLASS HF radar in Finland, one scan consists of 16 beams (from beam 0 to beam 15 in clockwise). The radar beam-width is 6 degrees at 8 MHz and 2.5 degrees at 20 MHz. In this case study, we take 6 degrees for 10 MHz.

7.4.2 Vertical ray paths and orthogonal ray points

Before doing any complex beam-scan mode modelling and comparison with the Finland radar observations, it is instructive to look at three plots of vertical projections of the ray paths of beam 5 to gain an initial impression of the first and second hop HF ray propagation and associated ionospheric orthogonal and ground ray points. Figures 7.4, 7.5, and 7.6 show three vertical projections of the ray paths of beam 5 for 1 March 1995 at 00:00:05 UT, 05:00:05 UT, and 08:05:05 UT, respectively. For simplicity and readability, the rays are traced at one azimuth angle only, that is -20.5° from the north, the central azimuth angle of beam 5, which is the beam that passes through the CP1 pointing direction. For all three plots, the ray elevation angle goes from 5° to 55° and both first and second hop HF ray propagation are modelled at a frequency of 10 MHz. Small vertical bars are employed to indicate where orthogonal conditions are satisfied. Theoretically, the orthogonality means that small-scale density irregularities could be detectable by a ground-based HF coherent backscatter radar system if the density fluctuation level is high enough there.

Figure 7.4 shows both first and second hop ray propagation at 00:00:05 UT. Plasma density irregularities are detectable on up-leg ray paths (see small vertical bars on the up-leg ray paths of both first and second hop ray propagation). Figure 7.5 illustrates that at 05:00:05 UT plasma irregularities are only detectable by the first hop up-leg rays and no ionospheric backscatter is received at all from the second hop ray propagation. Although there is no ionospheric backscatter from the second hop ray propagation, the

SPECIAL NOTICE

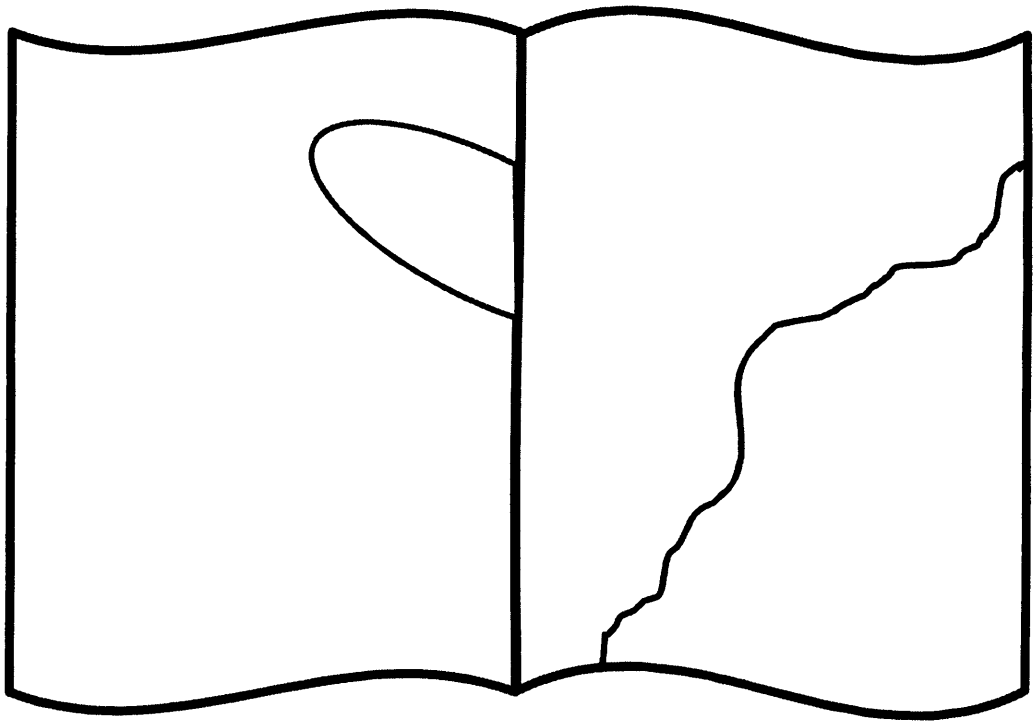

DAMAGED TEXT - INCOMPLETE IMAGE

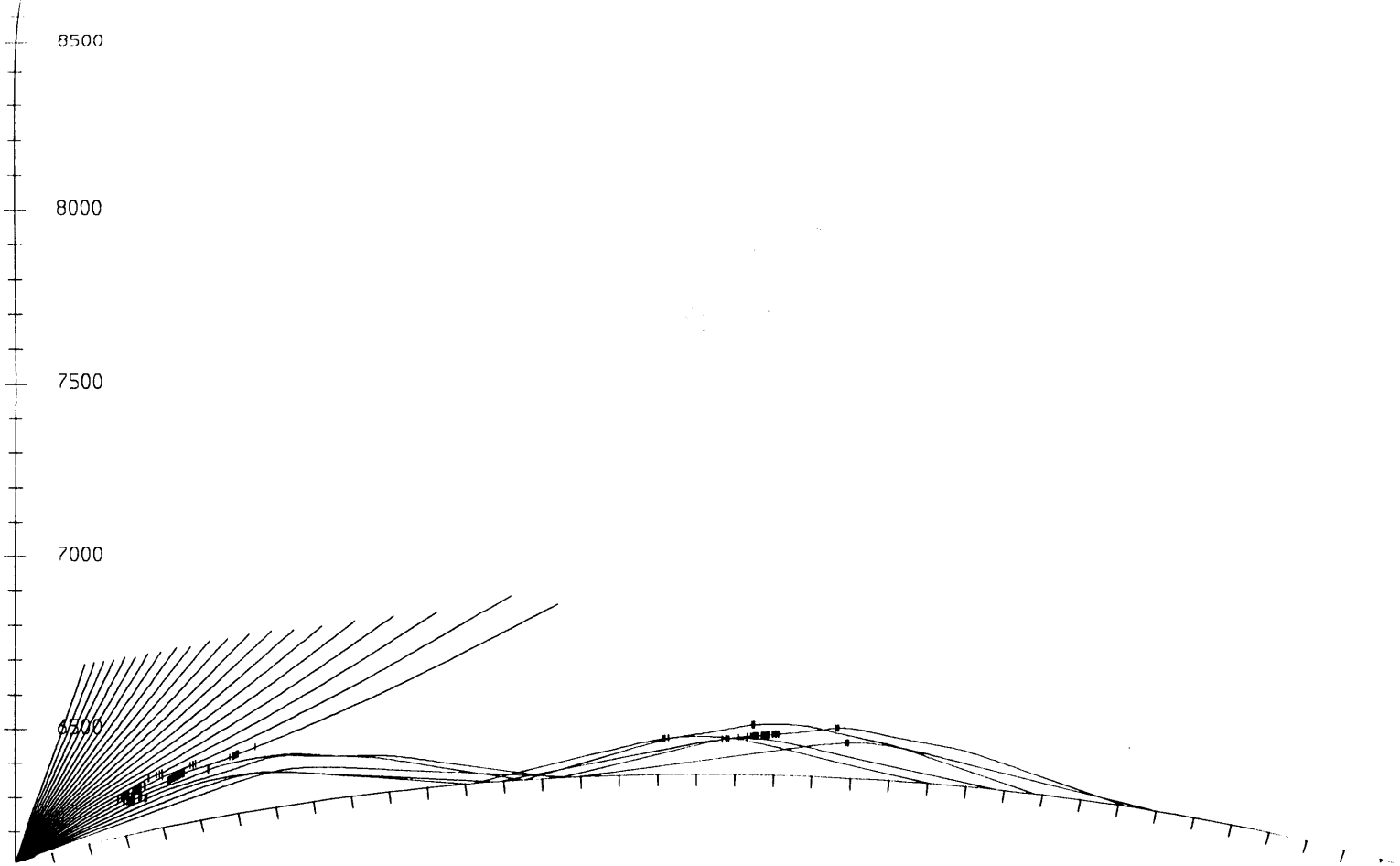

tromso, 00:00:05 01/03/1995

BAS

F= 10.0000, INI AZ= -20.5000, FIN AZ= -20.5000, ORDINARY

INI EL= 5.0000, FIN EL= 55.0000, 100.0000 KM BETWEEN TICKMARKS

Figure 7.4

SPECIAL NOTICE

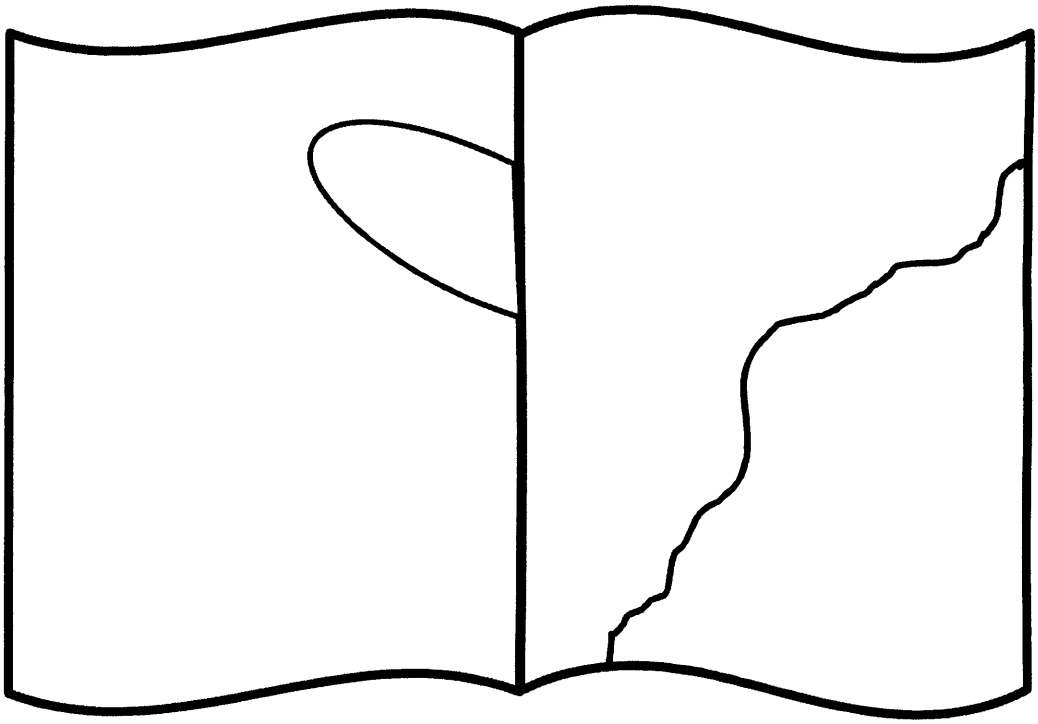

DAMAGED TEXT - INCOMPLETE IMAGE

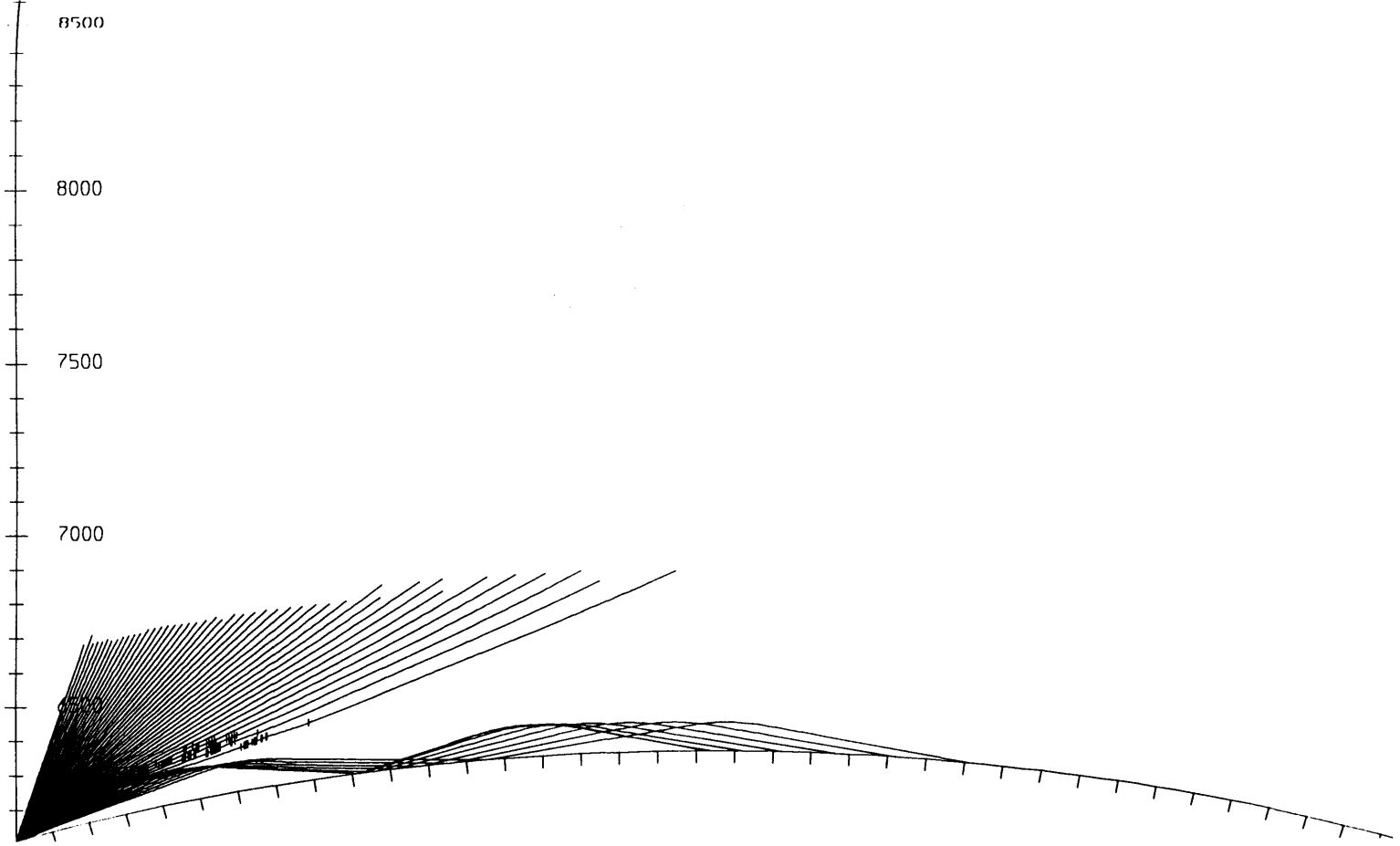

tromso, 05:00:05 01/03/1995

BAS

F= 10.0000, INI AZ= -20.5000, FIN AZ= -20.5000, ORDINARY

INI EL= 5.0000, FIN EL= 55.0000, 100.0000 KM BETWEEN TICKMARKS

Figure 7.5

SPECIAL NOTICE

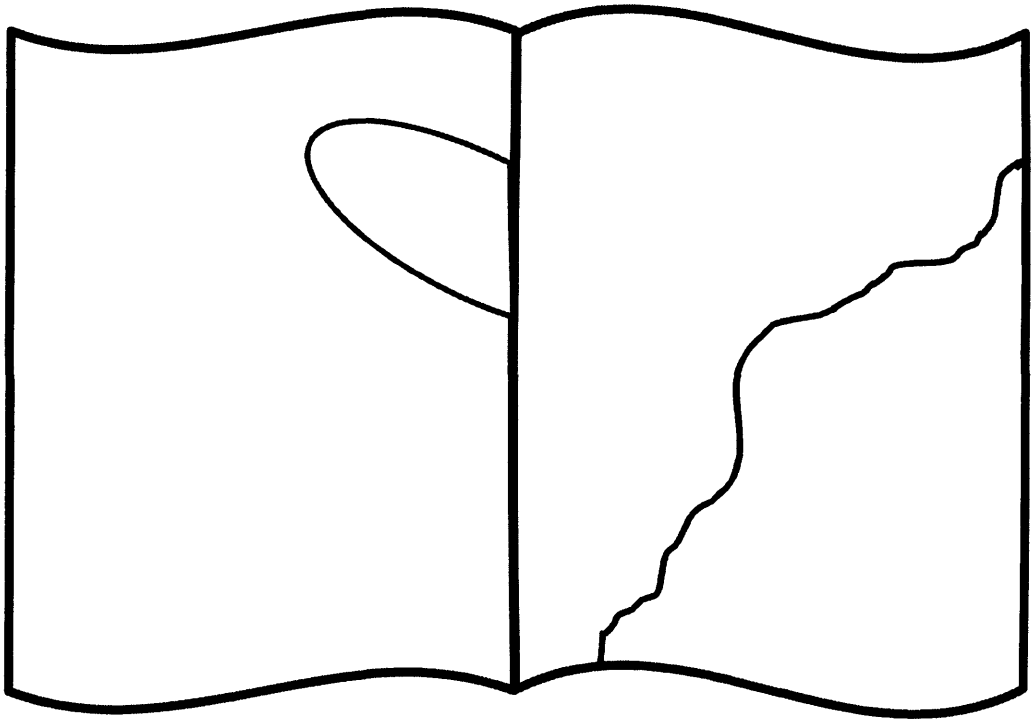

DAMAGED TEXT - INCOMPLETE IMAGE

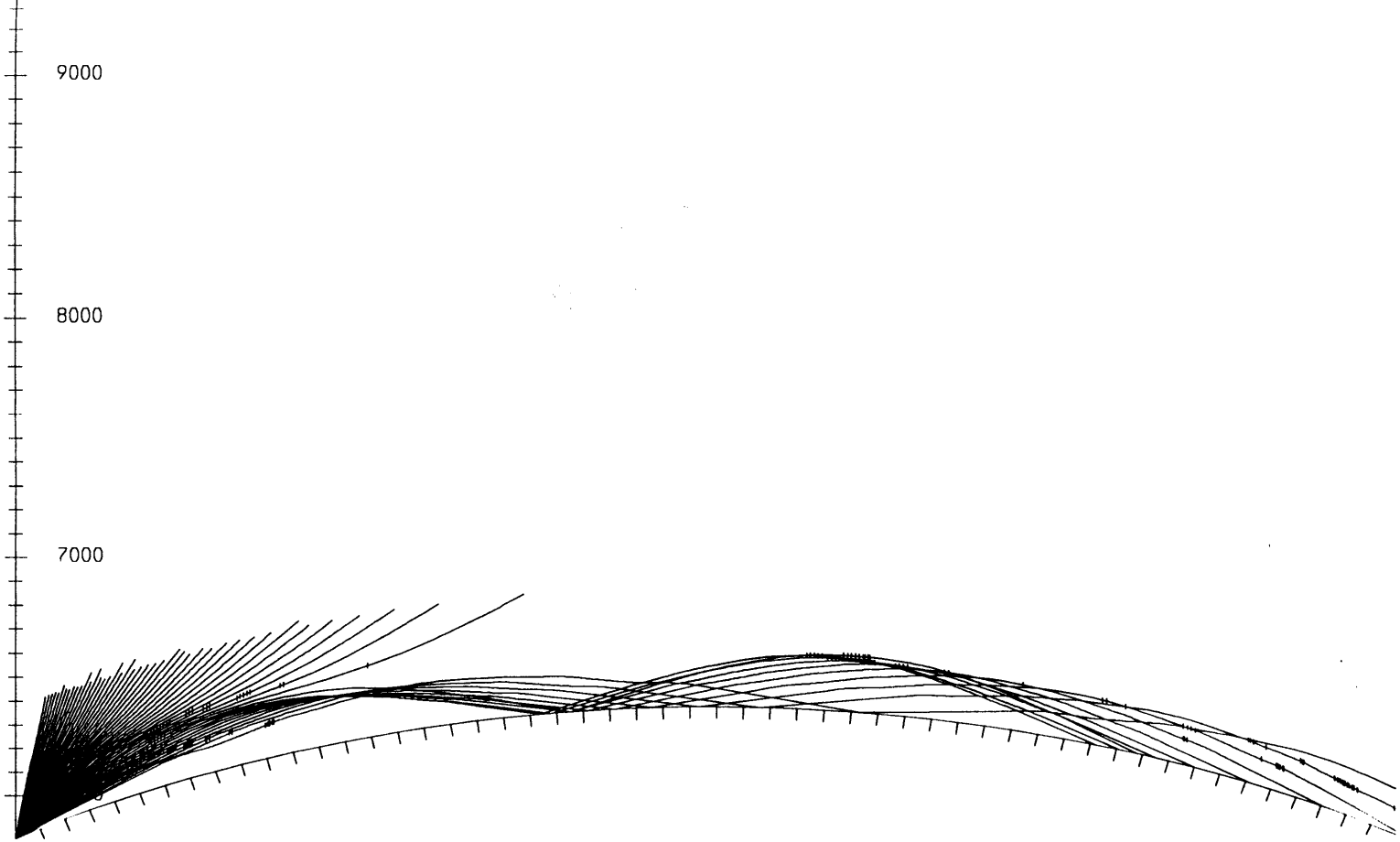

tromso, 08:05:05 01/03/1995

BAS

F= 10.0000, INI AZ= -20.5000, FIN AZ= -20.5000, ORDINARY

INI EL= 5.0000, FIN EL= 55.0000, 100.0000 KM BETWEEN TICKMARKS

Figure 7.6

radar may still be able to receive some ground backscatter from the second hop. Figure 7.6 shows that the radar, at 08:05:05 UT, receives much closer range ionospheric backscatter (orthogonal ray points) from the first hop. They are E-region backscatter. For the second hop ray propagation, ionospheric orthogonal ray points are no longer on the up-leg ray paths, but on the down-going ray paths.

The above three examples have demonstrated that the detection of radar backscatter by a ground-based HF coherent radar system may vary greatly with the ionospheric conditions and the geometry of the earth's magnetic field lines. It is these factors that make the interpretation of radar data and computer modelling very complicated.

7.4.3 Beam-scan mode modelling and comparison to radar observations

Figure 7.7 shows 24 scan plots of the Finland radar for 1 March 1995. They are colour-scaled in backscatter power. The radar data are selected for 6 UT times, i.e. 09:00 UT, 10:00 UT, 11:00 UT, 12:00 UT, 13:00 UT, and 14:00 UT hours. Figure 7.8 shows the same radar data, but arranged in velocity/region plots based upon the radar criteria of phase velocity and spectral width. The horizontal colourbar gives the phase velocity of plasma waves with positive number for waves moving towards the radar and negative number for waves moving away from it. The ground backscatter is plotted in grey. In figure 7.8, most of the radar received signals are identified as ground backscatter.

For the above six selected UT times, ray tracing modelling in the beam-scan mode is performed at 10 MHz. Results are shown in figures 7.9 for one-hop and 7.10 for two-hop ray propagation, and both figures are colour-scaled in altitudes of ray points. The ground ray points are again plotted in grey. For the convenience of comparison, six radar scan plots are reproduced in figures 7.11 and 7.12, colour-scaled in backscatter power and phase velocity/regions, respectively. Both the radar data and ray tracing results are plotted up to range-bin 75, the maximum observing range gate of the CUTLASS HF radar. Anything beyond this range gate is ignored.

Below is given a detailed comparison between the ray tracing results in figures 7.9 (one-hop) and 7.10 (two-hop), and the radar observations in figures 7.11 and 7.12.

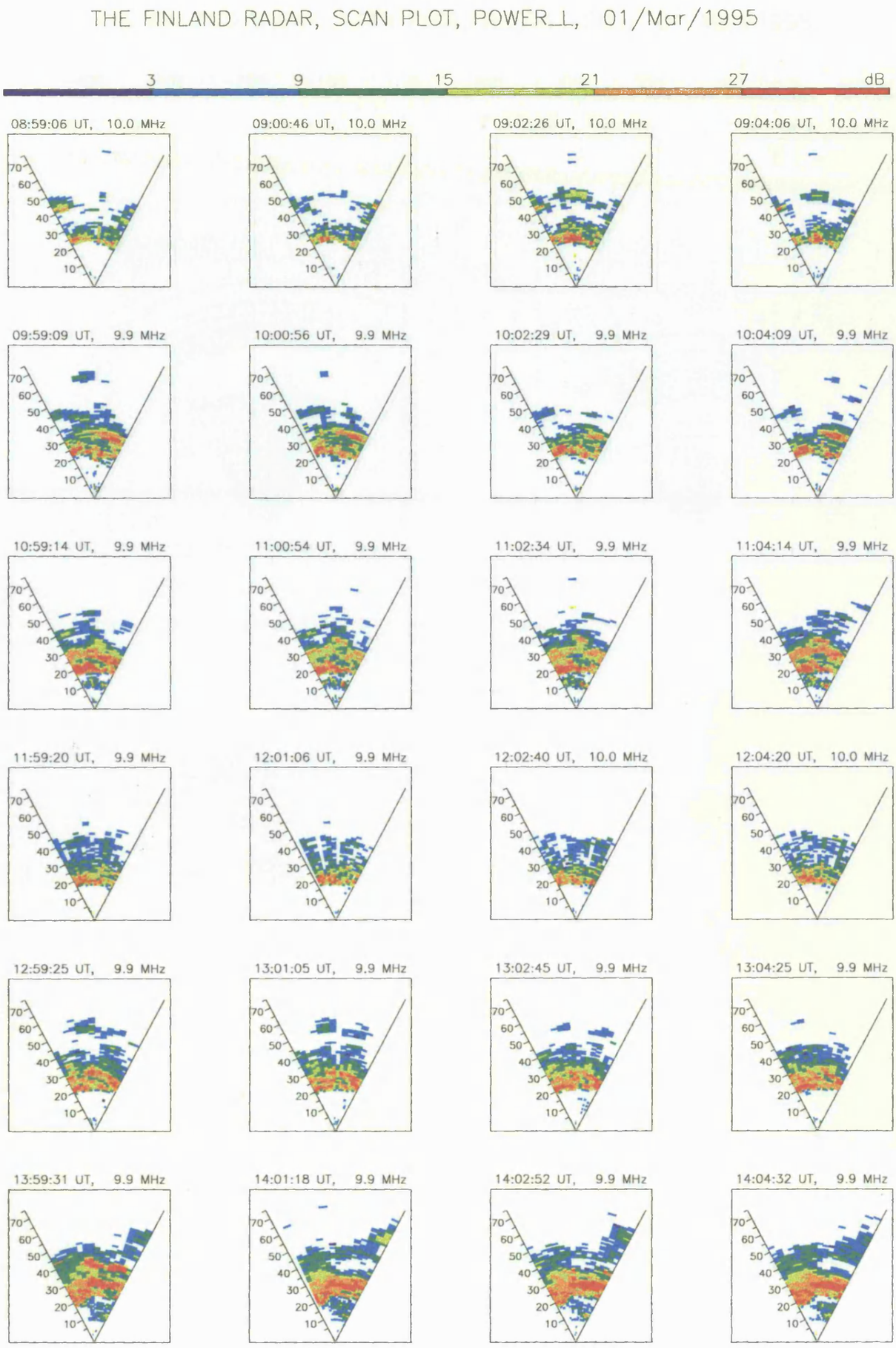

Figure 7.7 The Finland radar 6 sets of scan plots in backscatter power

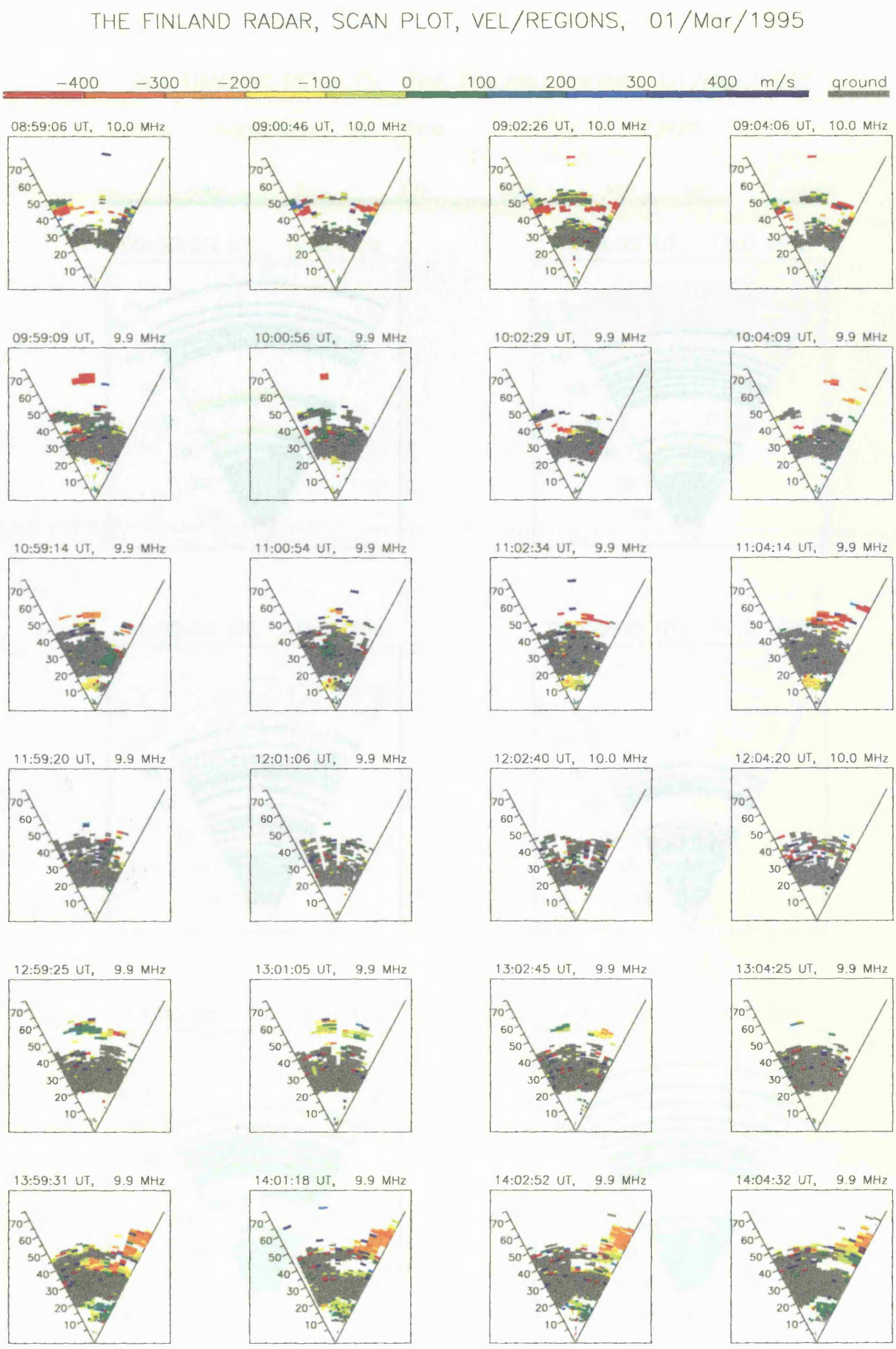

Figure 7.8 The Finland radar 6 sets of scan plots in velocity/region

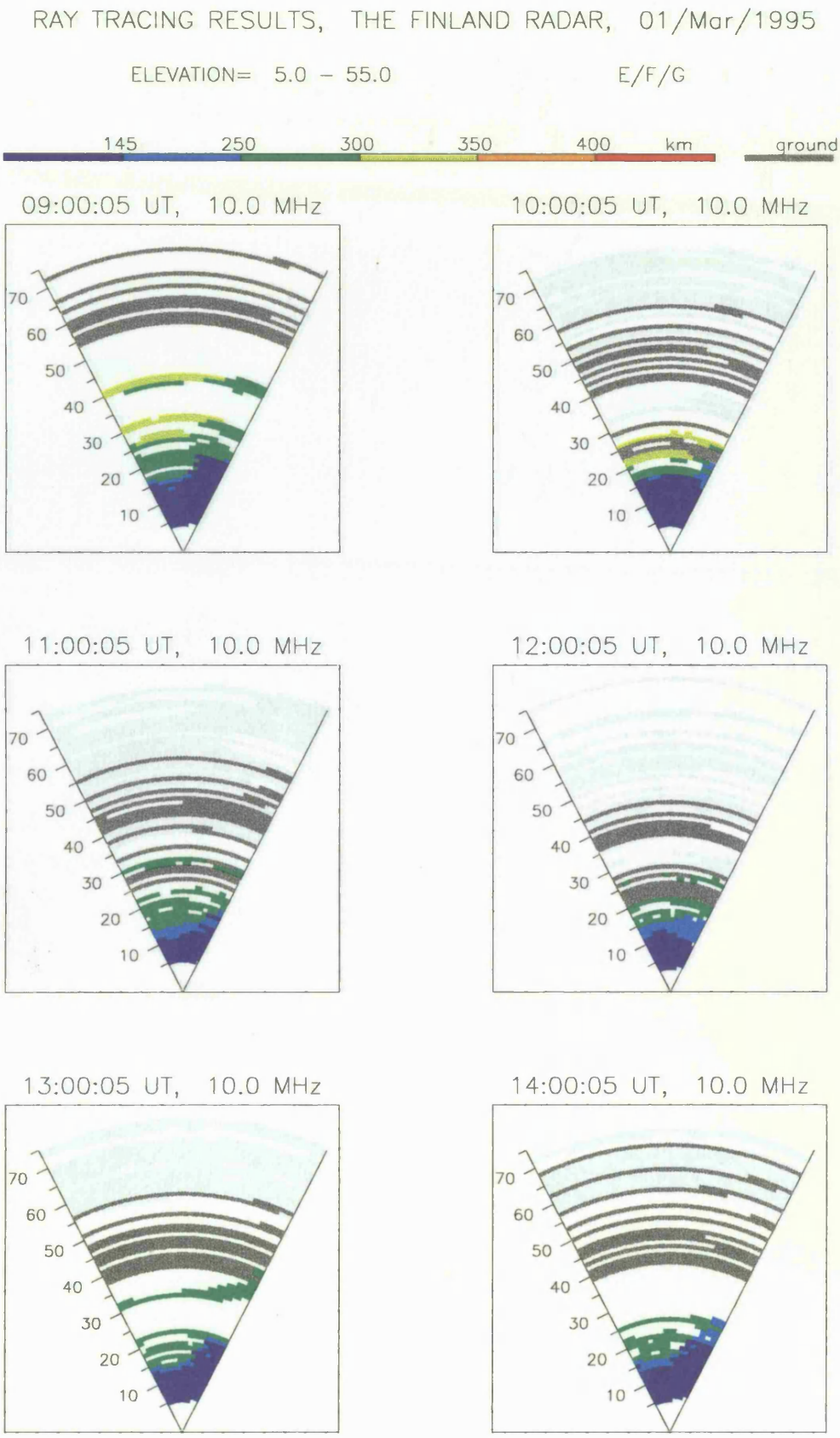

Figure 7.9 Ray tracing modelling in the beam-scan mode (one-hop ray propagation)

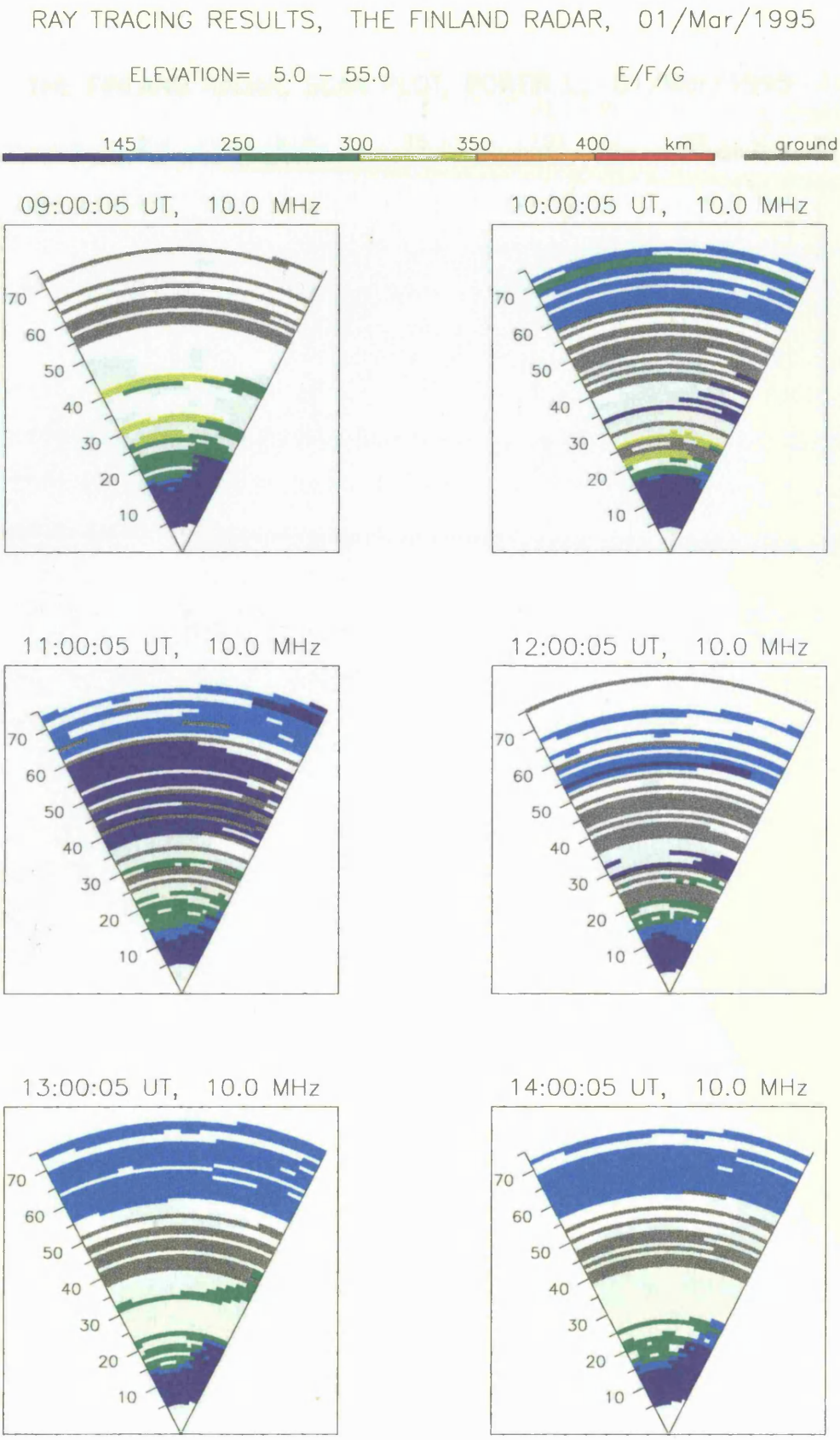

Figure 7.10 Ray tracing modelling in the beam-scan mode (two-hop ray propagation)

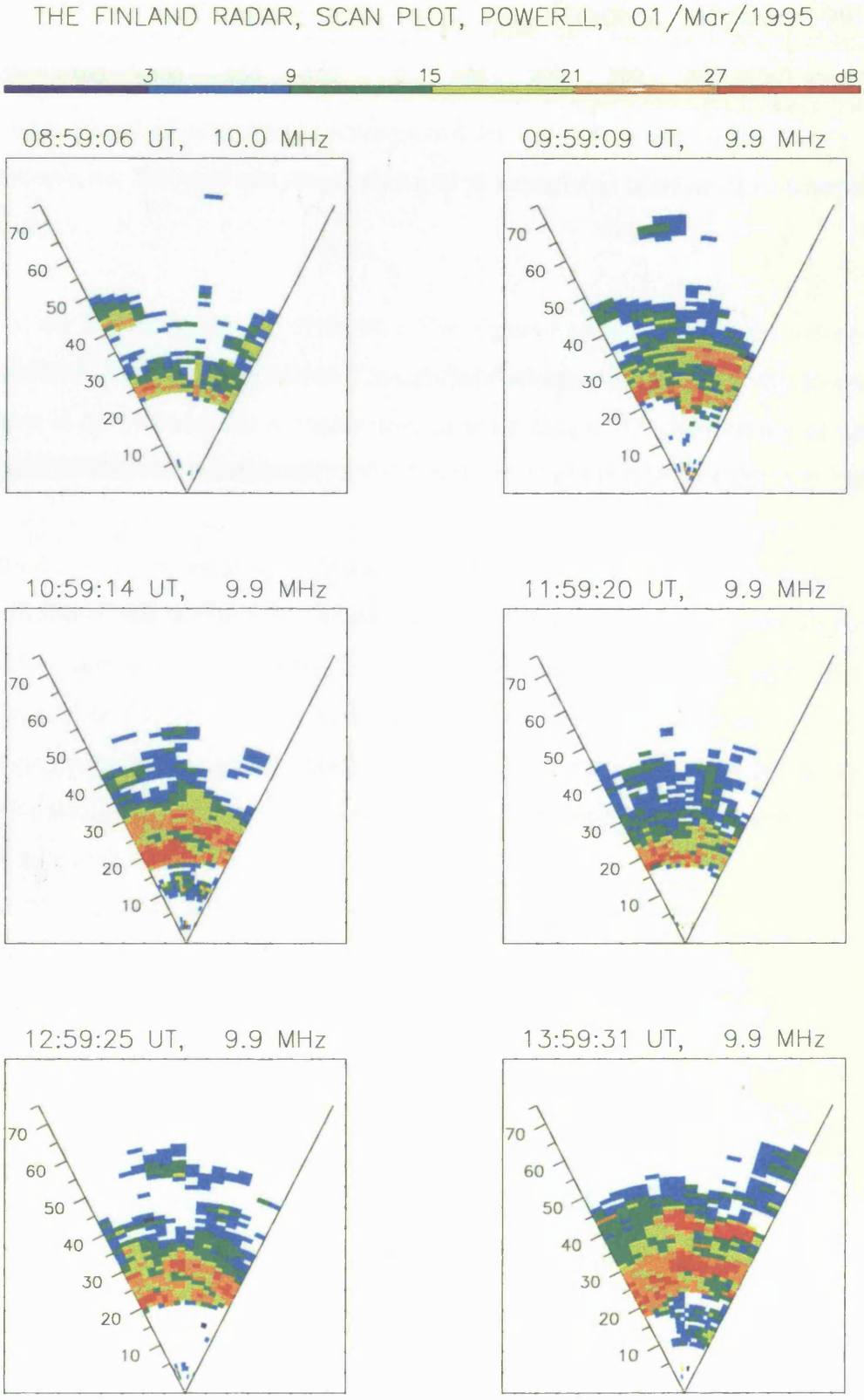

Figure 7.11 The Finland radar scan plots in backscatter power

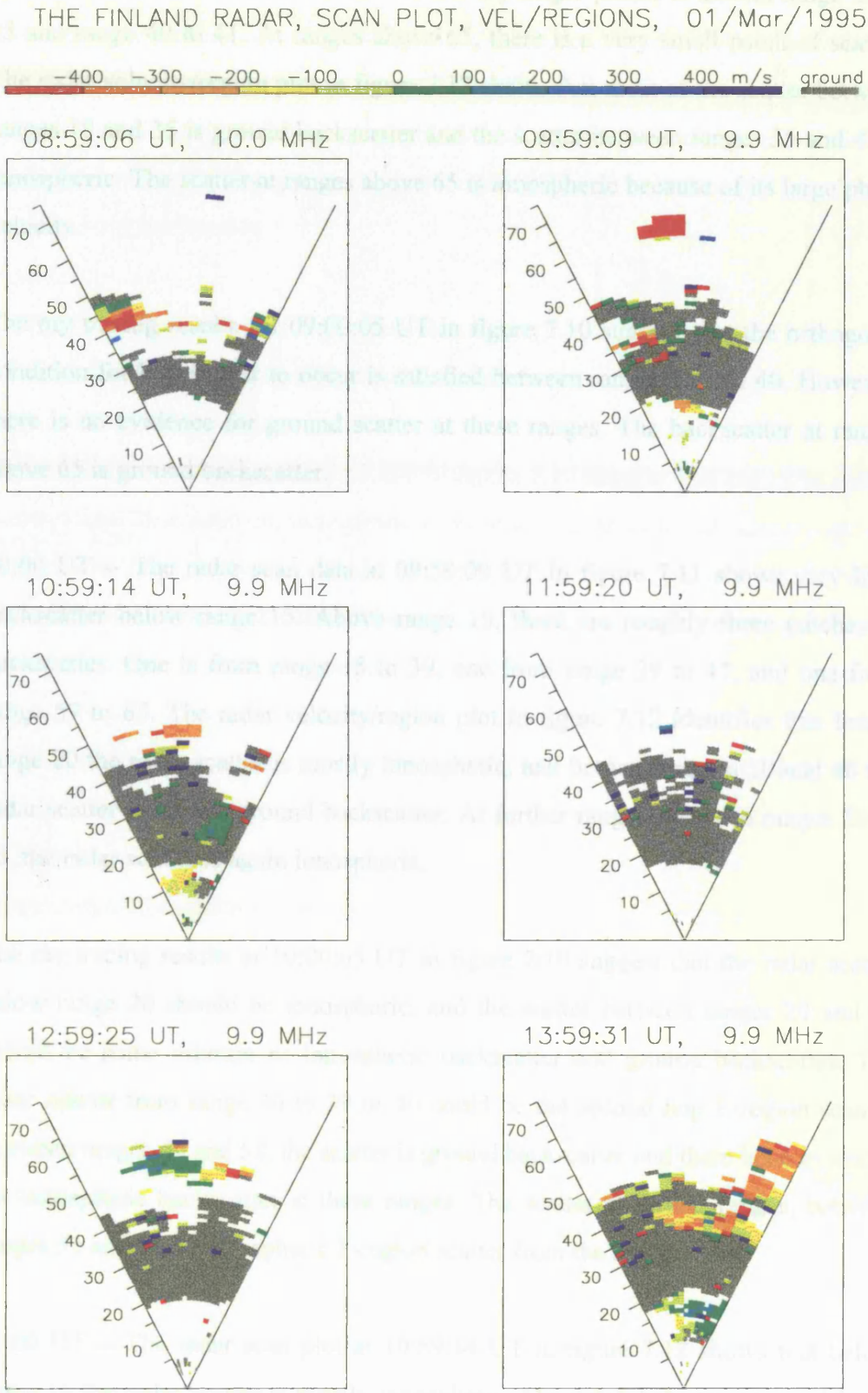

Figure 7.12 The Finland radar scan plots in velocity/region

(1) 09:00 UT -- The Finland radar scan plot at 08:59:06 UT in figure 7.11 shows very little backscatter below range 18. From range 18 up to range 50, there are two main belts of backscatter and the scatter of relatively larger power is around range 20 to 25 and range 40 to 41. At ranges above 65, there is a very small patch of scatter. The radar velocity/region plot in figure 7.12 shows that most of the scatter between ranges 18 and 35 is ground backscatter and the scatter between ranges 35 and 45 is ionospheric. The scatter at ranges above 65 is ionospheric because of its large phase velocity.

The ray tracing results for 09:00:05 UT in figure 7.10 suggest that the orthogonal condition for backscatter to occur is satisfied between ranges 18 and 40. However, there is no evidence for ground scatter at these ranges. The backscatter at ranges above 65 is ground backscatter.

(2) 10:00 UT -- The radar scan data at 09:59:09 UT in figure 7.11 shows very little backscatter below range 15. Above range 15, there are roughly three patches of backscatter. One is from range 15 to 39, one from range 39 to 47, and one from range 59 to 65. The radar velocity/region plot in figure 7.12 identifies that below range 20 the radar scatter is mostly ionospheric, and between ranges 20 and 46 the radar scatter is mostly ground backscatter. At further ranges, between ranges 59 to 65, the radar scatter is again ionospheric.

The ray tracing results at 10:00:05 UT in figure 7.10 suggest that the radar scatter below range 20 should be ionospheric, and the scatter between ranges 20 and 25 should be some mixture of ionospheric backscatter and ground backscatter. The radar scatter from range 30 to 39 or 40 could be the second hop E-region scatter. Between ranges 40 and 58, the scatter is ground backscatter and there is no evidence for ionospheric backscatter at these ranges. The scatter at further ranges, between ranges 59 and 74, is ionospheric F-region scatter from the second hop.

(3) 11:00 UT -- The radar scan plot at 10:59:14 UT in figure 7.12 shows that below range 15 the radar scatter is mostly ionospheric. The patch between ranges 15 and

45 is identified as mostly ground backscatter. Above range 46, the scatter is again ionospheric backscatter.

The ray results at 11:00:05 UT in figure 7.10 suggest that the radar scatter below range 22 is ionospheric. From range 37 to 59, the scatter is (the second hop) ionospheric E-region backscatter mixed with some ground backscatter. At further ranges, the scatter is (the second hop) ionospheric F-region backscatter mixed with some ground backscatter.

(4) 12:00 UT -- The radar velocity/region plot at 11:59:20 UT in figure 7.12 identifies the radar backscatter as largely ground backscatter.

The ray tracing results at 12:00:05 UT in figure 7.10 suggest that the radar scatter below range 20 should be ionospheric (F-region) backscatter. The scatter between range 29 to 32 is the second hop E-region backscatter. The scatter between ranges 35 and 51 is ground backscatter. Above range 52, the scatter is ionospheric scatter mixed with some ground backscatter.

(5) 13:00 UT -- There are roughly two big patches in radar scan data at 12:59:25 UT shown in figure 7.11. One is between ranges 19 and 44, and the other is above range 45. The radar velocity/region plot in figure 7.12 indicates that most of the scatter below range 45 is ground backscatter and the scatter above range 45 is ionospheric.

The ray tracing results at 13:00:05 UT in figure 7.10 suggest that the radar scatter below range 35 should be ionospheric backscatter and there is no evidence for ground backscatter at these ranges. The scatter between ranges 37 and 51 is ground backscatter and the scatter above range 54 could largely be the second hop F-region backscatter.

(6) 14:00 UT -- The radar velocity/region plot at 13:59:31 UT in figure 7.12 shows that below range 20 the scatter is mostly ionospheric. Between ranges 35 and 42 there is a belt of ionospheric backscatter. Above range 45, radar receives another patch of ionospheric backscatter.

The ray tracing results at 14:00:05 UT in figure 7.10 take all radar scatter below range 25 for ionospheric backscatter. Between ranges 26 and 39, no scatter is computed in the modelling. The radar scatter between ranges 39 and 53 should be ground backscatter and there is no evidence for ionospheric backscatter at these ranges. The radar scatter above range 55 should largely be the second hop F-region backscatter.

7.4.4 Discussion

The above comparison shows the agreement and disagreement between the beam-scan mode modelling and the Finland radar observations for the six selected UT times on 1 March 1995. In figure 7.12, the radar criteria identify most of the closest range radar scatter (e.g. below range 15) as ionospheric mixed with a little ground backscatter. The ray tracing results suggest that below range 20 the radar backscatter should be ionospheric and there is no evidence for ground backscatter at these ranges. The ray tracing results also suggest that most of the close range main red patches in figure 7.11 are ionospheric backscatter, whereas the radar criteria identify them as ground backscatter. For the far range radar scatters, the radar criteria are likely to identify them as ionospheric (see figure 7.12). The ray tracing results suggest that they are largely the second hop ionospheric scatter mixed with some ground backscatter, and sometimes they can be ground backscatter only. The middle range radar scatter is sometimes ground, sometimes ionospheric, and sometimes mixed backscatter.

It is noticed that some range gaps exist in the ray tracing results. This may be caused by the too big ray tracing angular step of one degree per ray in both elevation and azimuth, and may also be affected by the too strict orthogonal condition with the earth's magnetic field. Using smaller (ray tracing) angular step and less strict orthogonal criterion may help reduce the range gaps in the ray tracing results. It is also noticed that the radar frequency in real operation is not kept constant. The radar frequency varies with time and the variation could sometimes be as large as 0.1 MHz. This frequency variation may also affect the above comparison to some extent.

7.5 RADAR SUMMARY PLOT MODELLING

The summary plot modelling is, in fact, the same as the ray tracing modelling in the beam-scan mode, but only for the radar beam 5. This mode gives a 24 (UT) hour radar summary plot simulation and is good at illustrating how the radar scatter varies diurnally. The ionosphere may inevitably tilt a little during sunrise and sunset, and the assumption of a pure horizontally stratified ionosphere may not be good for those periods. In this summary plot modelling, both one-hop and two-hop ray propagation are investigated. Emphasis is given to the separation of radar ionospheric echoes from ground backscatter, and the possible effect of the second hop HF ray propagation.

7.5.1 Radar summary plot of beam 5

Figure 7.13 is the Finland radar summary plot for 1 March 1995. The top panel shows 24 hours backscatter data received by the radar beam 5 and colour-scaled in backscatter power. The middle panel is a velocity/region plot of the data and the bottom panel is colour-scaled in spectral width. The top panel of the summary plot shows that between 00:00 UT and 05:00 UT, except for very close ranges, very little backscatter is received. From 05:00 UT until 18:00 UT, there is considerable backscatter between ranges 15 and 60. It seems that the radar scatter from 05:00 UT to 18:00 UT could be separated into two main belts of backscatter. One is the belt of closer ranges and of relatively larger backscatter power (the main red belt), and the other is the belt at further ranges and of less backscatter power. After 18:00 UT, again, the radar scatter is mainly from very close ranges.

In the middle panel of figure 7.13, the radar criteria identify most of the radar scatter from very close ranges as ionospheric. Between 05:00 UT and 18:00 UT, the closer range backscatter patch of relatively larger backscatter power is identified as mostly ground scatter and the further range patch is partly ionospheric and partly ground backscatter.

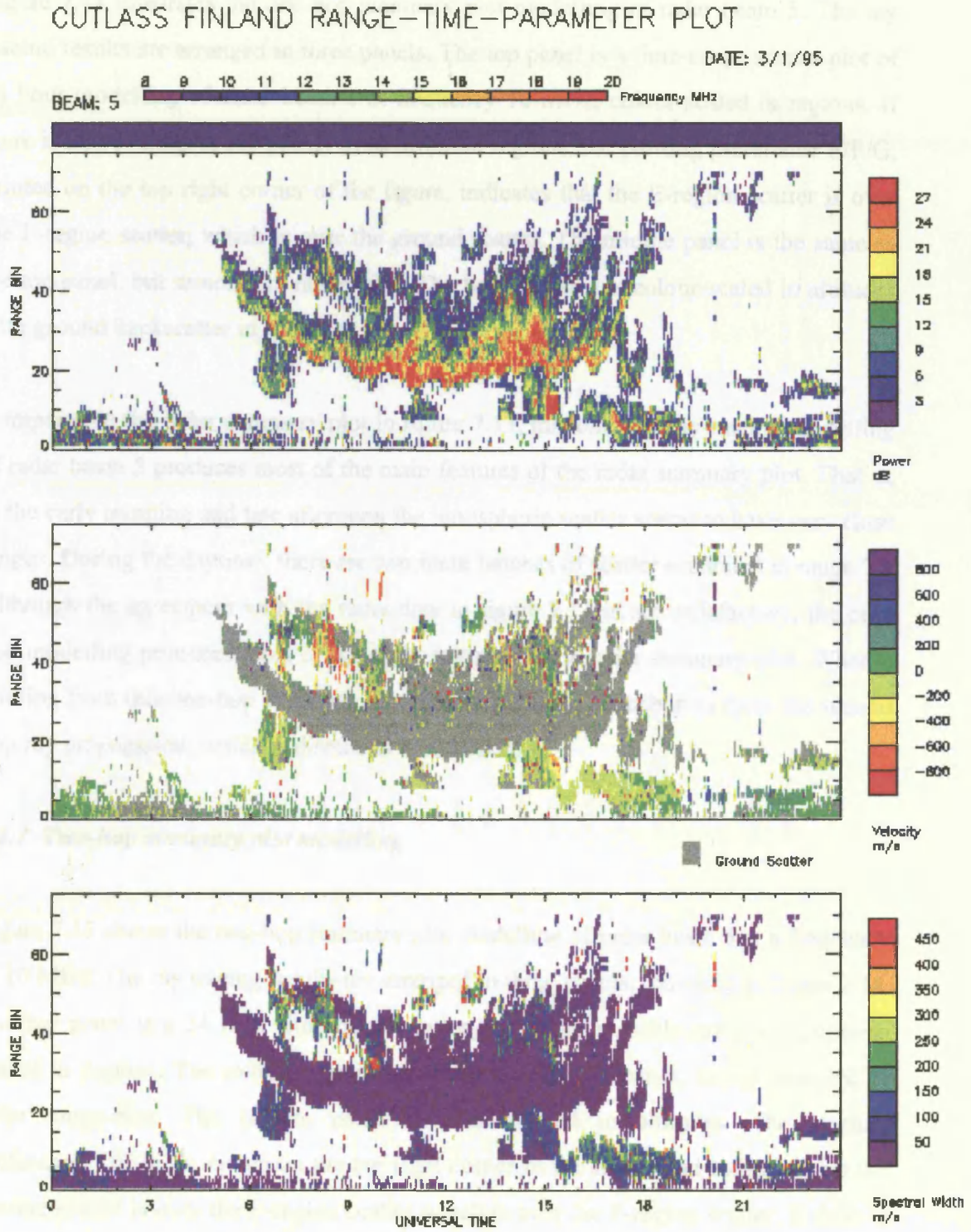

Figure 7.13 Finland radar summary plot for 1 March 1995

7.5.2 One-hop summary plot modelling

Figure 7.14 illustrates the one-hop summary plot modelling of radar beam 5. The ray tracing results are arranged in three panels. The top panel is a time-range scatter plot of 24 hour modelling of radar beam 5 at frequency 10 MHz, colour-scaled in regions. If there is any overlap of ray points from different regions, the plotting preference E/F/G, printed on the top right corner of the figure, indicates that the E-region scatter is over the F-region scatter, which is over the ground scatter. The middle panel is the same as the top panel, but sampled in range-bins. The bottom panel is colour-scaled in altitudes with ground backscatter in grey.

Compared to the radar summary plot in figure 7.13, this one-hop ray tracing modelling of radar beam 5 produces most of the main features of the radar summary plot. That is, in the early morning and late afternoon the ionospheric scatter seems to have very close ranges. During the daytime, there are two main patches of scatter separated at range 30. Although the agreement with the radar data in figure 7.13 is not satisfactory, the one-hop modelling produces most of the main features of the radar summary plot. What is missing from this one-hop summary plot modelling is the contribution from the second hop ray propagation, which is discussed in next section.

7.5.3 Two-hop summary plot modelling

Figure 7.15 shows the two-hop summary plot modelling of radar beam 5 at a frequency of 10 MHz. The ray tracing results are arranged in three panels, the same as figure 7.14. The top panel is a 24 hour time-range scatter plot of all possible ray points, colour-scaled in regions. The middle panel is the same as the top panel, except sampled in radar range-bins. The bottom panel is colour-scaled in altitudes. The plotting preference, G/E/F, is shown on the top right corner of the figure and indicates that the ground scatter is over the E-region scatter which is over the F-region scatter, if there is any possible overlap of scatters from different regions.

The two-hop ray tracing results in figure 7.15 demonstrate that before 06:00 UT the second hop scatter could be from as far as range 60, or even up to range 70. This far

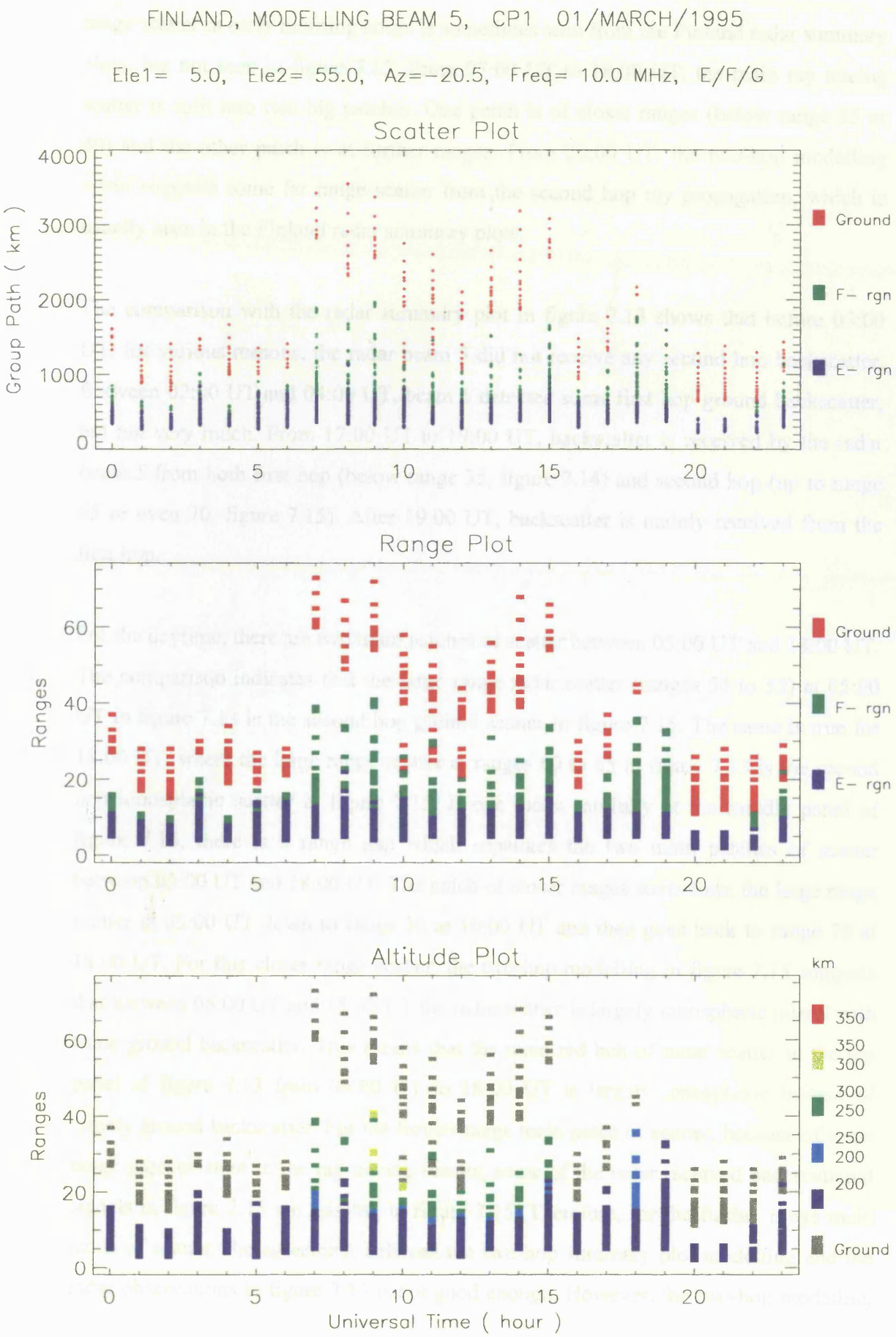

Figure 7.14 One-hop summary plot modelling of radar beam 5

range scatter in early morning hours is sometimes seen from the Finland radar summary plots, but not seen in figure 7.13. From 07:00 UT to 18:00 UT, the main ray tracing scatter is split into two big patches. One patch is of closer ranges (below range 35 or 40) and the other patch is at further ranges. From 20:00 UT, the two-hop modelling again suggests some far range scatter from the second hop ray propagation, which is usually seen in the Finland radar summary plots.

The comparison with the radar summary plot in figure 7.13 shows that before 05:00 UT, for various reasons, the radar beam 5 did not receive any second hop backscatter. Between 02:00 UT and 04:00 UT, beam 5 detected some first hop ground backscatter, but not very much. From 17:00 UT to 19:00 UT, backscatter is received by the radar beam 5 from both first hop (below range 35, figure 7.14) and second hop (up to range 65 or even 70, figure 7.15). After 19:00 UT, backscatter is mainly received from the first hop.

For the daytime, there are two main patches of scatter between 05:00 UT and 18:00 UT. The comparison indicates that the large range radar scatter (ranges 50 to 55) at 05:00 UT in figure 7.13 is the second hop ground scatter in figure 7.15. The same is true for 18:00 UT, where the large range scatter at ranges 60 to 65 in figure 7.13 is the second hop ionospheric scatter in figure 7.15. If one looks carefully at the middle panel of figure 7.15, there is a range gap which separates the two main patches of scatter between 05:00 UT and 18:00 UT. The patch of closer ranges starts from the large range scatter at 05:00 UT down to range 30 at 10:00 UT and then goes back to range 70 at 18:00 UT. For this closer range scatter, the two-hop modelling in figure 7.15 suggests that between 06:00 UT and 18:00 UT the radar scatter is largely ionospheric mixed with some ground backscatter. This means that the main red belt of radar scatter in the top panel of figure 7.13 from 06:00 UT to 18:00 UT is largely ionospheric instead of largely ground backscatter. For the further range main patch of scatter, because of some range gaps existent in the ray tracing results, some of the radar received backscattered signals in figure 7.13 are missing in figure 7.15. Therefore, for the further range main patch of scatter, the agreement between the two-hop summary plot modelling and the radar observations in figure 7.13 is not good enough. However, the two-hop modelling

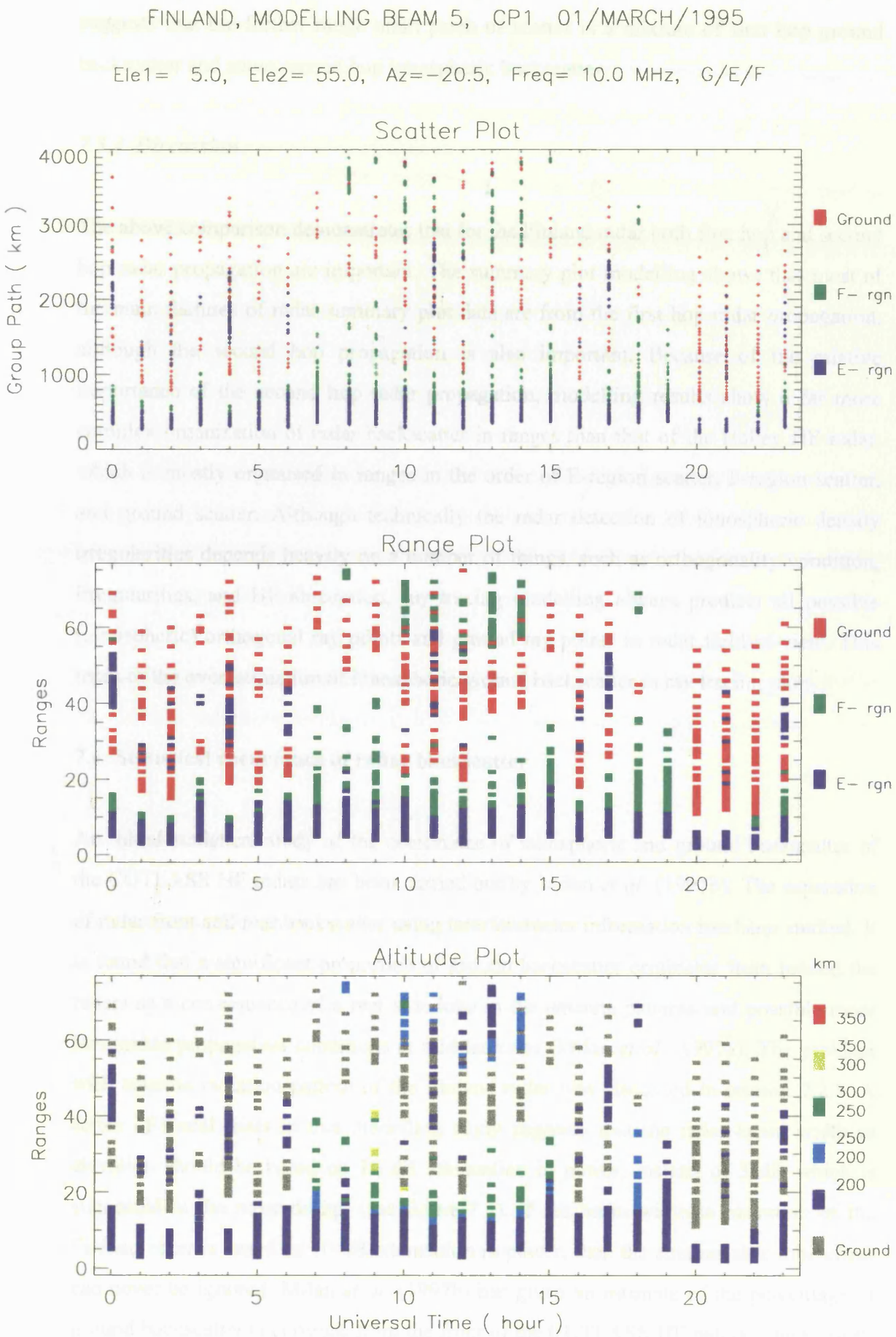

Figure 7.15 Two-hop summary plot modelling of radar beam 5

suggests that the further range main patch of scatter is a mixture of first hop ground backscatter and some second hop ionospheric backscatter.

7.5.4 Discussion

The above comparison demonstrates that for the Finland radar both first hop and second hop radar propagation are important. The summary plot modelling shows that most of the main features of radar summary plot data are from the first hop radar propagation, although the second hop propagation is also important. Because of the relative importance of the second hop radar propagation, modelling results show a far more complex organisation of radar backscatter in ranges than that of the Halley HF radar, which is mostly organised in ranges in the order of E-region scatter, F-region scatter, and ground scatter. Although technically the radar detection of ionospheric density irregularities depends heavily on a number of things, such as orthogonality condition, irregularities, and HF absorption, ray tracing modelling always predicts all possible (ionospheric) orthogonal ray points and ground ray points in radar field-of-view. This leads to the overestimation of ionospheric/ground backscatter in ray tracing plots.

7.6 Statistical occurrence of radar backscatter

An initial statistical study of the occurrence of ionospheric and ground backscatter of the CUTLASS HF radars has been carried out by Milan *et al.* (1997b). The separation of radar front and rear backscatter using interferometer information has been studied. It is found that a significant proportion of ground backscatter originates from behind the radars as a consequence of a rear side-lobe in the antenna patterns and possible more favourable propagation conditions at mid-latitudes (Milan *et al.*, 1997a). The problem with antenna radiation pattern of the Finland radar was discussed in section 7.2.1. A series of initial trials in this modelling study suggests that the radar beam width in elevation should be based on 10 dB attenuation in power, instead of 3 dB which is suggested in the radar design (see figure 7.2). If the beam width in elevation of the Finland radar is based on 10 dB attenuation in power, then the antenna side-lobe effect can never be ignored. Milan *et al.* (1997b) has given an estimate of the percentage of ground backscatter occurrence from the front of the CUTLASS HF radars. Their results

are reproduced here in Figure 7.16, which shows that significant (more than 50%) ground backscatter may come from behind the CUTLASS radars during winter and early spring. This may be part of the reason why the range gaps in the ray tracing results are not seen in radar observations.

The statistical study (Milan *et al.*, 1997b) suggests that the diurnal variation of the occurrence of far range ionospheric backscatter of the Finland radar has two maxima, one pre-noon and one post-noon. The variation of the UT times of the two maxima with months is shown in figure 7.17, in general being most separated near the equinoxes and approaching local noon towards winter solstice, until they merge to form a single peak in December 1995 and January 1996. Since data for March 1995 is not included in figure 7.17, we use the data for March 1996 instead. The figure shows that the two maxima of the occurrence of far range ionospheric scatter for March 1996 are at 6.30 UT and 15.30 UT. The ranges for the two maxima in March 1995 shown in their figure 7a are roughly from 40 to 46 (Milan *et al.*, 1997b). This is predicted by the two-hop summary plot modelling in figure 7.15, with both the pre-noon and post-noon far range scatter being from the second hop E-region at 06:00 UT and 17:00 UT, respectively. The second hop E-region scatter at 04:00 UT is not observed by the radar (see figure 7.15).

7.7 SUMMARY

To summarise, this chapter discusses the beam-scan mode and summary plot modelling of the CUTLASS HF radar in Finland. Comparison to the radar observations for 1 March 1995 is made. Emphasis is given to the separation of radar ionospheric echoes from ground backscatter and the possible effect of the second hop HF ray propagation.

For the beam-scan mode, the comparison to the radar scan data for 1 March 1995 shows that in general the agreement is good in ranges, but not in regions. It appears that the radar criteria tend to interpret close range scatter for ground scatter, whereas ray tracing results often strongly suggest that the close range scatter, between ranges 15 and 25, should mostly be ionospheric backscatter.

For the summary plot modelling, the comparison shows that the one-hop modelling produces most of the main features of the radar summary plot data for 1 March 1995, and that the two-hop modelling adds in the contributions from the second hop HF ray propagation. The two-hop modelling makes a better comparison to the radar summary plot data. That means for the Finland radar the second hop propagation is important. The comparison also suggests that the radar criteria are likely to identify those close range ionospheric scatter as ground backscatter. Besides, the two-hop summary plot modelling predicts the far range ionospheric scatter at the UT times of the two maxima of the occurrence of the radar ionospheric scatter in figure 7.17.

It is noticed that, compared to radar observations, some range gaps exist in ray tracing results. These range gaps may be caused by the too big ray tracing angular step of every one degree per ray in both elevation and azimuth. It could also be caused by the too strict orthogonal condition with the earth's magnetic field. It may help to reduce the range gaps in ray tracing results by using a smaller (ray tracing) angular step in both elevation and azimuth, and by using a less strict criterion of orthogonality. The rear side-lobe effect of the radar antenna may be part of the reason why the range gaps in ray tracing results are not usually seen in the radar data.

CHAPTER 8

CONCLUSIONS AND FUTURE WORK

8.1 INTRODUCTION

In both equatorial and high-latitude regions, pronounced radar backscatter is frequently received from small-scale plasma density irregularities of the ionosphere. This fact implies the possibility of investigating the ionospheric small-scale dynamics using ground-based radar systems. This research has involved ray tracing modelling of HF coherent detection of irregularities in the high-latitude ionosphere. All discussions are based on two HF radar systems, the Halley HF radar in Antarctica and the CUTLASS HF radar in Finland. A brief summary is now presented of the main background theory and the modelling techniques used in the research. The most important modelling results and the conclusions are highlighted.

8.2 IRREGULARITIES AND COHERENT BACKSCATTER

The clear-air radar scatter from the ionospheric region is caused by small fluctuations of radio refractive index, which are in turn produced by the fluctuations of electron density in the region. The fluctuations of electron density in the ionospheric E- and F- regions can be produced and sustained by various plasma instability processes (Farley, 1963; Buneman, 1963; Dungey, 1956). Because of the existence of the earth's magnetic fields, the ionospheric plasma is no longer isotropic electrically. Small-scale irregularities tend to be elongated along the earth's magnetic field lines.

Historically, most early radar studies of F-region irregularities have been confined to low and mid-latitudes where VHF and UHF radars can achieve the requisite orthogonality condition with the earth's magnetic field (Woodman *et al.,* 1976; Tsunoda *et al.*, 1979). At high-latitudes, the magnetic field lines are very close to vertical. This makes VHF and UHF radars very difficult to reach the orthogonality condition in the F-region. Taking advantage of the ionospheric refraction at lower frequencies, HF radars can achieve the orthogonality condition in both the E- and F-regions, and thus have been used to investigate small-scale irregularities in the high-latitude ionosphere (Greenwald *et al.*, 1995).

8.3 GROUND SCATTER AND RADAR CRITERIA

The radar observations also consist direct backscatter from the ground. An uncertainty arises due to the difficulty in separating true ground backscatter from ionospheric scatter which fulfils the radar criteria based on the measured Doppler velocity and spectral width. The radar ground backscatter is defined as scatter whose Doppler velocity and spectral width are both less than 50 m/s.

8.4 THE JONES3D PROGRAMME

The Jones3D programme (Jones and Stephenson, 1975) is one of the most widely used ray tracing computer programmes for radio waves in the ionosphere (Villain, *et al.*, 1984; Villain, *et al.*, 1985; Samson, *et al.*, 1990; Anderson, *et al.*, 1996). In this research, the programme has been modified to simulate HF radar detection of field-aligned small-scale irregularities in the high-latitude ionosphere. Although ray tracing can not produce dynamic parameters such as Doppler velocity and spectral width, which are used by radar to separate ionospheric echoes from ground backscatter, the modified version of Jones3D has the ability to distinguish between those ray points for which the orthogonal condition is satisfied and those ray points for which the ground is reached.

The main modifications made to the programme are summarised below.

(i) implementing a Gaussian extrapolation scheme in TABLEX to obtain a reasonable bottom-side profile of electron density

(ii) implementing the mechanism of computing orthogonal ray points and ground ray points

(iii) enabling to trace the rays up to any altitude above the F2 peak

(iv) setting a lower and upper height limit for the computation of orthogonal ray points

8.5 MODELLING SPECIFICATIONS

The specifications of the Jones3D programme used in the research are summarised below. Discussions of the specifications can be found in chapter 5.

(1) Only O-mode rays are traced.

(2) The earth-centred dipole model is used for the earth's magnetic fields.

(3) Numerical profiles of electron density (TABLEX) are used for the model inputs of realistic ionospheric conditions.

(4) No ionospheric perturbations and no tilts are considered.

(5) A combination of two exponentials is used for the profile of electron collision frequency.

(6) Radio refractive index is computed using the Appleton-Hartree formula with the magnetic field and electron-neutral collisions.

(7) The ray orthogonal condition: when the angle of ray wave vector **k** to the local geomagnetic field **B** is within one degree of perpendicularity, i.e. within 89 to 91 degrees, orthogonality is assumed.

(8) For both physics and computational purposes, orthogonalities with the earth's magnetic field lines are only computed and plotted between the user specified lower and upper height limits (see chapter 4). In this research, the lower and upper height limits are set to 90 and 500 km altitude, respectively.

8.6 MODEL INPUTS OF REALISTIC IONOSPHERIC CONDITIONS

For the Halley HF radar in Antarctica, the model inputs of realistic ionospheric conditions are computed directly by POLAN (Titheridge, 1985) from Halley AIS

dynasonde data. EISCAT CP1 data measured at Tromso are used for the modelling study of the CUTLASS HF radar in Finland.

8.7 DIFFERENT MODES OF HF RADAR MODELLING

In this modelling study, two different modes of ray tracing have been performed, the B-mode and beam-scan mode. In the B-mode, all 16 radar beams are simulated into one big rectangular beam, whose overall radiation pattern is assumed to be flat. In the beam-scan mode, the radar 16 beams are traced individually one by one from beam 0 to beam 15 through the same ionosphere. The sampling of each of the 16 beams is exactly the same as in the radar operation, starting from the first range gate by range resolution. In each range-cell, if one or more E-region orthogonal, F-region orthogonal or ground ray points are sampled, then the radar is assumed to have received E-region, F-region or ground backscatter from the range-cell.

The advantage of the B-mode modelling lies in its statistical meaning of the computation of orthogonal ray points and ground ray points. In fact, the more orthogonal ray points (or ground ray points) that are computed in a range-cell, the better the chance for the radar to receive ionospheric (or ground) backscatter from the range-cell. It is this statistical meaning of the computation of orthogonal ray points and ground ray points which makes sense to the B-mode modelling. On the other hand, the beam-scan mode provides a natural way of simulating the radar beam-scan mode operation. It is easy to compare the beam-scan mode results with radar scan data.

8.8 HF RADAR MODELLING -- CASE STUDY ONE

In the case study for the Halley HF radar in Antarctica, both the B-mode and beam-scan mode modelling have been performed. Comparisons with the radar observations are made. Compared with one radar scan data, the agreement between the B-mode results and radar observations is good in ranges, but not good in regions (figure 6.3). This is because two different methods are used to separate radar ionospheric echoes from ground scatter. The radar uses radar criteria based on the measured Doppler velocity and spectral width, whereas ray tracing modelling uses the heights of orthogonal and

ground ray points. The range-bin statistical analysis in figures 6.4 and 6.5 shows that (for one hour radar data) the B-mode modelling simulates the radar observations very well in terms of the count rate of radar scatter as a function of range, and demonstrates that the B-mode is good at investigating the probability of receiving radar backscatter from a given range (or range-bin). The comparisons indicate that the radar criteria based on the measured Doppler velocity and spectral width are not sufficient, and that the measured range (group path) parameter can play an important part in identifying radar ionospheric scatter from ground scatter.

The beam-scan mode modelling and its range-bin statistical analysis in figures 6.8 and 6.9 have confirmed the importance of the measured range parameter in separating radar ionospheric scatter from ground scatter. In comparison with radar scan data, the beam-scan mode results indicate that the radar criteria tend to interpret close range (below range 20) ionospheric scatter of relatively larger backscatter power for ground scatter.

Both the B-mode and beam-scan mode results indicate that for the Halley HF radar the main propagation mode is one-hop propagation mode, and the radar scatter is mostly organised in ranges in the order of E-region scatter, F-region scatter, and ground scatter (bottom panels of figures 6.4 and 6.5).

8.9 HF RADAR MODELLING -- CASE STUDY TWO

In the case study for the CUTLASS HF radar in Finland, in addition to the beam-scan mode modelling, the summary plot modelling of radar beam 5 has also been performed. Comparisons with the radar observations are made. Compared to radar observations, both the beam-scan mode and summary plot modelling suggest that for the CUTLASS HF radar in Finland both first hop and second hop radar propagation are important.

The comparison between the beam-scan mode results in figure 7.10 and the radar scan data in figure 7.12 indicates that the radar criteria tend to identify close range (below range 20 for the two middle panels at 11:00:05 UT, 12:00:05 UT, and below range 30 for the bottom left panel at 13:00:05 UT of figure 7.10) F-region scatter as ground

scatter. For E-region scatter (at 11:00:05 UT and 14:00:05 UT of figure 7.10), the radar criteria are mostly correct.

The summary plot modelling of radar beam 5 demonstrates that the one-hop modelling in figure 7.14 produces most of the main features of the radar summary plot data in figure 7.13. The two-hop results in figure 7.15 add in the contributions from the second hop ray propagation and make a better comparison. Besides, the two-hop modelling produces the far range ionospheric scatter at the UT times of the two maxima of radar backscatter occurrence found in a statistical study of the Finland radar data (Milan *et al.*, 1997b).

8.10 SUMMARY

The modelling case study for the Halley HF radar in Antarctica shows that the radar main propagation mode is one-hop propagation. Ray tracing results in both the B-mode and beam-scan mode indicate that the radar criteria based on the measured Doppler velocity and spectral width are not sufficient. The measured range (group path) parameter is important and should be used in separating radar ionospheric echoes from ground backscatter. Modelling results indicate that (for the Halley HF radar in Antarctica) radar scatter is mostly organised in ranges in the order of E-region scatter, F-region scatter, and ground scatter (bottom panels of figures 6.4 and 6.5).

The modelling case study for the CUTLASS HF radar in Finland indicates that for the Finland radar both first hop and second hop radar propagation are important. The beam-scan mode modelling shows that the radar criteria are good for E-region scatter, but tend to identify close range F-region scatter as ground scatter. The summary plot modelling shows that most of the main features of radar summary plot data are from the first hop radar propagation, although the second hop propagation is also important. Because of the relative importance of the second hop radar propagation, modelling results show a far more complex organisation of radar scatter in ranges than that of the Halley HF radar.

In this research, it has been found that ray tracing is very useful in determining the radar beam-width in elevation. For the Halley HF radar, the radar beam-width in elevation is found to be from 15° to 56°, not from 20° to 56°. This has been confirmed (Mike Pinnock, private communication 1994). For the CUTLASS HF radar in Finland, ray tracing results suggest that the radar beam-width should be based on 10 dB attenuation in power, rather than 3 dB. When the radar beam-width is based on 10 dB attenuation, the rear side-lobe effect of the radar antenna will not be negligible (figure 7.2). This has also been confirmed (Milan *et al.*, 1997a).

8.11 SUGGESTIONS FOR FUTURE WORK

Suggestions for future work are listed below.

(1) Use the range (group path) information obtained from the range-bin statistical analysis (chapter 6) and the other three measured parameters (backscatter power, Doppler velocity, and spectral width) to further investigate the radar criteria.

(2) Use the CUTLASS radars interferometer data and the B-mode ray tracing modelling to investigate the rear side-lobe effect on both first hop and second hop radar propagations.

References

[1] Aarons, J. (1973): 'A descriptive model of F-layer high-latitude irregularities as shown by scintillation observations', J. Geophys. Res., 78, p. 7441

[2] Anderson, D. N., Decker, D. T., and Valladares, C. E. (1996): 'Global Theoretical Ionospheric Model (GTIM)', in 'Solar Terrestrial Energy Program, Handbook of Ionospheric Models', Ed. R. W. Schunk

[3] Axford, W. I. and Hines, C. O. (1961): 'A unifying theory of high-latitude geophysical phenomena and geomagnetic storms', Can. J. Phys., 39, p. 1433

[4] Baker, K. B., Greenwald, R. A., Villain, J. P. and Wing, S. (1987): 'Spectral characteristics of high frequency (HF) backscatter from high-latitude ionospheric irregularities: preliminary analysis of statistical properties', Interim report RADC-TR-87-284, Rome air Development Center, Griffiss AFB, NY, USA

[5] Baker, K. B, Greenwald, R. A., Ruohoniemi, J. M., Dudeney, J. R., Pinnock, M., Mattin, N. and Leonard, J. M. (1989a): 'PACE Polar Anglo-American Conjugate Experiment', EOS, 70, p. 785

[6] Baker, K. B. and Wing, S. (1989b): 'A new magnetic coordinate system for conjugate studies at high latitudes', J. Geophys. Res., 94, p. 9139

[7] Berkner, L. V. and Wells, H. W. (1934): 'F- region ionospheric investigations at low latitude', Terr. Magn. Atmos. Elec., 39, p. 215

[8] Berkner, L. V. and Wells, H. W. (1937): 'Abnormal ionization of the E- region of the ionosphere', Terr. Magn. Atmos. Elec., 42, p. 73

[9] Booker, H. G. (1949): 'Application of the magneto-ionic theory to radio waves incident obliquely upon a horizontally-stratified ionosphere', J. Geophys. Res., 54, p. 243

[10] Booker, H. G. (1956): 'Turbulence in the ionosphere with applications to meteor trails, radio-star scintillation, auroral radar echoes and other phenomena', J. Geophys. Res., 61, p. 673

[11] Breit, G. and Tuve, M. A. (1926): 'A test of the existence of the conducting layer', Phys. Rev., 28, p. 554

[12] Bristow, W. A. and Greenwald, R. A. (1995): 'Estimating gravity wave parameters from oblique high-frequency backscatter: Modeling and analysis', J. Geophys. Res., 100, p. 3639

[13] Budden, K. G. (1985): 'The propagation of radio waves'. Cambridge University Press, Cambridge

[14] Buneman, O. (1963): 'Excitation of field aligned sound waves by electron streams', Phys. Rev. Lett., 10, p. 285

[15] Cerisier, J. C., Berthelier, J. J., and Beghin, C. (1985): 'Unstable density gradients in the high-latitude ionosphere', Radio Sci., 20, p. 755

[16] Chapman, S. (1953): 'Geometry of radio reflection from aurora', J. Atmos. Terr. Phys., 3, p. 1

[17] Collins, C. and Forsyth, P. A. (1959): 'A bistatic radio investigation of auroral ionization', JATP, 13, p. 315

[18] Croft, T. A. (1972): 'Sky-wave backscatter: A means for observing our environment at great distances', Rev. Geophys. Space Phys., 10, p. 73

[19] Davies, K. (1990): 'Ionospheric Radio', IEE Electromagnetic Waves Series 31, Peter Peregrinus Ltd.

[20] Dudeney, J. R. and Piggott, W. R. (1978): 'Antarctic ionospheric research' in Lanzerroti, L. J. and Park, C. G. (ed.): 'Upper Atmosphere Research in Antarctica', Antarctic Research Series, vol. 29, p. 200

[21] Dungey, J. W. (1956): 'Convective defusion in the equatorial F-region', J. Atmos. Terr. Phys., 9, p. 304

[22] Dungey, J. W. (1961): 'Interplanetary magnetic field and the auroral zones', Phys. Rev. Lett., 6, p. 47

[23] Farley, D. T. (1963): 'A plasma instability resulting in field-aligned irregularities in the ionosphere', J. Geophys. Res., 68, p. 6083

[24] Farley, D. T. (1985): 'Theory of equatorial electrojet plasma waves : new developments and current status', J. Atmos. Terr. Phys., 47, p. 729

[25] Fejer, B. G. and Kelley, M. C. (1980): 'Ionospheric irregularities', Rev. Geophys., 18, p. 401

[26] Fejer, J. A. (1979): 'Ionospheric instabilities and fine structure', J. Atmos. Terr. Phys., 41, p. 895

[27] Fukao, S. (1989): 'International School on Atmospheric Radar', Handbook for MAP 30, Middle Atmosphere Program

[28] Glassmeier, K.-H. (1987): 'Ground-based observations of field-aligned currents in the auroral zone: Methods and results', Annales Geophysicae, 5A, (3), p. 115

[29] Glassmeier, K.-H., Honisch, M. and Untiedt, J. (1989): 'Ground-Based and Satellite Observations of Traveling Magnetospheric Convection Twin Vortices', J. Geophys. Res., vol. 94, A3, p. 2520

[30] Greenwald, R. A., Ecklund, W. L., and Balsley, B. B. (1975): 'Radar Observations of Auroral Electrojet Currents', J. Geophys. Res., 80, p. 3635

[31] Greenwald, R. A., Weiss, W., Nielsen, E., Thomson, N. R. (1978): 'STARE: A new radar auroral backscatter experiment in northern Scandinavia', Radio Sci., 13, p. 1021

[32] Greenwald, R. A., Baker, K. B., Hutchins, R. A. and Hanuise, C. (1985): 'An HF phased-array radar for studying small-scale structures in the high-latitude ionosphere', Radio Sci., 20, p. 63

[33] Greenwald, R. A., Baker, K. B., Dudeney, J. R., Pinnock, M., Jones, T. B., Thomas, E. C., Villain, J.-P., Cerisier, J.-C., Senior, C., Hanuise, C., Hunsucker, R. D., Sofko, G., Koehler, J., Nielsen, E., Pellinen, R., Walker, A. D. M., Sato, N. and Yamagishi, H. (1995): 'DARN/SUPERDARN, A Global View of the Dynamics of High-Latitude Convection', Space Sci. Reviews, 71, p. 761

[34] Grubb, R. N. (1979): 'The NOAA SEL HF radar system (Ionospheric Sounder)', NOAA Tech. Memo. ERL SEL-55

[35] Haldoupis, C. (1989): 'A review on radio studies of auroral E-region ionospheric irregularities', Annales Geophysicae, 7, p. 239

[36] Haldoupis, C., Schlegel, K., and Nielsen, E. (1993): 'Some observations of radio auroral backscatter at 140 MHz during E-region electron gas heating', Annales Geophys., 11, p. 283

[37] Harang, L. and Stoffregen, W. (1938); 'Scattered reflections of radio waves from a height of more than 100 km', Nature (Lond), 142, p. 832

[38] Harang, L. and Stoffregen, W. (1961): 'Investigation of auroral echoes', Planet. Space Sci., 5, p. 33

[39] Hargreaves, J. K. (1992): 'The solar-terrestrial environment', Cambridge Atmospheric and Space Science Series 5, Cambridge University Press

[40] Haselgrove, J. (1955): 'Ray theory and a new method for ray tracing', Physics of the ionosphere, Phys. Soc., London, p. 355

[41] Hoh, F. C. (1963): 'Instability of Penning-type discharge', Phys. Fluids, 6, p. 1184

[42] Hunsucker, R. D. (1991): 'Radio Techniques for Probing the Terrestrial Ionosphere', Springer-Verlag

[43] Jones, R. M. (1968): 'A three-dimensional ray-tracing computer program', Digest of ESSA Tech. Rep. ITSA No. 17. Radio Sci., 3, p. 93

[44] Jones, R. M. and Stephenson, J. J. (1975): 'A versatile three-dimensional ray tracing computer program for radio waves in the ionosphere', OT Report 75-76. US Govt. Printing Office, Washington DC 20402

[45] Jones, R. M., Georges, T. M., and Riley, J. P. (1986): 'Measured ionospheric distortion of HF ground-backscatter spectra', IEEE Trans., AP-34, p. 563

[46] Kamide, Y. and Baumjohann, W. (1993): 'Magnetosphere - Ionosphere coupling', Springer-Verlag

[47] Kelley, M. C. and Heelis, R. A. (1989): 'The Earth's Ionosphere - Plasma Physics and Electrodynamics', International Geophysics Series, vol. 43, Academic Press, Inc.

[48] Kelso, J. M. (1964): 'Radio ray propagation in the ionosphere', McGraw-Hill Co., Inc., New York

[49] Leadabrand, R. L., Larson, A. G., and Hodges, J. C. (1967): 'Preliminary results on the wavelength dependence and aspect sensitivity of radar auroral echoes between 50 and 3000 MHz', J. Geophys. Res., 72, p. 3877

[50] Leonard, J. M. (1991): 'the phenology of Antarctic F- region irregularities', MPhil Dissertation, British Antarctic Survey and the University of Leicester

[51] Maliphant, R. G. (1968): 'HF ground backscatter analysis with the aid of computer ray tracing', in Thrane, E. (Ed.): 'Scatter propagation of radio waves'. AGARD Conf. Proc., No. 37, Advisory Group for Aerospace Research and Development, North Atlantic Treaty Organisation, p. 7-1

[52] McDiarmid, D. R. (1972): 'On the aspect sensitivity of radio aurora', Can. J. Phys., 50, p. 2557

[53] McDiarmid, D. R., Watermann, J., and McNamara, A. G. (1990): 'Can ionospheric refraction and oblique reflection explain the Canadian 48 MHz IGY radio aurora observations?', J. Geophys. Res., 95, p. 17261

[54] McNamara, A. G., McDiarmid, D. R., Sofko, G. J., Kochler, J. A., Forsyth, P. A. and Moorcroft, D. M. (1983): 'BARS - a dual bistatic auroral radar system for the study of electric field in the Canadian sector of the auroral zone', Adv. Space Res., 2, p. 145

[55] Milan, S. E., Jones, T. B., Robinson, T. R., Thomas, E. C. and Yeoman, T. K. (1997a): 'Interferometric evidence for the observation of ground backscatter originating behind the CUTLASS coherent HF radars', Annales Geophysicae', 15, p. 29

[56] Milan, S. E., Yeoman, T. K., Lester, M., Thomas, E. C., and Jones, T. B. (1997b): 'Initial backscatter occurrence statistics from the CUTLASS HF radars', Annales Geophysicae, 15, p. 703

[57] Moorcroft, D. R. (1985): 'An examination of radio-auroral aspect sensitivity', Can. J. Phys., 63, p. 1005

[58] Moorcroft, D. R. (1989): 'Refraction and reflection by tilted layers: An explanation for VHF auroral backscatter at large aspect angles', Geophys. Res. Lett., 16, p. 235

[59] Nielsen, E., Guettler, W., Thomas, E. C., Stewart, C. P., Jones, T. B. and Hedberg, A. (1983): 'SABRE: A new radar auroral backscatter experiment', Nature, 304, p. 712

[60] Nielsen, E. and Schlegel, K. (1985): 'Coherent radar Doppler measurements and their relationship to the ionospheric electron drift velocity', J. Geophys. Res., 90, p. 3498

[61] Nygren, T. (1996): 'Introduction to incoherent scatter measurements', Inverse Publications

[62] Piggott, W. R. and Rawer, K. (1972): 'U.R.S.I. handbook of ionogram interpretation and reduction', Rep. UAG-23, World Data Center A for Solar Terrestrial Physics, Boulder, Colo., USA

[63] Piggott, W. R. (1975): 'High latitude supplement to the U.R.S.I. handbook of ionogram interpretation and reduction', Report UAG-50, World Data Center-A for Solar Terrestrial Physics, Boulder CO, USA

[64] Pinnock, M., Conder, J. and Heron, S. (1994): 'SuperDarn antenna array, radiation pattern measurements', SuperDarn workshop, Orleans, p. 45

[65] Ratcliffe, J. A. (1970): 'Sun, Earth and Radio -- An introduction to the ionosphere and magnetosphere', World University Library.

[66] Rishbeth, H. and Garriott, O. (1969): 'Introduction to Ionospheric Physics', International Geophysics Series, vol. 14, Academic Press

[67] Rishbeth, H. (1988): 'Basic physics of the ionosphere: a tutorial review', Journal of the Institution of Electronic and Radio Engineers, vol. 58, no. 6, pp. s207-s223.

[68] Robin, G. de Q., Evans, S. and Bailey, J. T. (1969): 'Interpretation of radio echo sounding in polar ice sheets', Philosophical Transactions of the Royal Society, 265, p. 437

[69] Robinson, T. R. (1986): 'Towards a self-consistent non linear theory of radar auroral backscatter', J. Atmos. Terr. Phys., 48, p. 417

[70] Robinson, T. R. (1994): 'The role of natural E- region plasma turbulence in the enhanced absorption of HF radio waves in the auroral ionosphere: Implications for RF heating of the auroral electrojet', Annales Geophys., 12, p. 316

[71] Rogister, A. and D'Angelo, N. (1970): 'Type II irregularities in the equatorial electrojet', J. Geophys. Res., 75, p. 3879

[72] Ruohoniemi, J. M., Greenwald, A., Baker, K. D., Villain, J. P., and McCready, M. A. (1987): 'Drift motions of small scale irregularities in the high-latitude F-region: An experimental comparison with plasma drift motions', J. Geophys. Res., 92, p. 4553

[73] Samson, J. C, Greenwald, R. A., Ruohoniemi, J. M., Frey, A. and Baker, K. B. (1990): 'Goose Bay radar observations of earth-reflected atmospheric gravity waves in the high-latitude ionosphere', J. Geophys. Res., 95(A6), p. 7693

[74] Simon, A. (1963): 'Instability of a partially ionized plasma in crossed electric and magnetic fields', Phys. Fluids, 6, p. 382

[75] St-Maurice, J.-P. (1987): 'A unified theory of anomalous resistivity and Joule heating effects in the presence of ionospheric E-region irregularities', J. Geophys. Res., 92, p. 4533

[76] Titheridge, J. E. (1967): 'The overlapping-polynomial analysis of ionograms', Radio Science, 2, p. 1169

[77] Titheridge, J. E. (1985): 'Ionogram analysis with the generalised program POLAN', Report UAG-93, World Data Center-A, Boulder CO, USA

[78] Tsunoda, R. T., Barons, M. J., Owen, J., and Towle, D. M. (1979): 'Altair: an incoherent scatter radar for equatorial spread-F studies', Radio Science, 14, p. 1111

[79] Uspensky, M. V., Williams, P. J. S., Romanov, V. I., Pivovarov, V. G., Sofko, G. J., and Koehler, J. A. (1994): 'Auroral radar backscatter at off-perpendicular aspect angles due to enhanced ionospheric refraction', J. Geophys. Res., 99, p. 17503

[80] Villain, J. P., Greenwald, R. A. and Vickrey, J. F. (1984): 'HF ray tracing at high-latitudes using measured meridional electron density distributions', Radio Sci., 19, p. 359

[81] Villain, J. P., Caudal, G. and Hanuis, C. (1985): 'A SAFARI-EISCAT comparison between the velocity of F region small-scale irregularities and the ion drift', J. Geophys. Res., vol. 90, A9, p. 8433

[82] Villard, O. G. (1976): 'The ionospheric sounders and its place in the history of radio science', Radio Science, 11, p. 847

[83] Walker, A. D. M., Greenwald, R. A., and Baker, K. B. (1986): 'HF radar observations of pulsations near the magnetospheric cusp', J. Geophys. Res., 91, p. 8919

[84] West, J. C. and Dermarest, K. P. (1987): 'The radiation characteristics of an arbitrary antenna positioned on a polar ice sheet', Geophysics, 52, p. 1689

[85] Woodman, R. F., and LaHoz, C. (1976): 'Radar observations of F-region equatorial irregularities', J. Geophys. Res., 81, p. 5447

[86] Wright, J. W. and Pitteway, M. L. V. (1982): 'Data processing for the dynasonde', J. Geophys. Res., 87, p. 1589